University of Bremen

Alfred Wegener Institute - Helmholtz Centre for Polar and Marine Research

DOCTORAL THESIS

# Paleoclimate Data Assimilation with CLIMBER-X in Transient Simulation of the Last Deglaciation

*Author:*
Ahmadreza Masoum

*Supervisor and First Reviewer:*
Prof. Dr. Gerrit Lohmann

*Second Reviewer:*
Prof. Dr. Mihalis Vrekoussis

A thesis submitted in fulfillment of the requirements
for the degree of doctor rerum naturalium (Dr. rer. nat.)

in Physics/Electrical Engineering
Faculty 1

24 September 2024

# Abstract

Paleoclimate studies provide crucial insights into the Earth's climate system drivers and behavior, helping distinguish between natural climate patterns and human-induced changes and providing a context for current climate trends. The last deglaciation marked a period of Earth's history characterized by the retreat of massive ice sheets covering large parts of the planet. During this phase, a drastic transition occurred from the cold Last Glacial Maximum to the warmer and more stable climate of the Holocene. Besides proxy-based reconstructions and climate model simulations, data assimilation (DA) has emerged as a promising reconstruction technique of past climates. DA combines the data and the underlying dynamical principles governing the climate system to provide a state estimate of the system, which is better than that which could be obtained using just the data or the model alone.

As the first step of this dissertation, major uncertainties and forcing factors are evaluated for the last deglaciation using an efficient climate model. Two sets of transient simulations are based on the novel ice-sheet reconstruction PaleoMist and the established GLAC1D. The simulations reveal that the proximity of the Atlantic meridional overturning circulation (AMOC) to a bifurcation point, where it can switch between on- and off-modes, is primarily determined by the interplay of greenhouse gas concentrations, orbital forcing, and freshwater forcing. The impact of deglacial meltwater on AMOC shapes regional temperature patterns. PaleoMist simulation shows a pronounced warming in the Bølling-Allerød (BA), a strong AMOC, and a moderate cooling during the Younger Dryas (YD) with an AMOC weakening. The opposite signature is found for GLAC1D. The PaleoMist simulation replicates, at least qualitatively, the BA/YD sequence: a warming in Greenland and Antarctica in the BA, a cooling northern North Atlantic, and a warming in Antarctica in the YD.

In addition, as the main goal, this study presents an efficient method for assimilating the temporal evolution of surface temperatures for the last deglaciation. In applying an ensemble Kalman filter approach, the study makes use of the advances in the parallel DA framework (PDAF). It is found that the DA solution depends strongly on the background evolution of the decaying ice sheets rather than the assimilated temperatures. Further, the influence of DA is more pronounced on regional scales than on the global mean. In particular, DA has a stronger effect during millennial warming and cooling phases, such as BA and YD, especially at high latitudes with heterogeneous temperature patterns.
In the final step, the DA technique is developed to assimilate the subsurface temperatures. The results show the DA of subsurface temperatures modifies the precipitation pattern, which can consequently change the timing and magnitude of climate events such as BA and YD. The DA technique introduced and developed in this dissertation facilitates the paleoclimate DA on multi-millennial time scales and can also be employed to study future warming scenarios.

# Publications

- **Masoum, A.**, Nerger, L., Willeit, M., Ganopolski, A., & Lohmann, G. (2024). Paleoclimate data assimilation with CLIMBER-X: An ensemble Kalman filter for the last deglaciation. Plos one, 19(4), e0300138.
- **Masoum, A.**, Nerger, L., Willeit, M., Ganopolski, A., & Lohmann, G. (2024). Lessons from transient simulations of the last deglaciation with CLIMBER-X: GLAC1d versus PaleoMist. Geophysical Research Letters, 51(16), e2023GL107310.
- **Masoum, A.**, Nerger, L., Willeit, M., Ganopolski, A., & Lohmann, G. (2024). Assimilation of subsurface temperatures into the last deglaciation simulation. *In preparation.*

# Acknowledgements

I extend my deepest gratitude to my first supervisor, Prof. Gerrit Lohmann, whose guidance, expertise, and unwavering support have been invaluable throughout this journey. Your mentorship has shaped both my research and personal growth.

I am also grateful to my second supervisor, Dr. Lars Nerger, for your insightful feedback, encouragement, and dedication to excellence. Your constructive criticism has greatly enriched the quality of this thesis.

Special thanks are also given to Dr. Matteo Willeit for his patient support with the model and helpful feedback about the peer-reviewed papers based on this thesis. Furthermore, I would like to thank Dr. Andrey Ganopolski for his tips and contributions in writing peer-reviewed papers.

Many thanks also to the entire Paleoclimate Dynamics section at AWI for their invaluable support, engaging conversations, and creating such a positive and collaborative working environment.

Lastly, to my beloved wife, Sahar, your love, patience, and unwavering support have sustained me through the challenges of pursuing this PhD. Your belief in me never wavered, and your presence has been my anchor. Thank you for understanding the demands of this journey and for always being my source of strength.

# Contents

# Acronyms

**AMOC** Atlantic Meridional Overturning Circulation.

**BA** Bølling-Allerød.

**BP** Before Present.

**DA** Data Assimilation.

**EMIC** Earth System Model of Intermediate Complexity.

**EnKF** Ensemble Kalman Filter.

**EnSRF** Ensemble Square Root Filter.

**EOF** Empirical Orthogonal Function.

**ESTKF** Error Subspace Transform Kalman Filter.

**GCM** General Circulation Model.

**GHG** Greenhouse Gas.

**GMSST** Global Mean Sea Surface Temperature.

**IPCC** Intergovernmental Panel on Climate Change.

**kyr** thousand years.

**LESTKF** Local Error Subspace Transform Kalman Filter.

**LGM** Last Glacial Maximum.

**MWP-1A** Major Meltwater Pulse 1A.

**NH** Northern Hemisphere.

**PDA** Paleoclimate Data Assimilation.

**PDAF** Parallel Data Assimilation Framework.

**PDF** Probability Density Function.

**PF** Particle Filter.

**PI** Pre-Industrial.

**PMIP4** Protocol of the Intercomparison Project Phase 4.

**SESAM** Semi-Empirical Statistical-Dynamical Atmosphere Model.

**SH** Southern Hemisphere.

**SSS** Sea Surface Salinity.

**SST** Sea Surface Temperature.

**YD** Younger Dryas.

# List of Figures

# List of Tables

# Chapter 1

# Introduction

## 1.1 Motivation

Understanding climate dynamics raises critical questions in environmental science, including: How have past climate fluctuations shaped current patterns, and what factors drove these changes? What role does human activity play in altering the global climate, and how can these effects be separated from natural variability? What are the inherent limits of environmental systems in terms of frequency and intensity of events, and how do changes in factors like greenhouse gas concentrations and ice coverage affect these boundaries? Which key drivers, such as greenhouse gases and solar variations, will most significantly influence climate change over societal timescales? Addressing these inquiries necessitates robust paleoclimate research. Past climates provide essential insights into the drivers, variability, and evolution of the climate system, which are particularly relevant for understanding current anthropogenic climate change (Alley, 2003; Hargreaves et al., 2007; Rice et al., 2009; Schmidt, 2010; Snyder, 2010; Bell et al., 2013; Ault et al., 2014; Coats et al., 2020). They serve as analogues for potential future warm climate states (Overpeck et al., 2006; Burke et al., 2018; Tierney et al., 2020a), provide reference points for modern climate comparisons (Gulev et al., 2021), and help quantify both natural and forced climate variability (Cane et al., 2006; Cook et al., 2011; Goosse et al., 2012a; Ault et al., 2013; Fernández-Donado et al., 2013; Fang et al., 2021). Furthermore, by offering targets for assessing climate model performance, the study

of past climates enhances climate forecast accuracy and supports the development of more effective adaptation strategies (Crowley, 1991; Hargreaves and Annan, 2009; Schmidt et al., 2013; Zhu et al., 2021; Gulev et al., 2021).

The last deglaciation, 20-10 thousand years (kyr) before the present (BP), is a particularly useful period for paleoclimatic inquiry. During the last deglaciation, all climate components encountered large-scale changes. From a cold Last Glacial Maximum (LGM), the climate state transited to the warm interglacial state. This transition was triggered by insolation and geochemical processes (Paillard, 2015). Furthermore, greenhouse gas (GHG) concentrations rose by 80-100 ppm (Monnin et al., 2001; Spahni et al., 2005; Veres et al., 2013) and ice sheets melted, and positive feedbacks occurred (Clark et al., 2012). As a result, the atmospheric and oceanic circulation experienced significant changes (e.g., Löfverström and Lora, 2017; Pöppelmeier et al., 2023), and the global mean sea level rose by about 100-130 m (e.g., Lambeck et al., 2014; Gowan et al., 2021). However, these changes did not happen steadily; some abrupt events, pronounced in Greenland ice records, such as the warming during the Bølling-Allerød (BA; Clark et al., 2002; Weaver et al., 2003) or the cooling during the Younger Dryas (YD; Carlson et al., 2007) occurred during the last deglaciation.

Understanding the last deglaciation is not only important for reconstructing past climates but also for predicting future climate dynamics. The insights gained from this period help scientists refine their models and improve predictions of how current and future increases in GHGs will affect global temperatures, sea levels, and ice sheet stability. As we face unprecedented rates of climate change due to anthropogenic influences, the lessons learned from the last deglaciation become increasingly relevant. They remind us of the inherent sensitivity of the Earth's climate system and the potential for rapid and significant changes in response to both natural and human-induced forcings (Clark et al., 2012).

There are two traditional approaches to studying past climates: proxy-based reconstructions and climate model simulations. Proxy-based reconstructions utilize various natural recorders of climate variability, such as tree rings, ice cores, sediment layers, and corals, to reconstruct past climates. The proxy data, when carefully

calibrated and interpreted, can offer valuable insights into past climate conditions, allowing researchers to piece together climate variability and trends over millennia (e.g., Consortium et al., 2017) or deeper time in the past (e.g., McManus et al., 2004; Shakun et al., 2012; Marcott et al., 2013). However, the accuracy and spatial resolution of proxy data can be limited by the sparsity of proxy records and the potential for observational errors, which can affect the reliability of the reconstructions. Additionally, the relationships between proxies and the targeted climate variables are often established using empirical, typically linear, statistical approaches or proxy system modeling. Many proxy reconstructions also assume stationary teleconnections between local and large-scale climate variables, an assumption that often does not hold in reality.

In contrast, climate model simulations depend on the physical laws and dynamic mechanisms governing the climate system to provide continuous spatiotemporal variations of past climates (e.g., Crowley, 2000; Otto-Bliesner et al., 2006; Jungclaus et al., 2010; Zhu et al., 2020; Kapsch et al., 2022; Bouttes et al., 2023). These models simulate the interactions between the atmosphere, oceans, land surface, and ice, providing a comprehensive view of the climate system's behavior over time. Climate models are advantageous because they offer detailed, physically consistent scenarios of climate dynamics. However, they are also subject to uncertainties due to limitations in representing complex processes and the chaotic nature of the climate system (Deser et al., 2012). Combining the two approaches, proxy-based reconstructions and climate model simulations, allows for cross-validation and a more robust understanding of past climate variability, leveraging the strengths of each method to improve the accuracy and reliability of climate reconstructions (e.g., Phipps et al., 2013; Goosse, 2015).

An alternative method to the above-mentioned methods for reconstructing past climates is data assimilation (DA), which merges the information from models and proxy-based reconstructions. The Intergovernmental Panel on Climate Change (IPCC) defines DA as follows:

"Data assimilation is a mathematical method used to combine different sources of information in order to produce the best possible estimate of the state of a

system. This information usually consists of observations of the system and a numerical model of the system evolution. Data assimilation techniques are used to create initial conditions for weather forecast models and to construct reanalyses describing the trajectory of the climate system over the time period covered by the observations." (Arias et al., 2023)

DA has been recently applied to reconstruct, for instance, the climate of the past millennium (e.g. Goosse et al., 2010, 2012a; Hakim et al., 2016; Franke et al., 2017; Neukom et al., 2019a,b; Tardif et al., 2019; Erb et al., 2022), LGM (e.g., Kurahashi-Nakamura et al., 2017; Tierney et al., 2020b), YD (Renssen et al., 2015), and for the last glacial termination (Osman et al., 2021). The motivation behind DA is to jointly use model simulations and paleoclimate information to estimate the most likely state and trajectory. In a DA system, the data provide climate information at the sites, and the model fills in the missing information about the other locations by adding model dynamics and error bars from the data and the model (Fang and Li, 2016). DA results align with the information contained in observations and the physical mechanisms represented by the models. Furthermore, DA outcomes consistently outperform observations and simulations alone (Talagrand, 1997; Bouttier and Courtier, 2002; Robinson and Lermusiaux, 2000; Li, 2014).

Despite the potential of DA in paleoclimate, these methods have been used rather modestly in paleoclimate reconstructions due to the relative novelty of DA as a reconstruction method. Paleoclimate applications pose unique challenges for assimilation frameworks, leading to a significant focus on developing DA algorithms for various paleoclimate contexts (e.g., Bhend et al., 2012; Dirren and Hakim, 2005; Steiger et al., 2014; Mairesse et al., 2013; Dubinkina et al., 2011; Franke et al., 2020; Dee et al., 2016; King et al., 2021; Parsons et al., 2021; Tierney et al., 2020b; Osman et al., 2021). Furthermore, DA methods are challenging to implement due to their multifaceted requirements. This dissertation contributes to developing paleoclimate DA frameworks by presenting a fast DA technique for long-term paleoclimate simulations such as the last deglaciation.

## 1.2 Objectives & Structure of the Thesis

This dissertation focuses on the transient simulation of the last deglaciation, the development of paleoclimate DA methodology and the subsequent reconstruction of climate variables during this period. It is written based on the following objectives:

1. **To investigate the impact of a novel ice-sheet reconstruction on the simulation of the last deglaciation and to examine the roles of GHGs and orbital forcings in this context.** (Chapter 4)

   Due to uncertainty in ice-sheet evolution and the meltwater derived from them, transient simulations of the last deglaciation (e.g., Liu et al., 2014; Kapsch et al., 2022; Bouttes et al., 2023) show discrepancies in terms of global mean surface temperature and the Atlantic meridional overturning circulation (AMOC) strength compared to the proxy-based reconstructions (e.g., McManus et al., 2004; Shakun et al., 2012; Marcott et al., 2013; Osman et al., 2021), particularly during the BA and YD. Hence, the protocol of the Intercomparison Project Phase 4 (PMIP4) protocol prescribes two reconstructions, GLAC1D, and ICE-6G, as boundary conditions for ice-sheet evolution. These reconstructions are calculated by inverse modeling and exhibit notable uncertainties, attributed mainly to the viscosity model employed for the solid Earth. To address the uncertainty caused by ice-sheet reconstruction, a new ice-sheet reconstruction, PaleoMist (Gowan et al., 2021), that is used for the first time as an ice-sheet boundary condition for the last deglaciation, is employed in this study. PaleoMist reconstructs the ice sheets using different methodologies and prescribes the different freshwater schemes in the last deglaciation simulation. An Earth system model of intermediate complexity (EMIC), CLIMBER-X (Willeit et al., 2022), conducts the simulations in this study. EMICs are well-suited for long-term climate system integrations (Claussen et al., 2002) and are capable of simulating deglaciation (Charbit et al., 2005; Bonelli et al., 2009; Ganopolski and Calov, 2011; Heinemann et al., 2014). The deglacial climate, as simulated with PaleoMist, is evaluated by comparing it with the GLAC1D simulation. Moreover, the role of the other two forcings prescribed

by the PMIP4 protocol, GHG and orbital, is examined during the last termination with respect to the underlying ice sheets and by isolating the effects of orbital, GHG, and ice sheets.

2. **To design and implement a DA technique for the transient simulation of the last deglaciation.** (Chapter 5)

   Previous studies of DA in paleoclimate have focused primarily on the Holocene (e.g., Steiger et al., 2018; Tardif et al., 2019). Moreover, they largely focused on reconstructing one observed variable, mainly surface temperature, and did not investigate the effect of DA on the model performance in simulating other climate variables. In general, they employed the offline approach, in which the initial conditions for the next DA-cycles are not analyzed (e.g. Steiger et al., 2014) and used different existing simulations as the model background states (e.g. Osman et al., 2021; Erb et al., 2022) in their DA system to avoid the enormous computational cost of long-term transient simulations. However, they did not determine how the quality of the model states, which can be influenced by boundary settings, affects DA solutions for past climate reconstructions. In this dissertation, an online DA technique is designed to be conducted during the transient simulation of the last deglaciation. In the online approach, states are chosen from a dynamically evolving set of parallel model simulations. The state variables of these simulations are iteratively refined by assimilating proxy records (e.g., Perkins and Hakim, 2017). Surface temperatures from oceanic and terrestrial paleoclimate records of the recent deglaciation are assimilated. The model is also equipped with a Parallel Data Assimilation Framework (PDAF; Nerger and Hiller, 2013), providing an efficient variant of the ensemble Kalman filter (EnKF) algorithm (Evensen, 2003) as well as a stochastic emulator mimicking internal variability in the model. The effects of DA on climate trajectories are evaluated, and the results for the different ice sheet reconstructions, GLAC1D and PaleoMist, are compared to understand the influence of background states in the DA system.

3. **To investigate the effect of the assimilation of oceanic subsurface temperatures on the simulation of the last deglaciation.** (Chapter 6)

   Several studies investigate the importance of subsurface temperatures as potential predictors for abrupt changes in deglacial AMOC (e.g., Rühlemann et al., 2004; McManus et al., 2004; Knorr and Lohmann, 2007; Zhang et al., 2017). For example, Max et al. (2022) demonstrate a consistent trend of accelerated warming in the subsurface ocean preceding the onset of each Heinrich Event over the last 27 kyr.

   In addition, Okazaki et al. (2021) indicate that online DA surpasses offline DA when the predictability length exceeds the averaging time of observations. Moreover, a direct correlation exists between predictability length and the efficacy of online DA, with the ocean's influence being pivotal in extending predictability, thus enhancing the performance of online DA over offline methods (Okazaki et al., 2021). Since temperature variations occur more gradually in deeper layers than in the surface layer, incorporating subsurface temperature assimilation enhances DA proficiency. Therefore, as a logical step to develop the DA methodology outlined in Chapter 5, the subsurface temperatures are assimilated into the model, and its effect on abrupt events, such as BA, is evaluated.

This thesis is structured as follows: Chapter 2 overviews the climate system, climate forcings in Glacial-Interglacial cycles, the last deglaciation, and DA in paleoclimate scales. Chapter 3 gives an explanation of the climate model, framework used for the implementation of DA, and DA algorithm. Chapter 4 investigates the effect of different ice-sheet reconstructions in the last deglaciation's simulations and has been submitted in *Geophysical Research Letters*. Chapter 5 presents a DA technique for the last deglaciation simulations and has been published in (Masoum et al., 2024) in *Plos One*. Chapter 6 develops the DA technique for assimilating subsurface temperatures in the last deglaciation simulation. Chapter 7 concludes and summarizes this study.

# Chapter 2

# Theory

## 2.1 The Climate System

According to the IPCC (Masson-Delmotte et al., 2021), climate is defined as: "Climate in a narrow sense is usually defined as the average weather, or more rigorously as the statistical description in terms of the mean and variability of relevant quantities over a period of time ranging from months to thousands or millions of years. The classical period for averaging these variables is 30 years, as defined by the World Meteorological Organization. The relevant quantities are most often surface variables such as temperature, precipitation, and wind. Climate in a wider sense is the state, including a statistical description, of the climate system." The IPCC divides the climate system into five components:

- **The Atmosphere:** This is the Earth's gaseous envelope, divided into four layers: the troposphere, stratosphere, mesosphere, and thermosphere (Wallace and Hobbs, 2006). The troposphere, the lowest layer, contains approximately 80% of the atmosphere's mass and is where cloud formation and weather phenomena occur (Kikstra et al., 2022). The atmosphere consists mainly of nitrogen (78%), oxygen (21%), and argon (0.9%). Trace gases, though present in small quantities, play significant roles in the hydrological cycle (e.g., water vapor), the global carbon cycle (e.g., methane), and the greenhouse gas effect (e.g., water vapor, carbon dioxide, nitrous oxide, methane). Due to its low heat capacity and density, atmospheric processes operate on relatively short

time scales, ranging from weeks to months (Wallace and Hobbs, 2006).

- **The Hydrosphere:** This contains all of Earth's liquid surface and subterranean water, including oceans, lakes, rivers, and groundwater (Kikstra et al., 2022). Oceans, representing about 97% of Earth's water masses (Gleick, 1993), have a total mass approximately 250 times that of the atmosphere (Wallace and Hobbs, 2006), making them significant sinks for heat and anthropogenic carbon. Hydrospheric processes span a wide range of temporal and spatial scales, from small-scale eddies to Thermohaline Circulation (THC), a system of currents driven by salinity and temperature gradients and momentum exchange with the atmosphere. While exchange with the atmosphere and upper ocean mixing occur on relatively short time scales up to months, deep ocean exchanges occur on millennial time scales.

- **The Cryosphere:** This includes all frozen water masses on and below the land and ocean surfaces, such as snow, glaciers, ice sheets, ice shelves, icebergs, and sea ice. Frozen water constitutes approximately 2.2% of Earth's water masses (Shikazono and Shikazono, 2012), with the largest share in the Antarctic and Greenland ice sheets. Ice shelves are floating extensions of ice sheets that cover parts of the ocean surface. Calving, the process where ice breaks off from the edge of ice shelves, creates icebergs that transport freshwater, heat, and nutrients from ice shelves into the open ocean. Due to their high reflectivity (albedo), ice masses significantly affect the heat uptake of land and ocean surfaces. While sea ice varies seasonally, ice sheet buildup and dissolution occur over multi-millennial time scales.

- **The Lithosphere:** This is the upper layer of the solid Earth, including the crust and the elastic uppermost part of the mantle (Kikstra et al., 2022). The Earth's crust is divided into continental and oceanic plates that float on the denser, viscous mantle and move a few centimeters yearly (Wallace and Hobbs, 2006). Plate collisions can result in volcanic eruptions and the rise of mountain ranges, such as the Himalayas and the Rocky Mountains (Wallace and Hobbs, 2006). These tectonic activities shape Earth's topography and sea

floor, affect global sea levels, and exchange matter, energy, and momentum with other Earth system components. The time scales for these processes range from $10^7$ to $10^8$ years.

- **The Biosphere:** This encompasses all living organisms on Earth and their interactions with other Earth system components. Key biospheric processes include photosynthesis, which produces biomass from carbon dioxide and water using solar energy, and respiration, which releases energy by decomposing biomass. Biomass that is not decomposed forms natural carbon sinks, such as coal and oil reservoirs and peatlands. The biosphere is crucial in exchanging carbon, water, and energy with the atmosphere and the ocean. It also affects Earth's albedo and surface roughness and is a source of aerosols, impacting the atmospheric energy budget. Biospheric processes occur on time scales ranging from hours to centuries (Stocker, 2011).

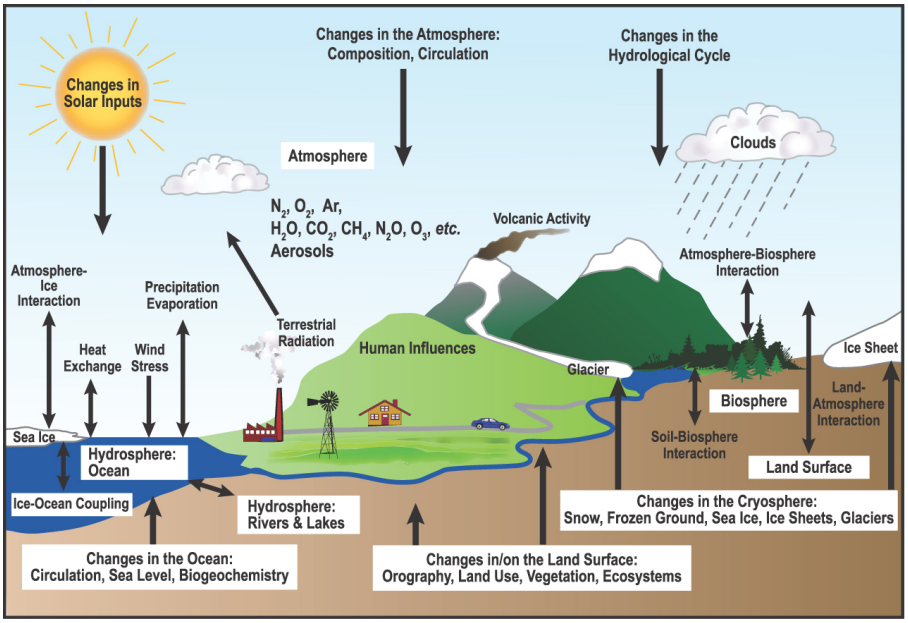


Figure 2.1: Schematic view of the climate system components, their processes, and interactions. The figure has been taken from Change (2007).

Figure 2.1 shows in a simplified way that the climate components do not exist in isolation; rather, they are interconnected and interact on multiple levels, both directly and indirectly. The system as a whole is driven by solar radiation and evolves under the influence of its internal dynamics through ocean currents and atmospheric

circulation. Additionally, external factors, known as forcings, drive the system, i.e., a mechanism that puts energy into the system and thus enables it to maintain a state far away from the thermodynamic equilibrium. All of the forcing mechanisms combined with all internal feedback mechanisms over all timescales eventually cause climate variability. Peixoto and Oort (1992) categorizes the forcings as follows:

**- External Climate Forcings**

- Changes in solar output: The solar irradiance is only 341 $W.m^{-2}$ on average. Physical processes within the sun lead to a so-called solar cycle, which modulates the irradiance by $\pm 0.5$ $W.m^{-2}$ with a periodicity of 11 years. Of negligible importance on timescales below tens of millions of years is the sun's ageing, leading to an increase in luminosity of around 1% per $10^8$ yr.

- Orbital changes: The Earth's orbit around the Sun is characterized by three parameters, each of them showing long-term variations that eventually influence how much energy the Earth receives from the Sun: The axial precession (periodicities 19 kyr and 23 kyr), the obliquity of the ecliptic (periodicity 4l kyr) and the eccentricity of the orbit (periodicities 100 kyr and 400 kyr) (Milankovitch, 1941).

**- Internal Climate Forcings**

- Atmospheric composition: All atmospheric gases consisting of molecules with an electric dipole moment, e.g., $CO_2$, $CH_4$, $H_2O$, and $N_2O$, absorb parts of the outgoing terrestrial long-wave radiation (so-called greenhouse gases). The energy is then either partly re-emitted towards Earth or thermalized in the Atmosphere, effectively increasing the temperature (Wallace and Hobbs, 2006). Similarly, atmospheric aerosols, for instance, from volcanoes, may absorb long-wave radiation (e.g., soot particles) or scatter incoming short-wave radiation back into space (e.g., $H_2SO_4$ droplets) (Boucher and Boucher, 2015).

- Changes in albedo: The albedo determines which share of the incoming solar radiation is scattered back into space by clouds and land surfaces. Consequently, variations in the vegetation, soil composition, or snow/ice cover modulate the amount of energy that is taken up by the Climate System.

- Changes in plate tectonics: The location of the continents plays a crucial role in terms of how much incoming energy the Earth absorbs due to differences between land and sea albedo. Processes like pole wandering and continental drifts occur on timescales ranging from $10^7$ yr to $10^9$yr (Peixoto and Oort, 1992).

Knowing about the timescales of all forcings and feedback mechanisms is particularly important to identify the causes of climate signals, i.e., any trends or patterns that can be observed in time series of climate variables.

### 2.1.1 Climate Forcings in Glacial-Interglacial Cycles

Paleoclimatic records reveal a sequence of glacial-interglacial cycles spanning the last 800 kyr in ice cores (community, 2004) and several million years in deep oceanic sediments (Lisiecki and Raymo, 2005) and loess (Ding et al., 2002). The past 430 kyr, the most thoroughly documented period, is characterized by 100 kyr glacial-interglacial cycles of significant amplitude, alongside considerable climate changes corresponding to other orbital periods (Hays et al., 1976) and millennial time scales (McManus et al., 2002; Project, 2004). On average, only 20% of each glacial-interglacial cycle was spent in the warm interglacial mode, typically lasting between 10 to 30 thousand years (Figure 2.2). There is evidence of longer interglacial periods between 430 and 740 kyr ago, which appear to have been colder than the typical interglacials of the late Quaternary (community, 2004). The Holocene, the most recent of these interglacials, continues to the present.

The ice core records demonstrate that GHGs co-varied with Antarctic temperatures over glacial-interglacial cycles, indicating a close link between natural atmospheric GHGs fluctuations and temperature. Over the last 420 kyr, $CO_2$ variations broadly followed Antarctic temperature changes, usually lagging by several centuries to a millennium (Mudelsee, 2001). The sequence of climatic forcings and responses during deglaciations, transitioning from full glacial conditions to warm interglacials, is well-documented. High-resolution ice core records of temperature proxies and $CO_2$ during deglaciations show that Antarctic temperatures rose several hundred years before $CO_2$ levels (Monnin et al., 2001; Caillon et al., 2003). During the

last deglaciation, and likely the three preceding ones, warming commenced at high southern and northern latitudes several thousand years before the first significant sea level rise, which resulted from the melting of northern ice sheets linked to rapid warming at high northern latitudes (Petit et al., 1999; Shackleton, 2000; Pépin et al., 2001). Current data do not precisely determine whether warming began earlier in the Southern Hemisphere (SH) or Northern Hemisphere (NH), but a notable deglacial feature is the inter-hemispheric differences in the magnitude and timing of strong reversals in the warming trend, which are not in phase between the hemispheres and are more pronounced in the NH (Blunier and Brook, 2001).

In addition, modeling studies have provided substantial evidence supporting the significant role of variations in Earth's orbital parameters in driving long-term climate variability. Specifically, simulations using General Circulation Models (GCMs) (e.g., Carlson et al., 2012; Herrington and Poulsen, 2011) corroborate the core principle of the Milankovitch theory (Milankovitch, 1941), which posits that a reduction in NH summer insolation leads to sufficient cooling to trigger ice sheet expansion. Climate-ice sheet models of varying complexities, when forced by changes in orbital parameters and reconstructed atmospheric $CO_2$ levels, simulate ice volume variations and other climate features over the last and several preceding glacial cycles that align with paleoclimate records (Abe-Ouchi et al., 2007; Bonelli et al., 2009; Ganopolski et al., 2010).

There is high confidence that orbital forcing is the primary external driver of glacial cycles (Kawamura et al., 2007; Cheng et al., 2009; Lisiecki, 2010; Huybers, 2011). Nonetheless, atmospheric $CO_2$ levels serve as a crucial internal feedback mechanism. Over the past several hundred thousand years, $CO_2$ concentration variability on an orbital scale has covaried with proxy records, including reconstructions of global ice volume (Lisiecki and Raymo, 2005), climatic conditions in central Asia (Prokopenko et al., 2006), tropical (Herbert et al., 2010) and Southern Ocean SST (Pahnke et al., 2003; Lang and Wolff, 2011), Antarctic temperatures (Parrenin et al., 2013), deep-ocean temperatures (Elderfield et al., 2010), biogeochemical conditions in the North Pacific (Jaccard et al., 2010), and deep-ocean ventilation (Lisiecki et al., 2008). These close linkages between $CO_2$ levels and climate variability are consistent

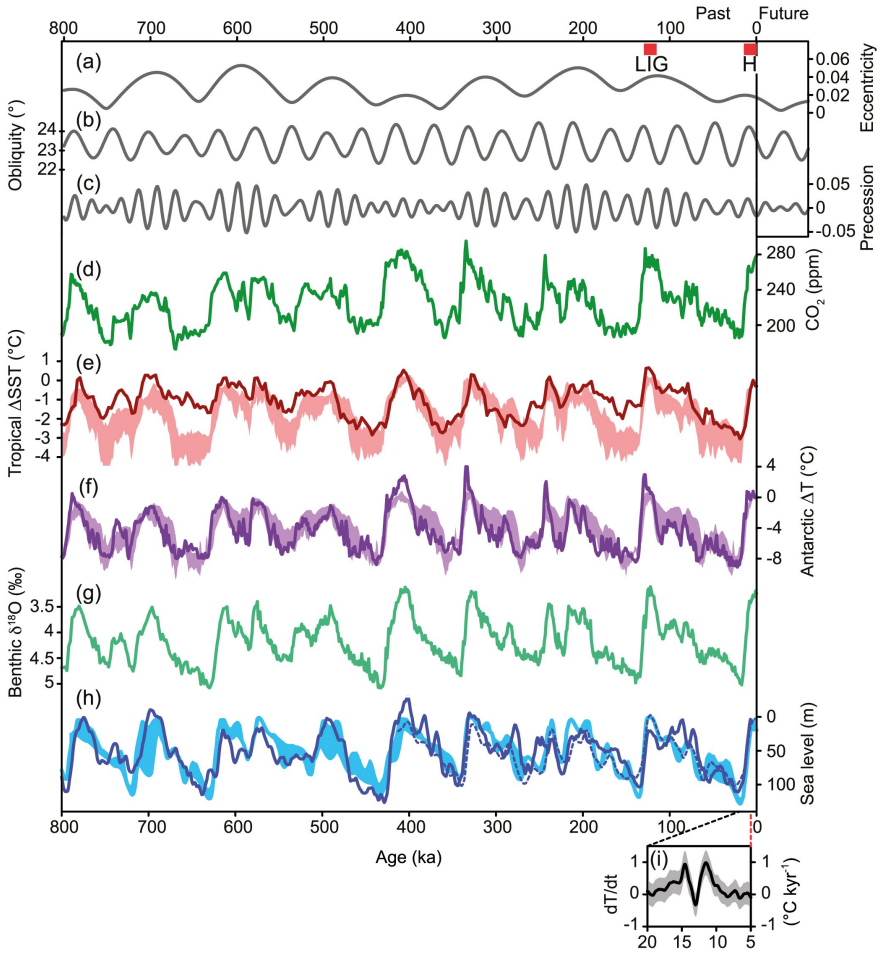


Figure 2.2: Orbital parameters and proxy records over the past 800 kyr. (a) Eccentricity. (b) Obliquity. (c) Precessional parameter. (d) Atmospheric concentration of $CO_2$ from Antarctic ice cores. (e) Tropical sea surface temperature (SST) stack. (f) Antarctic temperature stack based on up to seven different ice cores. (g) Stack of benthic $\delta^18O$, a proxy for global ice volume and deep-ocean temperature. (h) Reconstructed sea level. Lines represent orbital forcing and proxy records, shaded areas represent the range of simulations with climate models forced by variations of the orbital parameters and the atmospheric concentrations of the major GHGs. (i) Rate of changes of global mean temperature during the last deglaciation based on Shakun et al. (2012). The figure has been taken from Masson-Delmotte et al. (2013).

with modeling results that indicate with high confidence that glacial-interglacial variations of $CO_2$ and other GHGs explain a significant portion of glacial-interglacial climate variability in regions not directly influenced by NH continental ice sheets (Timmermann et al., 2009; Shakun and Carlson, 2010).

### 2.1.2 Last Deglaciation

It is highly probable that the global mean surface temperature rose by 3°C to 8°C during the last deglaciation, with an average rate of change likely between 0.3 to 0.8°C per thousand years. The deglacial global warming occurred in two major phases from 17.5 to 14.5 kyr ago and from 13.0 to 10.0 kyr BP, with peak rates of change likely reaching between 1°C and 1.5°C per thousand years at the millennial scale (Shakun et al., 2012). Higher rates may have been observed regionally and over shorter timescales, especially during a series of abrupt climate change events. Paleoclimate records indicate that the deglaciation period was not a smooth, gradual process but was punctuated by abrupt climatic events. These events include the BA warm period and the subsequent YD cold interval. The BA, occurring around 14.7 to 12.7 ky BP, was characterized by rapid warming and significant glacial melt. However, this warm phase was abruptly interrupted by the YD, a period of sudden cooling that lasted for about 1,200 years. The cause of the YD is still debated, but it is commonly attributed to the massive release of freshwater from the melting ice sheets, which disrupted the AMOC (Alley, 2003; Clark et al., 2002).

The end of the YD marked the final phase of the deglaciation, leading to the onset of the Holocene epoch. During this period, temperatures rapidly increased, leading to the further retreat of ice sheets and rising sea levels. This transition also saw significant shifts in vegetation and animal populations as ecosystems adapted to the changing climate. The stabilization of climate conditions during the early Holocene provided a more favorable environment for human societies, fostering the development of agriculture and the rise of civilizations (Fischer et al., 1999; Shuman et al., 2002).

A comprehensive temperature reconstruction for the last glacial termination (Shakun and Carlson, 2010) indicates that SH temperature changes preceded those in the NH. This lead is explained by the bipolar thermal seesaw concept (Stocker and Johnsen, 2003) and related shifts in inter-hemispheric ocean heat transport triggered by a weakening of the AMOC during the last glacial termination (Ganopolski and Roche, 2009). Additionally, the rapid response of sea ice to changes in austral spring insolation (Stott et al., 2007; Timmermann et al., 2009) further accounts for

SH warming preceding NH warming. These mechanisms suggest that the SH temperature lead over the NH is fully consistent with NH orbital forcing of deglacial ice volume changes (high confidence) and the pivotal role of climate-carbon cycle feedbacks in glacial-interglacial transitions. The close coupling is underscored by the near-zero lag between the deglacial rise in $CO_2$ and the average deglacial Antarctic temperature reported from improved estimates of gas-ice age differences (Pedro et al., 2012; Parrenin et al., 2013).

## 2.2 Paleoclimate Data Assimilation (PDA)

DA is an optimization method originating in atmospheric and oceanic sciences. It allows the combination of optimal information from observations with models of the earth system to estimate geophysical fields of interest accurately (Wang, 1999). DA enables the quantitative estimation of uncertainties in observations and simulations and uses observations to constrain model trajectories effectively. The results updated through DA are consistent with both the information contained in observations and the physical mechanisms represented by models, ensuring that these results are superior to those derived from observations and simulations alone (Talagrand, 1997; Bouttier and Courtier, 1999; Robinson and Lermusiaux, 2000; Li et al., 2007; Li, 2014).

In past climate research, DA offers a promising method for obtaining better estimates of historical climate states. The basic concept behind PDA is to constrain a climate model trajectory using proxy data and an observation operator, such as a forward model, to estimate past climate optimally. This method combines climate signals recorded in proxies with the physical understanding of the climate system represented by climate models, allowing for the effective handling of errors in both proxy data and simulation results. Consequently, estimated climate variations using DA are generally consistent with both the recorded climate signals and the physical laws and dynamic mechanisms represented by climate models (Widmann et al., 2010; Hakim et al., 2013). As Edwards et al., 2013 stated, PDA is a "best-of-both-worlds" method for estimating time slices in the past.

Since von Storch et al. (2000) first introduced the DA concept into paleoclimatology, various DA methods have been applied in paleoclimate research. These include nudging (von Storch et al., 2000), Bayesian estimation (Hargreaves and Annan, 2002), forcing singular vectors (Barkmeijer et al., 2003), ensemble square root filter (EnSRF; e.g., Pendergrass, 2009; Pendergrass et al., 2012; Bhend et al., 2012; Osman et al., 2021), and particle filter (PF; e.g., Dubinkina et al., 2011; Goosse et al., 2012b). Nudging and forcing singular vectors add an artificial forcing term to forecast equations to drive results forward based on observations, with the main difference being how the forcing term is constructed. EnSRF, a variant of EnKF, and PF are ensemble methods based on Bayesian estimation, which are widely used for their effectiveness in nonlinear and non-Gaussian systems. Although variational DA methods have been utilized in projects like the Twentieth Century Reanalysis (Whitaker et al., 2004; Compo et al., 2011), they are less suitable for reconstructing past climate due to the sparse nature of observations over longer timescales, whereas EnKF has performed well in such scenarios (Widmann et al., 2010). Bhend et al. (2012) further showed that variational methods are not ideal for PDA due to the limited number of observations and climate proxies.

The process of PDA involves using initial conditions and forcings to run climate model simulations. Assimilation operations commence after the model reaches equilibrium via a "spin-up" period. Observations during assimilation are either proxy-based reconstructions of climate variables or original proxy data. The assimilation of these observations requires either a simple transformation matrix or a forward model, depending on the type of data. The updated climate variables, termed "analysis values," are obtained by recursively activating the DA operation over the period of interest, providing optimal estimations of climate states over time and space (Dirren and Hakim, 2005; Steiger et al., 2014).

Although the theories of PDA and traditional DA in the fields of atmospheric, oceanic, and land surface sciences share the same theoretical foundations, PDA has unique characteristics. Firstly, PDA observations, such as proxies and proxy-based reconstructions, are time-averaged and continuous over time, whereas DA observations in other fields, such as in-situ observations and remote sensing data,

are usually instantaneous and discontinuous (e.g., Dirren and Hakim, 2005; Steiger et al., 2014). Prior to the instrumental observation epoch, direct observations of climate variables are generally unavailable, making proxy data the primary source for PDA. These proxy data are often insufficient and sparse in spatial coverage and represent average climate states over periods (Saltzman, 2002; Yu et al., 2007). Consequently, the time intervals of PDA are generally more than 10 years, which are significantly longer than the time steps and predictability of climate models (Lorenz, 1982; Kalnay, 2003; Reichler and Roads, 2003; Bhend et al., 2012).

Secondly, PDA requires long-term integration to reconstruct interannual, decadal, or centennial climate changes over hundreds of years or longer. This contrasts with DA in atmospheric, oceanic, and land surface sciences, focusing on short-term predictions (e.g., in the next 6 hours, 24 hours, or up to one month). Consequently, PDA demands higher computing performance and is more time-consuming (Huntley and Hakim, 2010). Thirdly, in the context of long-term climate research, initial conditions have minimal impact on results because their effects attenuate over time due to the chaotic nature of the atmosphere (Chou, 1983). Some studies have shown that the impact of initial conditions diminishes well before the end of the simulation cycle, making updating initial conditions unnecessary for PDA with longer intervals (Bhend et al., 2012; Annan and Hargreaves, 2012; Steiger et al., 2014). However, Okazaki et al. (2021) has indicated updating initial conditions improves the skill of the DA. These special aspects of PDA necessitate modifying or improving existing DA methods to study interannual, decadal, and centennial climate variability over large spatial and temporal scales (Widmann et al., 2010; Hakim et al., 2013).

### 2.2.1 Frequent PDA Algorithms

1) Nudging

Nudging is a sequential DA method that uses dynamic relaxation to adjust a model towards observations by adding an artificial forcing term to the governing equations (Kistler, 1974; Hoke and Anthes, 1976). This forcing term is proportional to the difference between observations and the model's forecasted equivalent. Nudging ensures that the model forecasts approximate available observations and maintains

dynamical coordination among various model variables. It also serves as the initial condition for subsequent simulations, enhancing prediction skills. von Storch et al. (2000) first introduced nudging into paleoclimatology, demonstrating its applicability and superiority. Nudging's simplicity, effectiveness, and ease of implementation make it suitable for DA with complex, non-linear models like coupled climate system models (Widmann et al., 2010). However, nudging cannot assimilate observations that models cannot forecast without converting them into forecasted variables first, and the relaxation factor assignment lacks a theoretical basis (von Storch et al., 2000).

2) PF

PF is a Bayesian estimation algorithm based on the Monte Carlo method, suitable for nonlinear and non-Gaussian systems (Gordon et al., 1993). It estimates the posterior probability density function (PDF) using weighted random particles in state space. The standard PF's ability to represent the posterior PDF accurately improves with the number of particles used. Prior to 2011, simplified or degenerated versions of PF were used in paleoclimate research, achieving satisfactory skill levels even with fewer particles under the constraint of high-quality proxies (Goosse et al., 2010; Crespin et al., 2009; Widmann et al., 2010). Advanced PF with residual resampling showed significant improvements, confirmed by further studies (Dubinkina et al., 2011; Annan and Hargreaves, 2012).

3) EnSRF

EnSRF is a deterministic DA algorithm based on EnKF, first proposed by Whitaker and Hamill (2002). EnSRF does not rely on perturbing observations and uses the Monte Carlo method to compute background error covariance, making it applicable to DA experiments with non-linear models and reducing computational demands. Dirren and Hakim (2005) adapted EnSRF for time-averaged observations in PDA, demonstrating its effectiveness. Huntley and Hakim (2010) found that the spatial distribution of proxies plays a significant role in DA skill, while Pendergrass et al. (2012) highlighted the importance of matching proxy temporal resolution with model variables. Steiger et al. (2014) showed that PDA results using EnSRF outperformed traditional methods like principal component analysis, especially in

regions with sparse proxy data.

### 2.2.2 Online vs Offline

Based on the DA approach to integrating proxy data and model simulations, PDA is categorized into two main approaches: online (e.g., Annan and Hargreaves, 2012; Goosse et al., 2012b) and offline (e.g., Steiger et al., 2014; Osman et al., 2021). The main differences between these two approaches can be explained as follows:

**Temporal Integration:** Online DA incorporates proxy data into the model simulation in real-time as the model runs. This allows for continuous updates and adjustments to the model state based on the available proxy information. On the other hand, offline DA uses pre-computed model simulations and combines them with proxy data after the model run is complete. This approach is less computationally intensive but may not capture the full temporal evolution of the climate system.

**Computational Resources:** Online DA typically requires more computational resources as it involves running the climate model and assimilating data simultaneously. This can be particularly demanding for complex Earth system models. Offline DA is generally less computationally expensive since it uses pre-existing model simulations. This makes it more feasible for longer time periods or when computational resources are limited.

**Feedback Mechanisms:** Online DA allows for immediate feedback between the assimilated proxy data and the model state. This can lead to more dynamically consistent reconstructions, as the model can adjust to new information in real-time (Perkins and Hakim, 2017; Okazaki et al., 2021). Offline DA lacks this immediate feedback, potentially resulting in reconstructions that are less dynamically consistent with the underlying climate physics.

**Uncertainty Quantification:** Online DA can provide more comprehensive uncertainty estimates by accounting for both model and proxy uncertainties throughout the simulation process. Offline DA may have limitations in fully capturing the propagation of uncertainties, especially those related to model dynamics.

**Temporal Resolution:** Online DA can potentially provide higher temporal res-

olution reconstructions, as it can incorporate proxy data at each time step of the model simulation. Offline DA is often limited to the temporal resolution of the pre-computed model simulations, which may be coarser than the available proxy data.

**Flexibility in Proxy Integration:** Online DA allows for more flexibility in incorporating new proxy data or updating existing proxies during the reconstruction process. Offline DA is less flexible, as it relies on pre-computed model simulations and may require rerunning the entire assimilation process to incorporate new proxy information.

In addition, there are two types of offline DA: transient offline DA and stationary offline DA. In transient offline DA, the background consists of an ensemble run for the same time period as the temporal resolution of the observations (Goosse et al., 006a; Bhend et al., 2012; Franke et al., 2017). Conversely, in stationary offline DA, the background remains the same at all analysis steps and consists of a single run (Steiger et al., 2014; Hakim et al., 2016; Tardif et al., 2019). Stationary offline DA is computationally efficient because it does not require an ensemble run. Steiger et al. (2014) demonstrated that this method outperforms the conventional climate field reconstruction method based on principal component analysis in reconstructing the surface temperature field, although its performance relative to transient offline DA is unclear.

In summary, while online paleoclimate DA offers advantages in terms of dynamic consistency, temporal resolution, and feedback mechanisms, it comes at the cost of higher computational requirements. Offline DA, although less dynamically consistent, provides a more computationally efficient approach for reconstructing past climate conditions, especially over longer time periods or when resources are limited.

### 2.2.3 PDA Challenges

One major issue is the uneven and sparse spatial distribution of existing proxies, coupled with a noticeable diversity among them. The influence of the spatial distribution of observations on the estimation skill of DA is significant. For regions far from observations, such as the SH and marine realms, updated DA re-

sults often show little to no improvement due to long-range "spurious correlations" (Houtekamer and Mitchell, 2001; Annan and Hargreaves, 2012; Anderson and Lei, 2013; Han et al., 2015). While covariance localization and observation localization can address these spurious correlations, they may also lead to non-optimized model states. Accurately quantifying proxies with qualitative characteristics for numerical calculation in DA also presents a significant challenge (Zhang and Jiang, 2004; Su et al., 2014).

Another issue is the difficulty in constructing forward models for proxies or the lack of explicit expressions for these models. PDA observations have primarily been proxy-based temperature reconstructions. Constructing reliable forward models for various proxies remains challenging. Although tree-ring proxies have a relatively mature forward model (Vaganov et al., 2006) validated for PDA (Breitenmoser et al., 2014), other proxies, like stable isotope $\delta^{18}$O in precipitation, still require validation for their forward models (e.g., Sturm et al., 2005; Fischer, 2006; Zhang et al., 2009; Tierney et al., 2020b).

The uncertainties of initial conditions and forcings are significantly greater in PDA than in DA for modern climate research. For modern climate research, initial conditions and forcings are derived from instrumental data, which generally show higher accuracy and lower uncertainty. In contrast, paleoclimate research relies on proxy-based reconstructions, which exhibit lower accuracy and higher uncertainty. Smerdon (2011) reported that the signal-to-noise ratios of proxies are representative of real-world conditions, indicating significant noise levels. These uncertainties in initial conditions and forcings in PDA can compromise the expected skill of past climate estimations (Steiger et al., 2014).

Verification of PDA results is another challenging issue. Unlike modern climate data, where actual past climate states can be accurately captured by instruments, PDA results for periods before the instrumental era (approximately 1850 to present) can only be indirectly verified by comparing them with other proxy-based reconstructions or climate model simulations. This lack of credible references makes it difficult to validate PDA outcomes effectively (Bhend et al., 2012).

# Chapter 3

# Model and Tools

## 3.1 CLIMBER-X

CLIMBER-X v1.0 is an EMIC that bridges the gap between computational efficiency and high-resolution climate simulations. The model is designed with a modular structure, encompassing a range of components that simulate the atmosphere, ocean, sea ice, and land surface processes. Each component operates on a regular latitude-longitude grid with a horizontal resolution of $5° \times 5°$, facilitating efficient data exchange and integration. CLIMBER-X stands out due to its ability to simulate the Earth system over extensive temporal scales, from decades to over 100 kyr, making it a powerful tool for both past climate reconstructions and future climate projections. The model achieves a remarkable throughput of around 10,000 simulation years per day on a high-performance computer with 16 CPUs, which is significantly faster than many state-of-the-art GCMs. This efficiency is achieved without compromising the model's ability to realistically reproduce many observed climate characteristics, providing a robust platform for studying long-term climate dynamics. The modular design of CLIMBER-X ensures that each component, from the atmosphere to the ocean and land surface, is finely tuned and validated against present-day and historical climate data, allowing for comprehensive climate simulations with detailed feedback and sensitivity analyses.

A simplified overview of the model is given in Figure 3.1. Version 1 of CLIMBER-X (https://doi.org/10.5281/zenodo.6877358) is used for Chapter 5 and Version 2 for

Chapter 4 and 6. In the following, the different model components are explained in more detail.

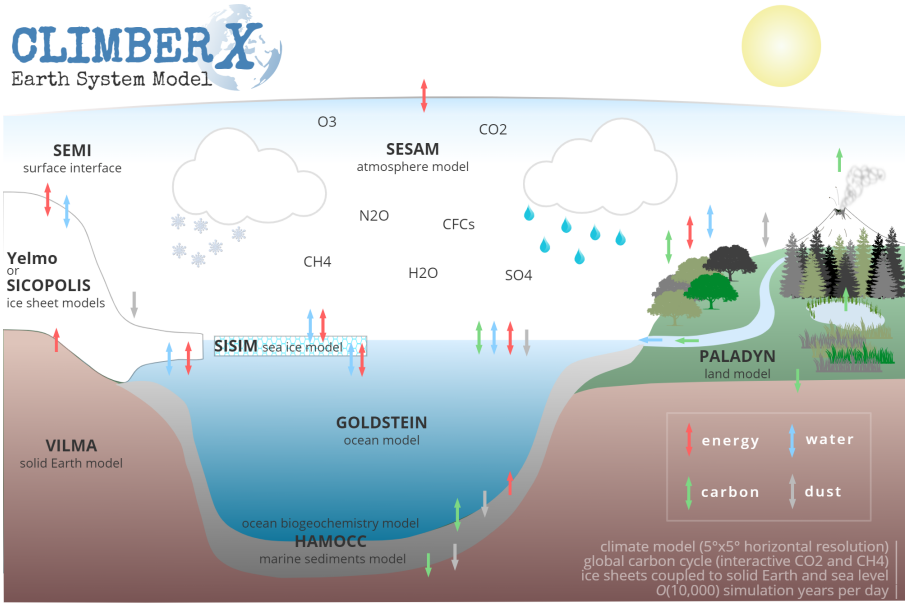


Figure 3.1: Schematic illustration of the CLIMBER-X model, including exchanges and coupling between the different components. Figure has been taken from Willeit et al. (2022).

### 3.1.1 Atmosphere Model (SESAM)

The atmospheric component of CLIMBER-X is called the Semi-Empirical Statistical-Dynamical Atmosphere Model (SESAM). SESAM operates on a $5° \times 5°$ grid and uses a semi-empirical approach, leveraging high-quality climatological data and complex climate model simulations. The model includes a 2.5-D representation where prognostic variables such as temperature, specific humidity, and eddy kinetic energy are 2-D, but horizontal energy and water transport, as well as vertical fluxes of longwave radiation, involve 3-D distributions. The vertical structure of the atmosphere is characterized using universal vertical profiles for temperature and relative humidity, while the horizontal wind velocity is divided into geostrophic and ageostrophic components. SESAM also incorporates cloud parameterizations based on atmospheric relative humidity, effective vertical velocity, and near-surface temperature inversion strength, along with comprehensive schemes for shortwave and longwave radiation (Petoukhov et al., 2000; Hansen et al., 1983; Feigelson et al., 1975).

### 3.1.2 Ocean Model (GOLDSTEIN)

The ocean component of CLIMBER-X is based on the 3-D frictional-geostrophic balance model GOLDSTEIN. GOLDSTEIN diagnoses horizontal and vertical ocean velocities using frictional-geostrophic balance and hydrostatic equilibrium, ensuring stable and realistic ocean dynamics without internal variability. The model utilizes an advection-diffusion equation for tracer transport, employing a flux-corrected transport scheme to minimize numerical diffusion. It also includes parameterizations for isopycnal and diapycnal mixing, as well as eddy-induced transport. The ocean model operates on the same $5^\circ \times 5^\circ$ grid as the atmosphere model and includes 23 vertical layers with varying thicknesses. Adaptations have been made to handle dynamic changes in the land-sea mask, ensuring continuous and realistic transitions in ocean properties (Edwards et al., 1998; Redi, 1982; Rahmstorf, 1993).

### 3.1.3 Sea Ice Model (SISIM)

SISIM, the Sea Ice Model in CLIMBER-X, is a dynamic-thermodynamic model with a single ice layer and a snow layer on top. SISIM computes the surface energy balance separately for ice-free and ice-covered areas within each oceanic grid cell. The model handles the accumulation and melting of snow and sea ice, considering both surface and basal processes. It includes temperature-dependent sea ice albedo, a parameterization for snow albedo, and accounts for conductive heat flux within the ice and snow layers. Sea ice dynamics are simulated using an elastic-viscous-plastic rheology and a flux-corrected transport scheme for ice and snow thickness advection. SISIM also manages the interaction between sea ice and ocean currents, ensuring realistic drift and deformation of sea ice (Semtner Jr, 1976; Hunke and Dukowicz, 1997).

### 3.1.4 Land Surface Model (PALADYN)

The land surface model PALADYN in CLIMBER-X serves as an interface for energy and water exchanges between the surface and the atmosphere while representing vegetation dynamics and land carbon cycle processes. PALADYN includes explicit

treatment of permafrost and differentiates between eight surface types, including various plant functional types, bare soil, land ice, and lakes. The model employs a consistent approach to simulate soil temperature, water content, and carbon processes across five soil layers. Additionally, PALADYN includes modules for snow albedo, dust emissions, and the effects of land use changes. The model's hydrological cycle covers interception, runoff, and infiltration, ensuring a comprehensive representation of terrestrial processes. Recent enhancements include parameterizations for snow grain size and dust and soot effects on snow albedo, based on regional climate model outputs and empirical data (Willeit and Ganopolski, 2016; Dang et al., 2015).

## 3.2 PDAF

PDAF provides a computationally efficient framework for performing ensemble-based DA with different filters in numerical models (http://pdaf.awi.de; Nerger and Hiller, 2013). It separates the data assimilation system into three parts: numerical model, observations, and filter algorithms. The filter algorithms combine the model and observational information.

PDAF can be efficiently coupled with numerical models, allowing us to have a model with data assimilation extension (Figure 3.2). The high efficiency and full parallelization features of PDAF make it a proper tool for different ensemble sizes for data assimilation in climate models (Nerger et al., 2020). Different types of EnKF filter algorithms, PF, and variational methods for DA are available in PDAF.

## 3.3 DA Algorithm

In this study, the Local Error Subspace Transform Kalman Filter (LESTKF) is chosen as the DA algorithm because it is a particularly efficient formulation for high-dimensional DA (Nerger et al., 2012).

The LESTKF is a localized version of the Error Subspace Transform Kalman Filter (ESTKF; Nerger et al., 2012). The ESTKF uses an ensemble of $m$ model states of size $n$, which are stored as columns of the matrix $\mathbf{X}_k$. The prior climate states

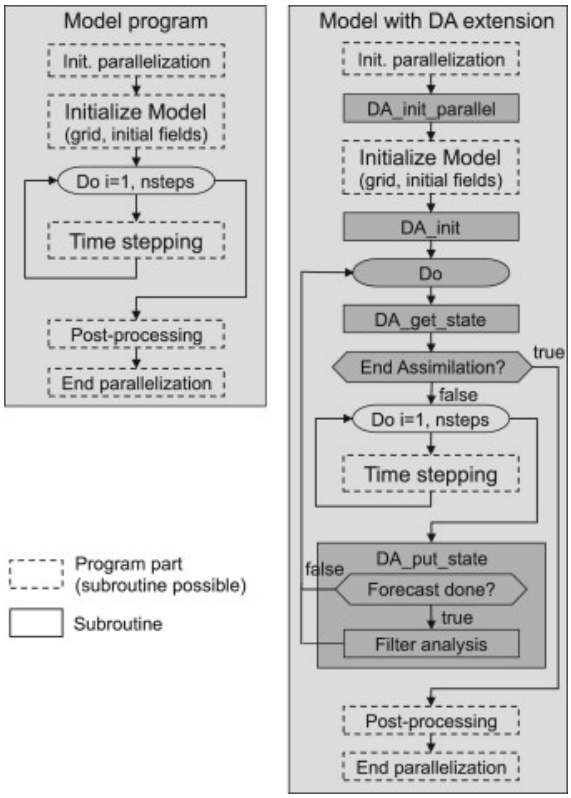


Figure 3.2: Left: Flow diagram of a typical numerical model. Right: The flow diagram of the model extended to an assimilation system by calls to routines of the assimilation framework. Figure has been taken from Nerger and Hiller (2013).

matrix $\mathbf{X}_k^{prior}$ from the model simulations is converted into a matrix of analysis states $\mathbf{X}_k^a$ at time $t_k$ using the transformation

$$\mathbf{X}_k^a = \bar{\mathbf{x}}_k^{prior}\mathbf{1}_m^T + \mathbf{X}_k^{prior}\left(\mathbf{w}_k\mathbf{1}_m^T + \tilde{\mathbf{W}}_k\right). \tag{3.1}$$

Here, $\bar{\mathbf{x}}_k^{prior}$ presents the prior ensemble mean state of size $n$, and $\mathbf{1}_m$ is a vector of size $m$ having the value of one in all elements. Additionally, $\mathbf{w}_k$ is a vector size of $m$ transforming the ensemble mean, and the ensemble perturbation is transformed by the matrix $\tilde{\mathbf{W}}_k$ of size $m \times m$ named weight matrix. Since all computations in the analysis refer to the time $t_k$, the time index $k$ is skipped hereafter.

The ensemble transformation matrix and vector are calculated in an error subspace of dimension $m-1$ represented by the prior ensemble. An error-subspace matrix can be computed by $\mathbf{L} = \mathbf{X}^{prior}\mathbf{T}$, where the matrix $\mathbf{T}$, named projection matrix, has the size of $m \times m-1$ and is defined by

$$\mathbf{T}_{ji} = \begin{cases} 1 - \frac{1}{m}\frac{1}{\frac{1}{\sqrt{m}}+1} & \text{for } i = j, j < m \\ -\frac{1}{m}\frac{1}{\frac{1}{\sqrt{m}}+1} & \text{for } i \neq j, j < m \\ -\frac{1}{\sqrt{m}} & \text{for } j = m. \end{cases} \tag{3.2}$$

The relation between the prior state vector $\mathbf{x}^{prior}$ and the vector of observations $\mathbf{y}$ is described as

$$\mathbf{y} = \mathbf{H}(\mathbf{x}^{prior}) + \epsilon, \tag{3.3}$$

where $\mathbf{H}$ is the observation operator, and $\epsilon$ gives the vector of observation errors, which is considered a white Gaussian distributed random process with observation error covariance matrix $\mathbf{R}$. For the analysis step, a transform matrix, which has size $(m-1) \times (m-1)$, is calculated as

$$\mathbf{A}^{-1} = \rho(m-1)\mathbf{I} + (\mathbf{H}\mathbf{X}^{prior}\mathbf{T})^T\mathbf{R}^{-1}\mathbf{H}\mathbf{X}^{prior}\mathbf{T}. \tag{3.4}$$

Here, the $\mathbf{I}$ is the identity matrix, and $\rho$ is named the "forgetting factor" (Pham et al., 1998). $\rho$ with the value of $0 < \rho \leq 1$ is used to inflate the prior error covariance matrix. The weight vector $\mathbf{w}$ and matrix $\tilde{\mathbf{W}}$ are now defined by

$$\mathbf{w} = \mathbf{T}\mathbf{A}(\mathbf{H}\mathbf{X}^{prior}\mathbf{T})^T\mathbf{R}^{-1}(\mathbf{y} - \mathbf{H}\bar{\mathbf{x}}^{prior}), \tag{3.5}$$

$$\tilde{\mathbf{W}} = \sqrt{m-1}\mathbf{T}\mathbf{A}^{1/2}\mathbf{T}^T, \tag{3.6}$$

where $\mathbf{A}^{1/2}$ is the symmetric square root of $\mathbf{A} = \mathbf{U}\mathbf{S}^{-1}\mathbf{U}^T$ that is calculated from the eigenvalue decomposition $\mathbf{U}\mathbf{S}\mathbf{V} = \mathbf{A}^{-1}$ such that $\mathbf{A}^{1/2} = \mathbf{U}\mathbf{S}^{-1/2}\mathbf{U}^T$.

For localization, which is required for a high-dimensional model, each individual grid point is independently updated by a local analysis step that considers only observations within a horizontal radius of influence $l$. Thus, a local observation operator computes an observation vector within the radius $l$ from the global model state. Furthermore, each observation is weighted according to its distance from the grid point. The weight is applied by multiplying the entries of matrix $\mathbf{R}^{-1}$ in the Eqs (3.4) and (3.5) by a weight which decreases from one to zero with increasing distance. The localization weight is computed by a fifth-order polynomial with a form similar to a Gaussian function (Gaspari and Cohn, 1999). In localization, Eq (3.1) is used with individual matrices $\mathbf{w}_k$ and $\tilde{\mathbf{W}}_k$ for each local analysis region.

# Chapter 4

# Transient Simulations of the Last Deglaciation

Several studies highlight different facets of glacial-interglacial climate, including the last deglaciation, by employing model simulations with prescribed ice sheet changes (e.g., Knorr and Lohmann, 2007; Liu et al., 2009; He, 2011; Zhang et al., 2014, 2017; Sun et al., 2022) or more complicated simulations done by coupled ice sheet-climate modeling (e.g., Ganopolski and Calov, 2011; Abe-Ouchi et al., 2013; Gregoire et al., 2015). Ganopolski and Calov (2011) and Abe-Ouchi et al. (2013) emphasize that orbital changes primarily drive glacial-interglacial cycles. Zhang et al. (2021) show that an abrupt transition from warm interstadial to cold stadial states could be initiated directly by precession and obliquity changes. Gregoire et al. (2015) suggest that orbital forcing is the main driver of the reduction of North American ice sheets, while GHG forcing accounts for 30% contribution as the second driver. GHG, particularly $CO_2$, are essential for the amplitude of the cycles and result in complete deglaciation (Charbit et al., 2005; Ganopolski and Calov, 2011; Abe-Ouchi et al., 2013; Heinemann et al., 2014). Prescribing ICE-4G ice sheets (Peltier, 1994), Timmermann et al. (2009) indicate that orbital forcing and atmospheric $CO_2$ increase initiate the warming around Antarctica without direct triggers from the NH.

Previous studies show that a primary source of uncertainty in the glacial-interglacial simulations is the ice sheet evolution, which has a decisive influence on the timing

and occurrence of climate events (e.g., Ullman et al., 2014; Zhang et al., 2014; Bakker et al., 2020; Kapsch et al., 2022). Ice sheet heights are important for simulating the atmospheric (Kageyama and Valdes, 2000; Löfverström et al., 2014) and oceanic circulation (Zhang et al., 2014; Zhu et al., 2014; Sherriff-Tadano et al., 2018). Kapsch et al. (2022) and Bouttes et al. (2023) follow PMIP4 (e.g., Kageyama et al., 2017) for transient simulation of the last deglaciation (Ivanovic et al., 2016), and compare the effect of the ICE-6G (Argus et al., 2014; Peltier et al., 2015) and GLAC1D (Tarasov et al., 2012; Briggs et al., 2014) ice sheet reconstructions. Consistent with the control of the ocean circulation by ice sheet height (Zhang et al., 2014), Kapsch et al. (2022) indicate that topography differences lead to changes in the jet stream's magnitude, the atmospheric circulation, and river directions in the last deglaciation. Bouttes et al. (2023) employ an EMIC and show that changes in bathymetry lead to a cooling in the deglaciation simulations. In addition, the use of evolving ice sheets implies changes in freshwater flux into the ocean, affecting AMOC (McManus et al., 2004; Stouffer et al., 2007; Kageyama et al., 2010). The deglacial AMOC strongly depends on the timing and magnitude of freshwater forcing at high latitudes of the North Atlantic or Arctic, where deep water forms (e.g., Stouffer et al., 2006; Smith and Gregory, 2009; Roche et al., 2010; Lohmann et al., 2020). When the freshwater shifts over a critical value, called bifurcation point (Held and Kleinen, 2004), the AMOC can shift or fluctuate between modes (e.g., Lohmann and Schneider, 1999; Zhang et al., 2017; Klockmann et al., 2018; Kapsch et al., 2022; Sun et al., 2022). Accordingly, AMOC instability can lead to abrupt climate changes during the last deglaciation (e.g., Lohmann and Schulz, 2000; Clark et al., 2002; Knorr and Lohmann, 2007). Bethke et al. (2012) conduct sensitivity simulations with the ICE-5G (Peltier, 2004) reconstruction and investigate different combinations of GHG, orbital, and ice sheet forcing. They suggest that ice sheet reconstructions provide limited constraints on the timing, volume, and location of the freshwater discharges associated with melting ice sheets.

This chapter conducts several simulations of the last deglaciation with different forcings to understand the role of ice sheets, GHGs, and orbital forcings for the past 22 ka BP.

## 4.1 Choice of ice sheet reconstruction

PaleoMist and GLAC1D use different methodologies to reconstruct the past ice sheets. GLAC1D creates the Greenland Ice Sheet based on an ice sheet modeling exercise that was tuned to fit Holocene sea level observations (Tarasov and Richard Peltier, 2002). Antarctica and North American ice sheets are based on an ensemble average of several thousand ice sheet model simulations that scored favorably in fitting constraints such as Holocene sea level changes and present-day uplift rates (Tarasov et al., 2012; Briggs et al., 2014). Conversely, PaleoMist calculates the ice sheet using the ICESHEET program (Gowan et al., 2016), which assumes perfectly plastic, steady-state conditions for the ice sheet (i.e., the lateral shear stresses are ignored, and the ice surface is not dynamically changing). Employing the model SELEN (Spada and Stocchi, 2007), changes in sea level and Earth's deformation are computed using a time series of ice sheet changes. Finally, the sea level change is added to modern topography and the ice sheet thickness to produce a paleo-topography reconstruction (Gowan et al., 2021). Due to the above differences, the sea level increases linearly in PaleoMist while showing variation in GLAC1D, particularly during BA and YD (Figure 4.1).

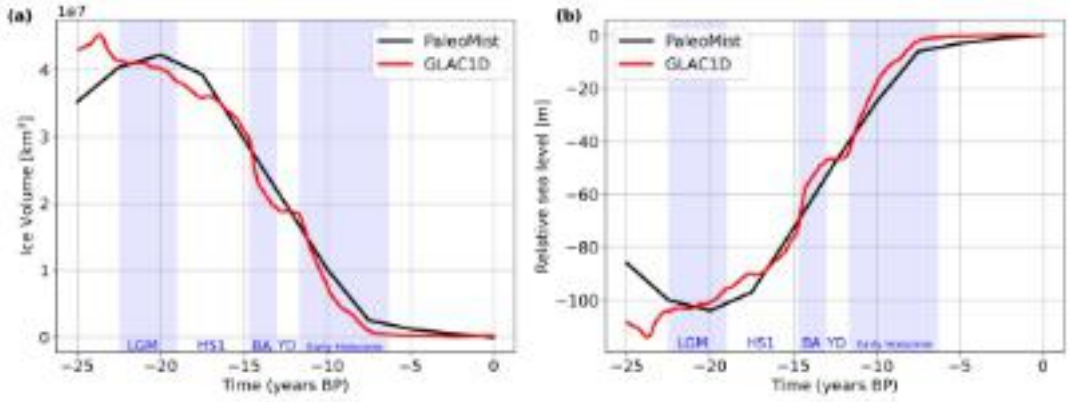


Figure 4.1: (a) Ice-volume evolution and (b) relative sea level to pre-industrial (PI) during the last deglaciation calculated by GLAC1D and PaleoMist.

Yokoyama et al. (2022) criticize that PaleoMist is based only on near-field constraints, resulting in discrepancy with previous studies (e.g., Clark and Tarasov, 2014) in the estimation of the relative sea level. To reply to Yokoyama et al. (2022), Gowan et al. (2022) reason that by relying on near-field constraints, Pa-

leoMist would be independent of deep-sea foraminifera and avoid sea-level proxies with high uncertainties. Moreover, Gowan et al. (2022) question in using spherically symmetric Earth structures to represent far-field sea level. Therefore, Gowan et al. (2021) utilize non-ice sheet proxies not as absolute constraints but to test PaleoMist qualitatively.

## 4.2 Experimental Design

Two sets of transient deglaciation simulations, Exp_GLAC1D and Exp_PaleoMist, are conducted, each consisting of five simulations: full-forced (GLAC1D_full and PaleoMist_full), with constant ice sheet reconstruction (GLAC1D_fixIce and PaleoMist_fixIce), with constant GHG (GLAC1D_fixGHG and PaleoMist_fixGHG), with constant orbital forcing (GLAC1D_fixOrbit and PaleoMist_fixOrbit), and PI simulation (GLAC1D_PI and PaleoMist_PI; Table A.1). In both experiments, GHG concentrations and orbital parameters are prescribed by Köhler et al. (2017) and Laskar et al. (2004), respectively. In addition, the GLAC1D reconstruction (Tarasov and Richard Peltier, 2002; Tarasov et al., 2012; Briggs et al., 2014) is used for ice sheets, bathymetry, and land-sea mask in Exp_GLAC1D, while Exp_PaleoMist employs the PaleoMist reconstruction (Gowan et al., 2021). Except for PI simulations, full-forced simulations are integrated from 25 kyr BP with PI equilibrium and then switch to LGM boundary conditions. The model is subsequently run until the year 6.5 kyr BP. Time-varying topography, bathymetry, GHGs ($CO_2$, $N_2O$, $CH_4$), and orbital parameters are prescribed in the full-forced simulations. The GHG and orbital parameters forcing field is updated yearly, while topography, bathymetry, and ice sheet distribution are changed every 100 years. In the model, the FW flux to the ocean is computed from a combination of precipitation-evaporation, sea ice fluxes, and land runoff. Additionally, the prescribed changes in ice thickness are converted into a liquid water flux that is routed into the ocean following the steepest surface gradient.

The sensitivity simulations begin with boundary conditions from 22 kyrs BP, and throughout the simulation, the corresponding forcing remains constant at the 22

kyrs BP level, while the other forcing factors vary over time. The LGM initial conditions recommended in the PMIP4 protocol (Kageyama et al., 2017) are prescribed. This means that in simulations with constant GHG forcing, $CO_2$, $N_2O$, and $CH_4$ were set to 190 ppm, 200 ppb, and 375 ppb, respectively. Similarly, eccentricity, obliquity, and perihelion are kept constant in simulations with constant orbital forcing at 0.018994, 22.949°, and 114.42°, respectively. This configuration is intentionally designed to determine the distinct role of individual forcing factors. Finally, PI is defined as the year 1850, and PMIP4 instructions are followed for applying GHG and orbital forcings in the PI simulations.

## 4.3 Sensitivity simulations

In Figure 4.2, the left panels show the deglacial dynamics for Exp_GLAC1D, whereas the right panels are for Exp_PaleoMist. Sensitivity forcing experiments are performed, maintaining different deglacial forcing components at LGM levels. In scenarios with fixed ice sheets and bathymetry (blue lines in Figure 4.2), North Atlantic FW forcing (≥30° N, including FW in the Arctic Ocean) remains near LGM levels. Consequently, North Atlantic sea surface salinity (SSS) and AMOC show minor changes. However, in Exp_GLAC1D, FW forcing slightly exceeds Exp_PaleoMist on average by approximately 0.05 Sv, resulting in a weaker early Holocene AMOC. GLAC1D_fixIce and PaleoMist_fixIce simulations underestimate last deglaciation warming, yielding an early Holocene GMST approximately 2.5 °C warmer than LGM. This result aligns with the anticipated consequences of constant FW forcing and albedo effects, corroborating findings by Zhang et al. (2014), indicating that slight changes in NH ice sheet height can initiate immediate climate shifts.

In simulations with constant GHG forcing (red lines in Figure 4.2), FW forcing is higher than in full-forced simulations due to more precipitation occurring in the fixGHG simulations (see Figures A.2, A.3, and A.4 in Appendix A). This is notable in Exp_PaleoMist during YD and early Holocene (Figure 4.2b). When FW exceeds approximately 0.24 Sv during the simulations, AMOC transitions to off-mode. This

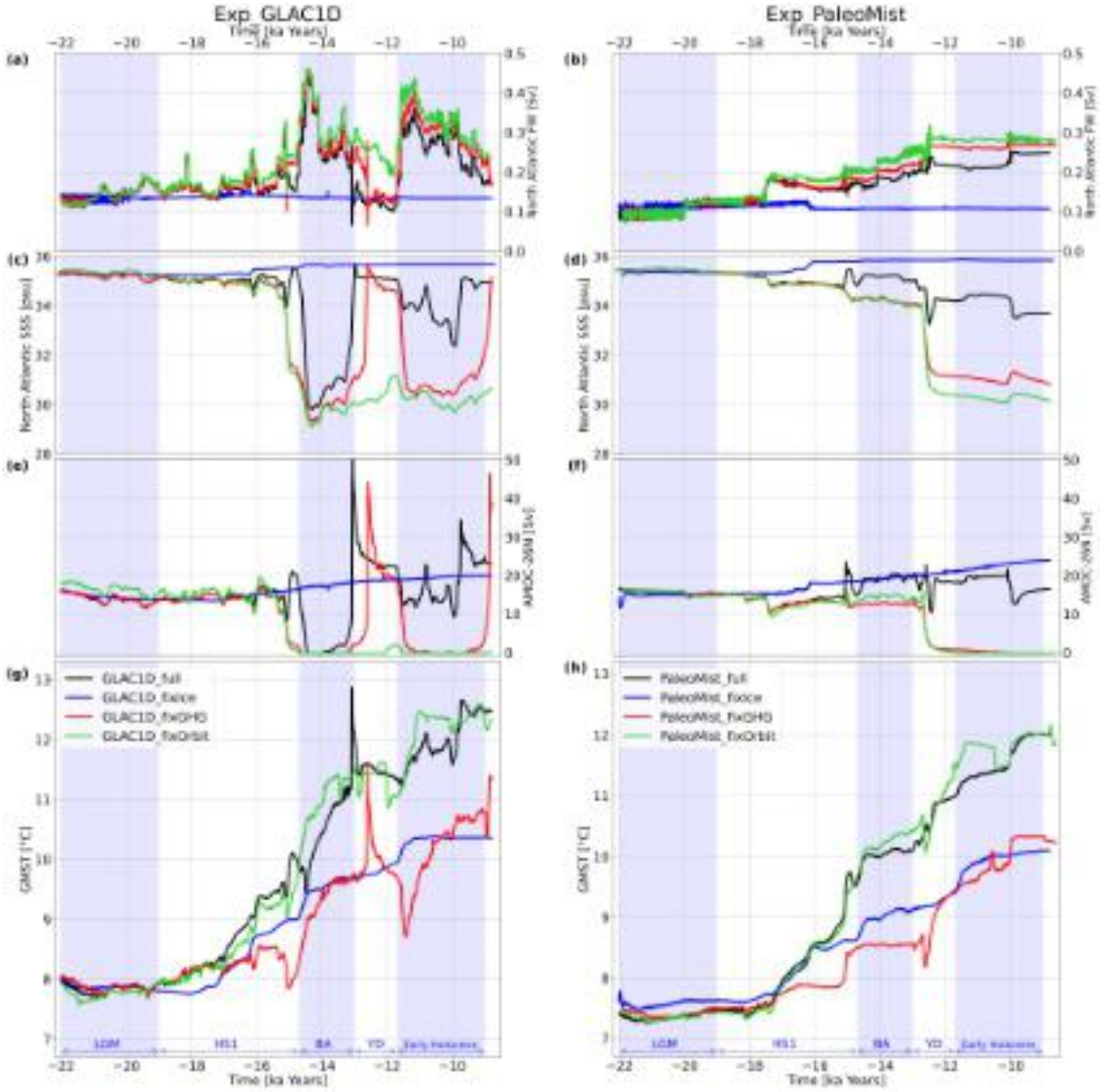


Figure 4.2: North Atlantic FW, North Atlantic SSS, AMOC at 26°N, and GMST for Exp_GLAC1D (a),(c),(e),(g), and for Exp_PaleoMist (b),(d),(f), and (h). LGM is defined as 22-19 kyr BP, Heinrich Stadial 1 (HS1) as 19-14.7 kyr BP, BA as 14.7-13 kyr BP, and YD as 13-11.6 kyr BP. North Atlantic index for SSS is defined as an average over 50°N-70°N and 45°W-0°W. The blue background represents LGM, BA, and early Holocene, while the white background represents HS1 and YD. Note that the vertical axes differ for Exp_GLAC1D and Exp_Paleomist except for GMST panels (g and h). North Atlantic FW flux encompasses precipitation-evaporation, sea ice fluxes, land runoff, and liquid water flux melted from ice sheets.

transition aligns with HS1 culmination in Exp_GLAC1D (Figure 4.2e) and YD onset in Exp_PaleoMist (Figure 4.2f). This supports Zhang et al. (2017) results, suggesting atmospheric $CO_2$ changes critically impact AMOC transitions. Nonetheless, abrupt declines in FW within GLAC1D_fixGHG lead to sudden AMOC strengthening, subsequently resulting in a rapid increase in GMST. Furthermore, the GMST

increases only by approximately 3 °C during deglaciation in simulations featuring constant GHG forcing. This underscores the significant role played by transient GHG concentrations in driving the last deglaciation process.

There is a conspicuous FW forcing in GLAC1D_fixOrbit and PaleoMist_fixOrbit (green lines in Figure 4.2). Ice sheets' contribution to FW forcing remains unchanged across full-forced, constant GHG and orbital simulations. However, there are substantial variations in precipitation patterns, global mean precipitation, and evaporation between these simulations and the full-forced ones (see Figures A.2, A.3, and A.4 in Appendix A).

GLAC1D_fixOrbit and PaleoMist_fixOrbit depict higher precipitation in the NH, leading to increased FW in the North Atlantic. Furthermore, AMOC transitions to an off-mode state at comparable times (as shown in Figure. 4.2e and 4.2f) as in simulations with constant GHG forcing. This finding aligns with the outcomes of a study by Zhang et al. (2021), which demonstrated that precession and obliquity play influential roles in shaping hydroclimate in glacial-interglacial cycles. GHG and orbital forcings influence FW fluxes by changing precipitation patterns, with a sustaining effect on the AMOC. Moreover, the GLAC1D_fixOrbit and PaleoMist_fixOrbit simulations effectively replicate the increase of approximately 5 °C in GMST during the last deglaciation. This underscores the significant impact of GHG and ice sheets on the simulation of global temperatures during this period, although such forcing also affects the dynamics of AMOC.

## 4.4 Full-forced simulations: GLAC1D vs PaleoMist

In full-forced simulations (black lines in Figure 4.2), North Atlantic SSS (Figure 4.2c and d) is anti-correlated with North Atlantic FW forcing (Figure 4.2a and b) and reduced by about one psu during the simulations. This reduction is attributable to the FW contributions resulting from ice sheet melting (Broecker, 2002; Clark et al., 2012). North Atlantic SSS differs from 1 to 5 psu between GLAC1D_full and PaleoMist_full during various temporal segments (Figure 4.2c and d). GLAC1D_full is less saline over the Atlantic and more saline at the surface of the other oceans

(see Figure A.5 in Appendix A). During BA, due to the shutdown of AMOC in Exp_GLAC1D (Figure 4.2e), the northward transport of warm and saline water is disrupted, producing pronounced differences (exceeding 5 psu in North Atlantic) relative to Exp_PaleoMist (Figure 4.2c and d). During YD, GLAC1D_full simulates more saline surface water near Greenland, where deep water forms in the North Atlantic (Figure 4.2c and d). This phenomenon is potentially linked to the stronger AMOC in GLAC1D_full compared to PaleoMist_full (Figure 4.2e and f). PaleoMist presents a more extensive and higher ice sheet configuration than GLAC1D (see Figure A.6 in Appendix A). In the SH, PaleoMist_full shows more area covered by sea ice (sea ice fraction in grid cell $\geq$15%) during LGM ($\approx$20 mln $km^2$) and BA ($\approx$15.67 mln $km^2$) compared to GLAC1D_full ($\approx$19 and $\approx$8.79 mln $km^2$ for LGM and BA, respectively). In the NH, sea ice area during LGM in PaleoMist_full (10.30 mln $km^2$) exceeds that of GLAC1D_full (9.55 mln $km^2$). However, during BA, due to the weak AMOC, GLAC1D_full exhibits a greater sea ice area (12.73 mln $km^2$) than PaleoMist_full (9.85 mln $km^2$) over the NH (Figure 4.3).

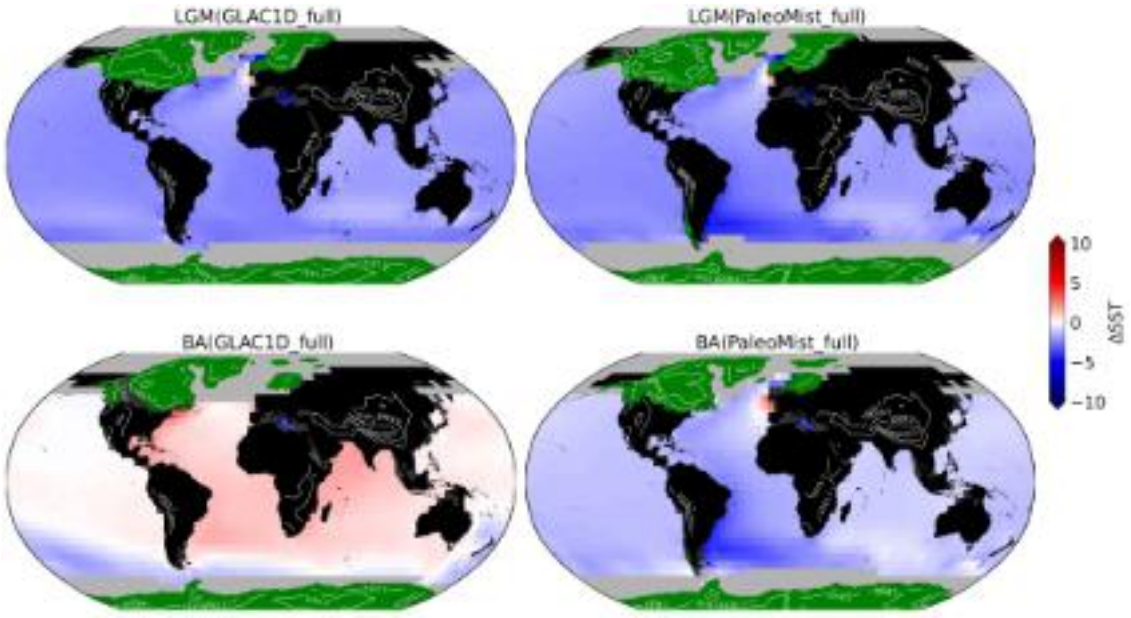


Figure 4.3: Ice sheet coverage (green area), sea ice (grey area), topography (contour lines), and SST anomaly relative to PI during LGM and BA for GLAC1D_full (left) and PaleoMist_full (right). The shown variables are averaged over the defined intervals. Note that the sea ice is plotted by the resolution of $5° \times 5°$ while the resolution of ice sheets and continents is $0.5° \times 0.5°$.

The glacial SST anomaly ($\Delta$SST) relative to PI period is almost identical over the

| Region | MARGO | GLAC1D_full | PaleoMist_full |
|---|---|---|---|
| Southern Ocean western Atlantic[1] | -2.5 ± 3.2 | -2.46 | -2.43 |
| Southern Ocean eastern Atlantic[2] | -1.9 ± 1.6 | -1.16 | -1.4 |
| Southern Ocean western Pacific[3] | -4.3 ± 1.4 | -1.4 | -1.83 |

Table 4.1: Comparison of MARGO, PaleoMist_full, and GLAC1D_full mean NH winter SST anomalies (LGM minus modern) for Southern Ocean key regions (°C). NH winter is defined as January-February-March.[1]defined as 30 to 60°S, 70 to 30°W, [2]defined as 30 to 60°S, 0 to 20°E,[3]defined as 30 to 60°S, 145°E to 150°W.

NH in GLAC1D_full and PaleoMist_full (Figure 4.3). The global ΔSST during LGM (average over 22-19 kyr BP) is -2.18 and -2.15 °C for GLAC1D_full and PaleoMist_full, respectively. These results are around 1 °C warmer than cooling 3.14 ± 0.29 °C reconstructed by Tierney et al. (2020b). During the NH winter, PaleoMist_full and GLAC1D_full are consistent with MARGO (MARGO, 2009) over the Southern Ocean western Atlantic. In the Southern Ocean eastern Atlantic, PaleoMist_full shows more cooling than GLAC1D_full and aligns better with MARGO. However, in the Southern Ocean western Pacific, MARGO indicates colder temperatures than simulations done in this chapter (Table 4.1).

The simulated global cooling during the LGM (average over interval 22-19 kyr BP), relative to PI, amounts to 6.12 °C in PaleoMist_full and 5.9 °C in GLAC1D_full. These results are in agreement with data assimilation-based estimate of 6.05±0.43 °C by Tierney et al. (2020b), the data assimilation-based estimate of 6.75 ±0.48 °C by Osman et al. (2021), and the model-based estimate of 6.2 °C in Willeit et al. (2022). However, Annan et al. (2022) reconstructed a smaller GMST anomaly (LGM-PI) of 4.5±0.9 °C. PaleoMist_full depicts a colder LGM GMST (by approximately 0.5 °C) than GLAC1D_full due to higher ice sheet altitudes. This 0.5 °C difference is more than the difference between the 6.12 and 5.9 °C anomalies because of the difference in GLAC1D_PI and PaleoMist_PI temperatures.

During BA, GLAC1D_full oceans are warmer than PI in most regions (Figure 4.3) due to an abrupt AMOC shift (Figure 4.2e), leading to an abrupt increased temperature at the end of BA. The main differences between full forced simulations occur during BA due to significant FW flux differences (see Figure A.7) and very different AMOC (Figure 4.2e and f). GLAC1D includes significant ice volume loss during BA in the North Atlantic, associated with the major meltwater pulse 1A (MWP-1A)

(Peltier, 2005), resulting in substantial FW influx (Figure 4.2a). GLAC1D loses $0.225\times10^7 km^3$ ice more than PaleoMist during BA. This configuration imparts a diminished AMOC in GLAC1D_full (Figure 4.2e), correspondingly inducing lower SSS in the North Atlantic relative to PaleoMist_full.

The AMOC alterations are often proposed as a main factor in abrupt climate shifts during the last deglaciation (e.g., Lohmann and Schulz, 2000; Clark et al., 2002; Knorr and Lohmann, 2007). AMOC strengthening during the BA compared to HS1 is observed in reconstructions (McManus et al., 2004; Ng et al., 2018) and modeling studies (e.g., Liu et al., 2009). In GLAC1D_full, AMOC increases at the end of HS1 but experiences an off-mode transition at the onset of the BA period, followed by a substantial resurgence at the end of the BA (Figure 4.2e). The sudden reduction in AMOC during BA is common in the transient simulations prescribing GLAC1D (e.g., Broecker, 2002; Clark et al., 2012; Figure 4.4). In PaleoMist_full, AMOC has an abrupt increase and reduction at the end of HS1. It increases considerably at the onset of BA and is almost stable by the end of BA (Figure 4.2f). In both simulations, the abrupt strengthening of AMOC occurs before BA. As shown in Figure 4.2 for different simulations, the timing of the abrupt changes in the AMOC depends on the FW flux. Obase and Abe-Ouchi (2019) suggested that the gradual increase in atmospheric $CO_2$ during HS1 may cause a weakening of stratification of the North Atlantic, which results in an abrupt rise in the AMOC during the BA transition. Converse to BA, McManus et al. (2004) indicated AMOC was weak during YD. In GLAC1D_full, AMOC after the overshoot decreases gradually during YD, while in PaleoMist_full, it experiences variations and an abrupt reduction (Figure 4.2e and f).

When comparing the evolution of North Atlantic SST in the simulations with a corresponding marine climate record (Waelbroeck et al., 2001), PaleoMist_full simulation reflects the warming and cooling patterns over the North Atlantic during BA and YD periods. In contrast, the GLAC1D_full simulation suggests cooling during the BA, followed by a sudden increase and decrease, and relatively stable temperature during YD (Figure 4.5a-c).

For the BA/YD sequence in GMST, the Shakun and Osman reconstructions show a

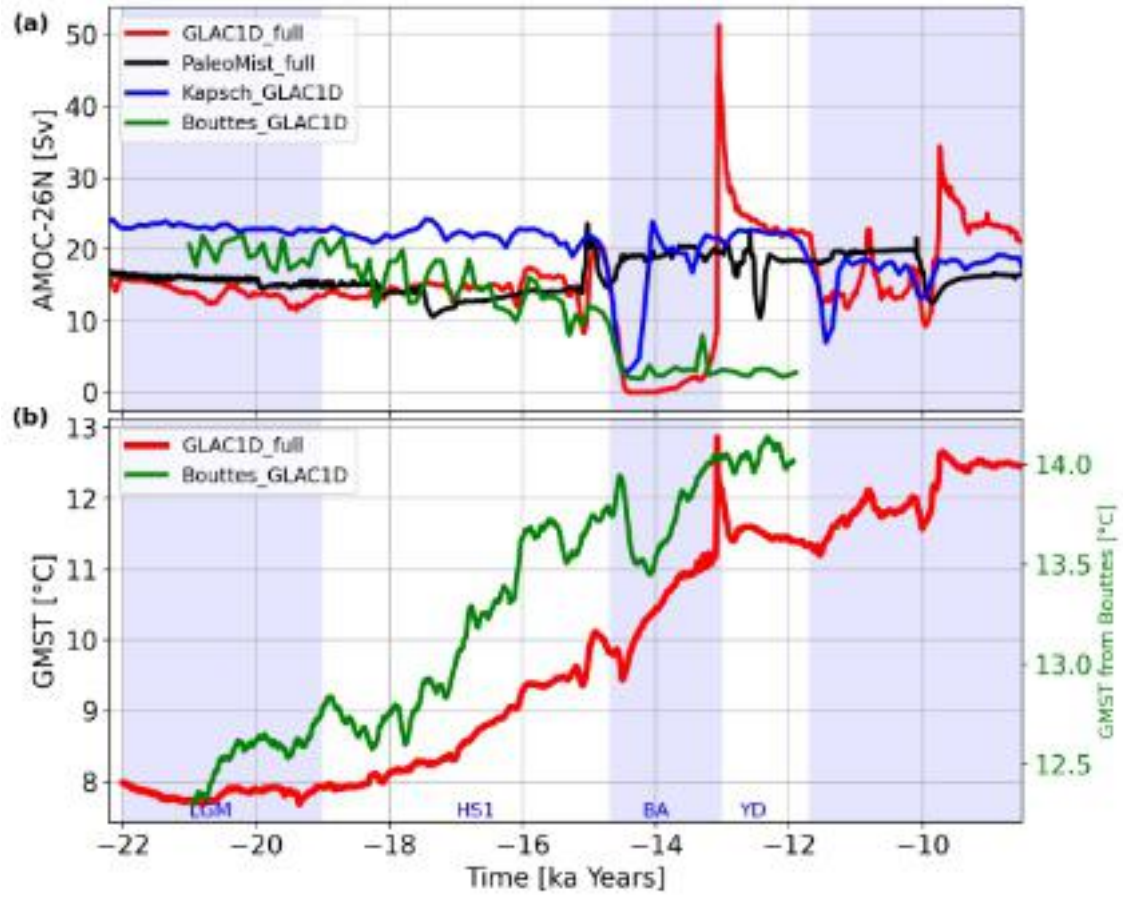


Figure 4.4: (a) Comparision of AMOC at 26° N between GLAC1D_full, PaleoMist_full and transient simulations conducted by Bouttes et al. (2023) and Kapsch et al. (2022). (b) GMST for GLAC1D_full and Bouttes et al. (2023). Note that there are different Y-axis for GLAC1D_full and Bouttes et al. (2023) in (b).

"warming-cooling-warming" sequence in global mean surface temperature (GMST; Figure 4.5d). In GLAC1D_full, the transition from BA to YD is also seen, following the AMOC pattern (Figure 4.2e and g). If the abrupt reduction and overshoot during BA are ignored, GLAC1D_full shows a "warming-cooling-warming" sequence, but this sequence is late with respect to the reconstructions (Figure 4.5d). Moreover, the warming of the BA in GLAC1D_full matches neither NGRIP nor DomeC temperature records (Figure 4.5a and b). Comparing Bouttes_GLAC1D and GLAC1D_full, AMOC shifts to the weak mode simultaneously at the onset of BA in both simulations. Still, the timing and magnitude of overshoot of AMOC at the onset of YD is mostly a model-dependent feature, and consequently, the GMST trajectory is different in GLAC1D_full (Figure c4.4).

Conversely, GMST within the PaleoMist_full scenario follows mainly GHGs (Fig-

ure 4.2h), with some shorter variations ($\approx 0.25$ °C) at the onset of the BA (warming-cooling-warming) occurred much earlier than reconstructions (Figure 4.5d). Moreover, there is a minor short-term cooling ($\approx 0.1$ °C) during the YD, which is not comparable with the reconstruction cooling. Generally, a "warming-stable-warming" sequence from -15 to -12.5 kyr BP is observed in PaleoMist_full for GMST and temperatures in DomeC and NGRIP locations (Figure 4.5b and d).

Figure 4.6d-g indicates surface temperature anomalies between the BA and HS1 and between YD and BA for both PaleoMist_full and GLAC1D_full. PaleoMist_full shows a pronounced warming between the BA and HS1 and a moderate cooling between YD and BA in the northern North Atlantic. The opposite is found for GLAC1D_full with cooling between the BA and HS1 and warming between YD and BA. The deglacial meltwater and its influence on AMOC affect the timing of the two-step character "cold-warm-cold-warm" during the termination: For PaleoMist_full, the HS1-stadial comes along with a weaker AMOC and a stronger AMOC during BA (Figure 4.6a and b), in contrast to GLAC1D_full. The PaleoMist simulations replicate, at least qualitatively, the BA/YD sequence with respect to reconstructions: a warming in Greenland and Antarctica in the BA, a cooling northern North Atlantic, and a warming in Antarctica in the YD.

Finally, surface temperature field differences between PaleoMist_full and GLAC1D_full (Figure 4.7) indicate a colder NH during HS1 and YD and warmer conditions in PaleoMist_full relative to GLAC1D_full. Temperature variations exceeding 10 °C highlight ice sheet reconstruction's pivotal role in modeling regional climate states, where greater elevation corresponds to lower temperatures. This pattern is evident during LGM, HS1, YD, and BA in North America. Ice-sheet extent and topography can influence local temperature gradients and the flow of air masses, alter pressure gradients, and affect wind patterns (Figures A.8, A.9, and A.10 in Appendix A). Furthermore, the temperature fields align with surface albedo patterns (Figure A.11 in Appendix A), such as during BA, where off-mode AMOC in GLAC1D_full fosters increased sea ice and higher albedo within the North Atlantic region, resulting in a substantial temperature anomaly of -10 °C relative to PaleoMist_full conditions.

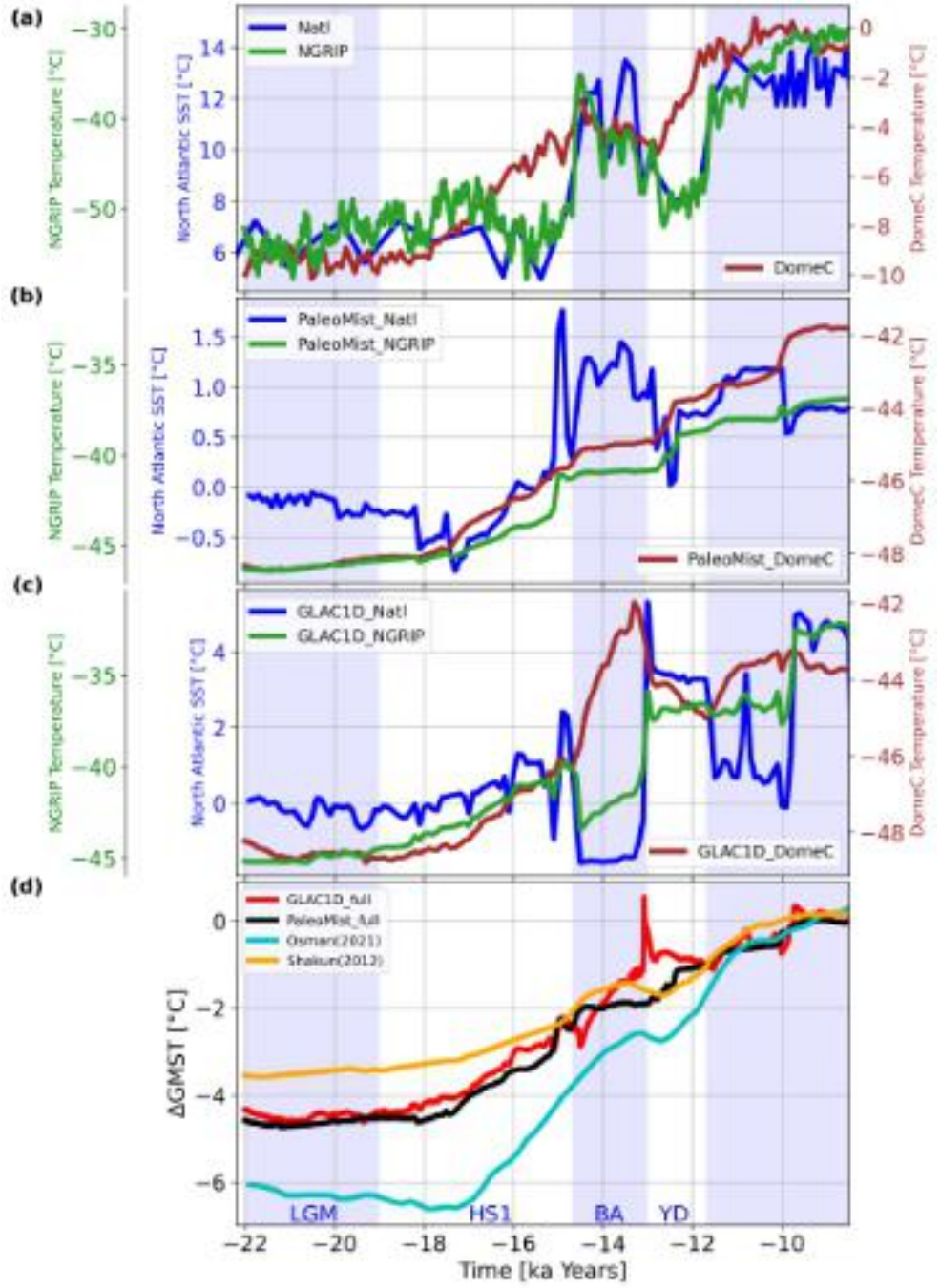


Figure 4.5: (a) Evolution of temperature at NGRIP (Greenland), DomeC (Antarctica), and SST at North Atlantic (NA87-22; Waelbroeck et al., 2001), (b) Evolution of temperature at NGRIP, DomeC, and SST at North Atlantic in PaleoMist_full, (c) Evolution of temperature at NGRIP, DomeC, and SST at North Atlantic in GLAC1D_full, and (d) GMST anomaly from the early Holocene (defined as 11.5-6.5 kyr BP) for GLAC1D_full, PaleoMist_full, Shakun et al. (2012), and Osman et al. (2021). Data for NGRIP, DomeC, and NA87-22 in (a) are from Shakun et al. (2012). North Atlantic index for SST in (b) and (c) is defined as an average over 50°N-70°N and 45°W-0°W. Discrepancies between Shakun et al. (2012) and Osman et al. (2021) reconstructions are due to utilizing different observation datasets, background states, and methods. Note that there are different vertical axes for different variables.

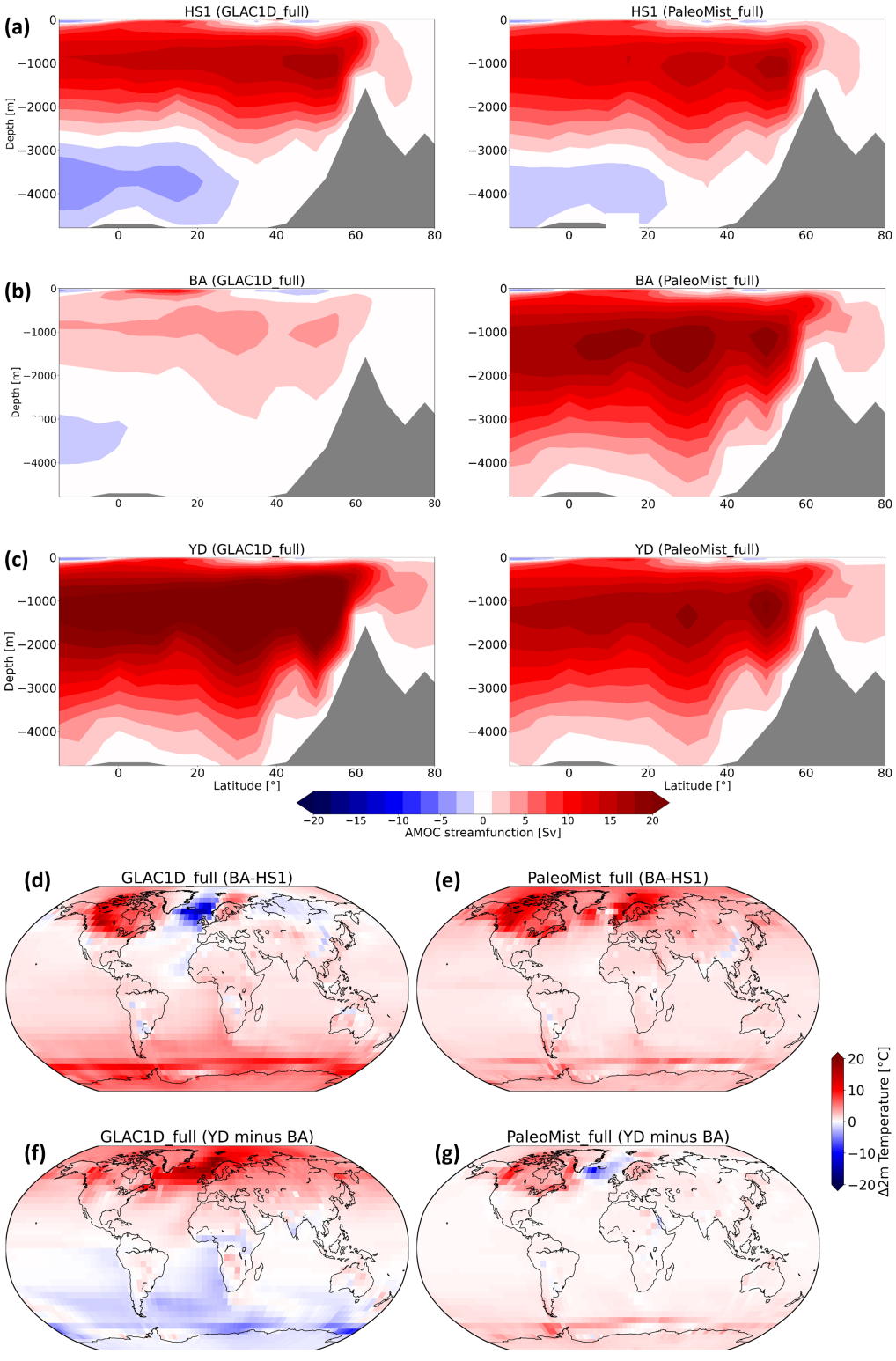


Figure 4.6: AMOC stream function for GLAC1D_full and PaleoMist_full during HS1, BA, and YD (a),(c), and (e). Near-surface temperature (2m temperature) anomalies between BA and HS1 and between YD and BA for PaleoMist_full (d) and (f) and GLAC1d_full (e)and (g), indicating the differences in the regional temperature signatures. The shown variables are averaged over the defined intervals.

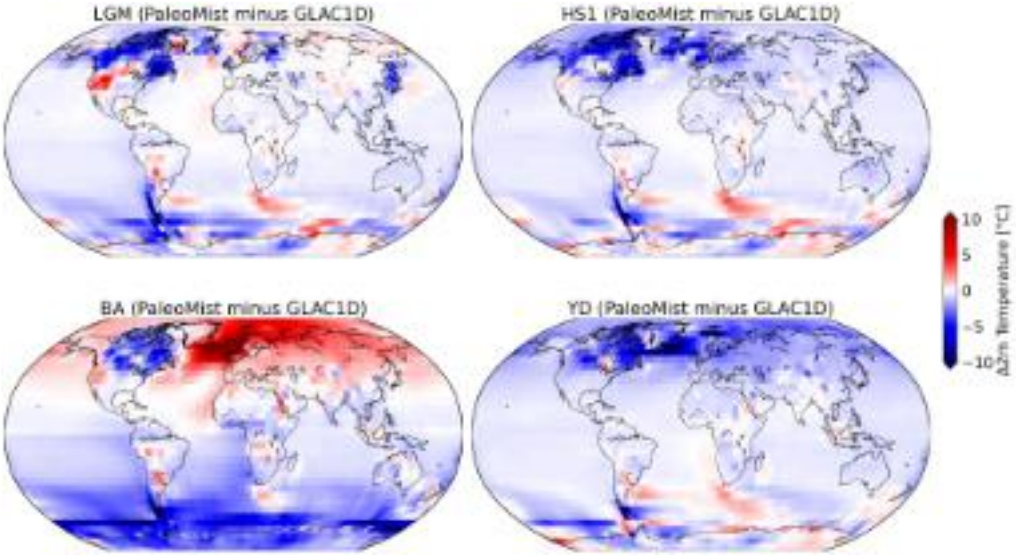


Figure 4.7: Surface temperature (2m temperature) differences between GLAC1D_full and PaleoMist_full for LGM, HS1, BA, and YD.

# Chapter 5

# Paleoclimate Data Assimilation: An ensemble Kalman filter for the Last Deglaciation

To address the second objective of this dissertation, this chapter presents an online DA technique for implementation over the last deglaciation using CLIMBER-X (Section 3.1) and LESTKF (Section 3.3). At the time of this study, only Osman et al. (2021) have used DA for the reconstruction of the past 24,000 years. Their method employs an offline ensemble square root Kalman filter (Tierney et al., 2020b), which combines prior climate states derived from the iCESM (Hurrell et al., 2013) model simulations with proxy observation data. This approach produces a posterior ensemble of climate states that better reflects past climatic conditions. Osman et al. (2021) aimed to address the Holocene temperature conundrum (Liu et al., 2014) and demonstrated that temperature variability over the last deglaciation was primarily influenced by two key climatic mechanisms: radiative forcing from ice sheets and GHGs, and changes in ocean overturning circulation combined with seasonal insolation.

## 5.1 Observations

The dataset provided by Shakun et al. (2012) is used as observations in the data assimilation system. The dataset includes well-dated temperature records from the last glacial period, including sixty-seven records from the ocean, interpreted as SST, and thirteen records for temperatures at the land surface. The dataset contains the absolute temperature values of each proxy site (green dots in Figure 5.2), the published age, and the corresponding errors of the age model ($\sigma$).

For the reconstruction of the early Holocene global mean surface temperature (GMST) anomaly (11.5-6.5 kyr BP; $\Delta$GMST), Shakun et al. (2012) first project the dataset onto a $5° \times 5°$ grid, then linearly interpolate it to a 100-year resolution and integrate it as area-weighted averages. The details of the age control, proxy temperatures, and uncertainty analysis are explained in Shakun et al. (2012). As the spatial resolution of this reconstruction corresponds to that of CLIMBER-X, a comparison of the simulated trajectory with Shakun et al.'s reconstruction can be made with ease.

Since the dataset does not contain the surface temperature errors for the proxy sites, the age model uncertainties are translated into temperature uncertainties. To obtain the temperature uncertainty at time $t$ for each record, the corresponding temperature at $t - \sigma$ and $t + \sigma$ is subtracted from the temperature of $t$, and the absolute average of these variances is taken as the temperature uncertainty in $t$. Finally, the average temperature uncertainties over all records were taken to represent the vector of observational errors in the DA system for every 100 years.

## 5.2 Experimental Design

The combination of CLIMBER-X with PDAF can simultaneously run the transient simulation and DA without restarting the model. Two experiments are performed. Exp_GLAC1D uses GLAC1D (Tarasov et al., 2012) for the ice sheet reconstruction, bathymetry, and land-sea mask while a new ice sheet reconstruction, PaleoMist (Gowan et al., 2021), is employed in Exp_PaleoMist. In both experiments, GHGs (Figure A.1) and orbital forcing are taken from Köhler et al. (2017) and Laskar et al.

(2004), respectively. The transient simulations start at 25 kyr BP with PI equilibrium and then switch to LGM boundary conditions. The model is subsequently run until the year 6.5 kyr BP using prescribed time-varying topography, bathymetry, ocean, GHGs, and orbital forcing. Adequate equilibrium and representation of the climate states at 22 kyr BP are achieved after three thousand years.

In the DA setup, data are assimilated into the model every 100 years from 22 to 6.5 kyr BP, which means that the DA system consists of 156 cycles. An implicit assumption in a DA system for the optimal combination of model predictions and observations is that data and model errors are random with a mean of zero (i.e., unbiased), indicating the importance of identifying and correcting observational errors before implementing DA (Dee and Da Silva, 1998; Dee, 2005). In order to avoid systematic errors, the state vector containing the field updated by DA is initialized by yearly-averaged surface temperature anomalies from the early Holocene ($\Delta$ST) at the last year of 100-year intervals in which the observation information is available (Figure 5.1). The values of early Holocene are taken from the free run, and the prognostic variable, skin temperature, is used to calculate the yearly average surface temperature. Another advantage of assimilating anomalies is that the DA results can be easily compared with the GMST reconstruction of Shakun et al. (2012), which is presented as an anomaly from the early Holocene.

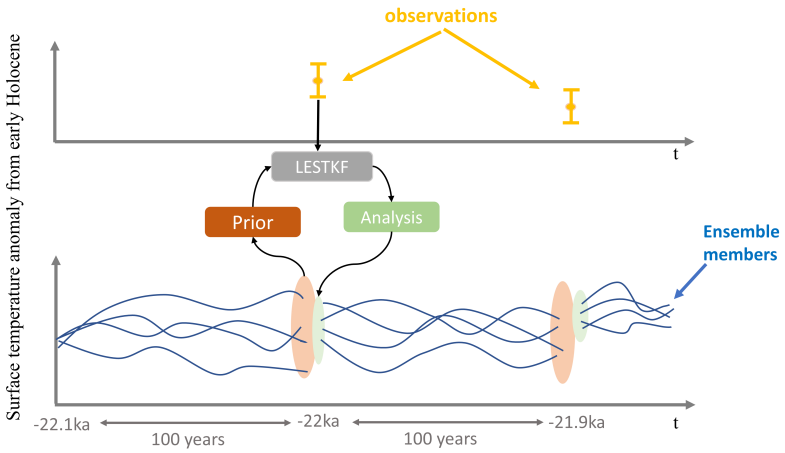


Figure 5.1: Schematic view of the DA system for the first two cycles.

In the DA system, the observation operator **H** in Eq (3.3) is a simple transformation matrix because the observation and the state vector have the same unit. This approach in paleoclimate DA is known as indirect DA (Li, 2014). Indeed, **H** extracts $\Delta$ST at the observed states and subtracts the mean to obtain the analysis states. Moreover, the DA system is online (Okazaki et al., 2021), estimating the time-averaged state and initial condition for subsequent DA cycles (Figure 5.1). Accordingly, an increment term is computed as $\mathbf{X}k^{a} - \mathbf{X}k^{prior}$ and added to the model field to calculate the state of the next time step. In other words, the model has an updated (or corrected) initial field for integration through the next 100 years until the next update for the initial condition.

Many studies demonstrate that the predictability of surface temperatures, typically captured by most proxies, extends beyond an annual timeframe (e.g., Collins, 2002; Doblas-Reyes et al., 2013). Consequently, in principle, online DA is expected to outperform offline DA when the model exhibits predictability that surpasses the averaging time represented by observations. This advantage arises from the ability of online DA, particularly in EnKF-based methods, to utilize more accurate initial conditions. To effectively leverage information from initial conditions with online DA, models must incorporate slowly changing components, such as the ocean model (Okazaki et al., 2021). Matsikaris et al. (2015) suggest when the computational cost of online and offline methods is comparable, the online approach is generally preferable due to the temporally consistent states it offers. Given that CLIMBER-X incorporates an ocean component and is characterized by its efficiency as a fast model, the online DA approach is opted for. Furthermore, the online DA provides the added benefit of enabling us to evaluate the performance of CLIMBER-X in simulating variables beyond surface temperature.

Here, the DA system has 16 ensemble members, and the localization radius is 5000 km. The size of the ensemble was chosen based on the computational cost. This choice is also consistent with Bhend et al. (2012), who have shown that an ensemble size of 15 or more is sufficient to constrain the simulations with the available proxy information.

Further, the optimal localization radius is determined by comparing experiments

with different radii. The localization radius is an important factor, usually tuned individually for each application in the DA methods applying localization. The previous studies based on the observation network, prior states, their DA methods, and the goal of their reconstruction define their criteria for the optimal radius. For example, Okazaki et al. (2021) employs an EMIC for their online DA experiments and uses a localization radius ranging from 2000 km to 8000 km. However, some other studies that conduct the offline DA select a relatively large radius localization such as 12000 and 25000 km (e.g., Tierney et al., 2020b; Osman et al., 2021; King et al., 2021; Erb et al., 2022). The key factor guiding the choice of radius is its impact on the surface temperature field. In Figure 5.2, the DA result of the surface temperature field after the first cycle of four DA experiments with radii of 2500, 5000, 7500, and 10000 km is compared. The data assimilation effect appears to be too localized for a radius of 2500 km. Using a radius of 5000 km, almost all grid points (99%) are influenced by at least one observation while avoiding large-distance covariances beyond this radius. For the 7500 and 10000 km radii, the DA combined information from locations that are too distant, which leads to reduced effect, e.g., over Greenland, but also spurious effects like the rather uniform cooling of the Antarctic.

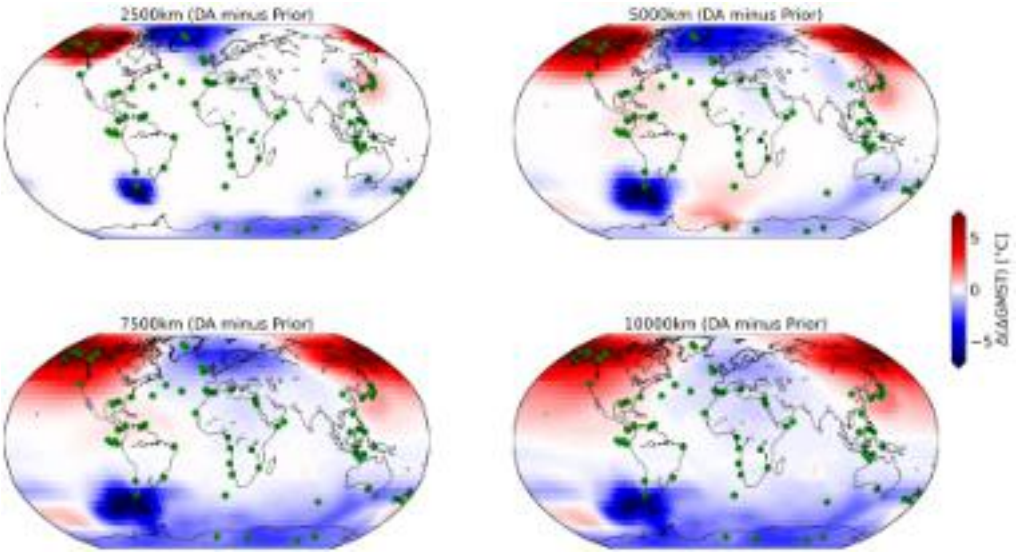


Figure 5.2: Effect of DA increment at first analysis step on the surface temperature field using 2500, 5000, 7500, and 10000 km radius.

## 5.3 Stochastic model component

In an ensemble-based DA system, the ensemble members represent the model uncertainty (Evensen, 2003). Since CLIMBER-X is a deterministic model (Palmer et al., 2010), ensemble members are integrated in parallel, with each ensemble member running on a single compute node equipped with 2×18-core CPUs on a high-performance computer (Cray CS400 Xeon E5-2697V4 3.60 GHz), and random perturbations are added to these model states at each model time step to obtain sufficient ensemble dispersion. The surface temperature values from a climate run in the TraCE-21000 project (He, 2011) are used to generate spatially-correlated perturbations as follows. First, the dataset is linearly interpolated to the spatial resolution of CLIMBER-X. Then, snapshots of the surface temperature values from 22 to 6.5 kyr BP every 100 years are collected in a matrix $\mathbf{Z}$ with 156 columns, each containing the anomaly values in the grid points at a given time. After subtracting the temporal mean, the matrix $\mathbf{Z}'$ is obtained. Then, the singular value decomposition $\mathbf{Z}' = \mathbf{VSW}$ is computed, yielding 155 empirical orthogonal functions (EOFs) stored in the columns of $\mathbf{V}$, while $\mathbf{S}$ is a diagonal matrix holding the corresponding singular values. Then, following second-order exact sampling (Pham, 2001), the matrix of ensemble perturbations is computed as

$$\mathbf{\Delta X} = \sqrt{\boldsymbol{m-1}}\mathbf{S}\mathbf{V}\mathbf{\Omega}^{\boldsymbol{T}}. \tag{5.1}$$

Here $m$ is the ensemble size, and $\Omega$ is a random matrix that preserves the mean and the covariances. Consequently, the ensemble perturbations are added to the ensemble members following the autoregressive method (Box et al., 2015) to make the model stochastic, providing an ensemble scatter. The perturbations are added to a prognostic variable named near-surface atmosphere temperature ($tam$) as

$$tam_k = tam_{k-1} + \varepsilon_k, \tag{5.2}$$

where $\varepsilon_k$ is perturbation at time $k$ defined as $(1-\alpha)\Delta x_{k-1} + \alpha \Delta x_k$. $\Delta x$, containing perturbations for the grid points, is one column of matrix $\Delta\mathbf{X}$. Therefore, $\Delta\mathbf{X}$ has 16 different columns that are used by ensemble members. $\alpha$ is a user-defined

coefficient, which is equal to 0.5 in the experiments. For the prior step, Figure 5.3 shows the ensemble spread for ΔGMST. This perturbation method yields that the standard deviation of the ensemble spread for both experiments varies between ≈ 0.2° and 0.4°C during the experiments.

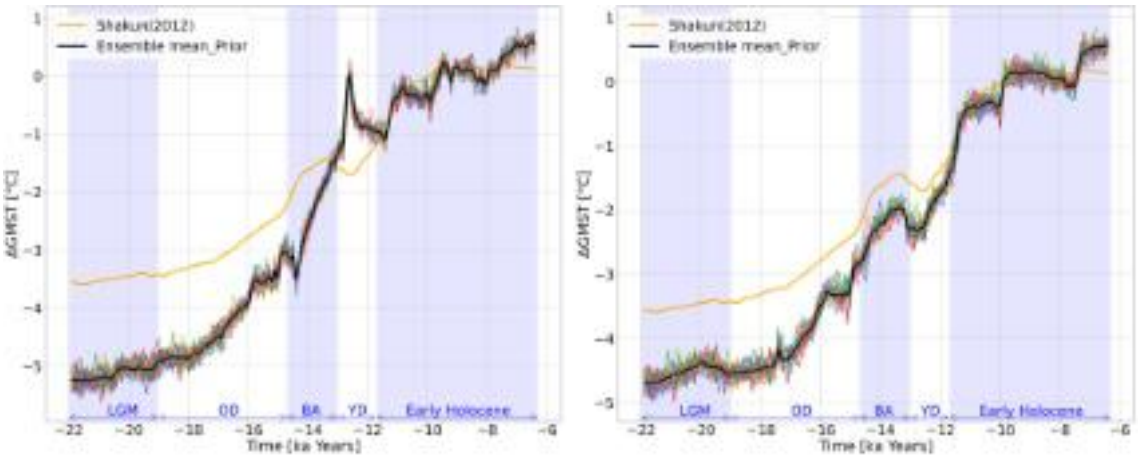


(a) (b)

Figure 5.3: Ensemble members (coloured lines) and ensemble mean compared to (Shakun et al., 2012) in the prior step in (a) Exp_GLAC1D and (b) Exp_PaleoMist.

## 5.4 Results

This section starts by comparing the outcomes of free model runs based on the GLAC1D and PaleoMist ice sheet reconstructions without DA. Thereafter, the effect of DA on ΔGMST trajectories is analyzed. Lastly, how the DA solution can alter the spatial patterns of the surface temperature fields is shown.

### 5.4.1 Free Runs

Figure 5.4a shows the absolute values of GMST for free runs with GLAC1D and PaleoMist. The different time intervals LGM, Oldest Dryas (OD), BA, YD, and early Holocene are used here as in Shakun et al. (2012). Both trajectories are nearly identical during the LGM. However, during the rest of the time, the PaleoMist simulation shows a cooler GMST, except for the beginning of the BA interval. Moreover, the GMST in the PaleoMist simulation increases more steadily, while in

the GLAC1D simulation, there are two abrupt shifts in the GMST at the beginning and end of the BA. The differences in the magnitude, timing, and speed of the warming and cooling trends during BA and YD are evident between the two free simulations, suggesting that ice sheet reconstruction significantly impacts the transient simulation.

Comparing the transient simulations with the GMST reconstruction of Shakun et al. (2012), which has been projected to a $5° \times 5°$ grid (Figure 5.4b), the $\Delta$GMSTs simulated by the model are about 1.3-1.5 times colder than the proxy-based reconstruction during the LGM. Shakun et al. (2012) and Exp_PaleoMist_Free show a continuous warming trend during BA, while this trend is disrupted in Exp_GLAC1D by a strong cooling followed by remarkably rapid warming. The trajectories of Shakun et al. (2012) and Exp_PaleoMist_Free behave similarly over the YD. In contrast, Exp_GLAC1D shows a strong decrease in $\Delta$GMST beginning with the onset of the YD.

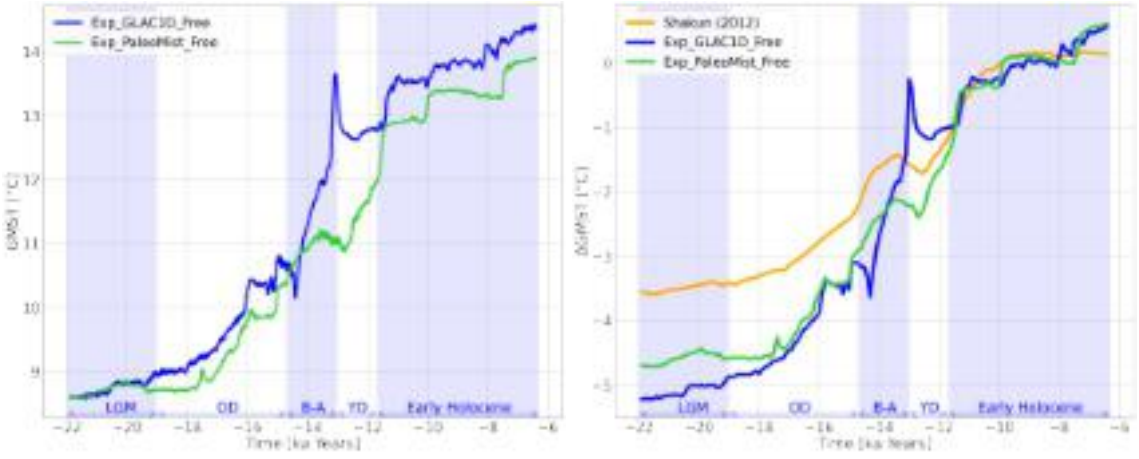


(a) (b)

Figure 5.4: a) GMST from free runs of the last deglaciation using the different ice sheet reconstructions, GLAC1D and PaleoMist. b) Comparison of GMST anomaly from the early Holocene of the free runs compared to Shakun et al. (2012).

### 5.4.2 Trajectories after DA

After applying the DA, the ensemble members are evaluated to ensure the DA system functions. The standard deviation of the ensemble is reduced between $\approx 20\%$ and 70% in both experiments during DA cycles, showing that the DA system effi-

ciently influences the ensemble members. Moreover, the mean surface temperature anomaly from the early Holocene (ΔMST) is computed before and after applying DA by averaging over the proxy sites and comparing it to the proxy-based ΔMST (Figure 5.5). The DA results are mainly between the observations and the simulated ΔMST. In Exp_GLAC1D (Figure 5.5a), the intensity of the abrupt changes in BA and YD declines, and ΔMST aligns more closely with the observations until the end of YD. As with Exp_PaleoMist, the DA trajectory exhibits slightly higher temperatures than both observation and the ensemble mean of the prior during LGM. However, the trajectories closely follow the same pattern for BA and YD in Exp_PaleoMist.

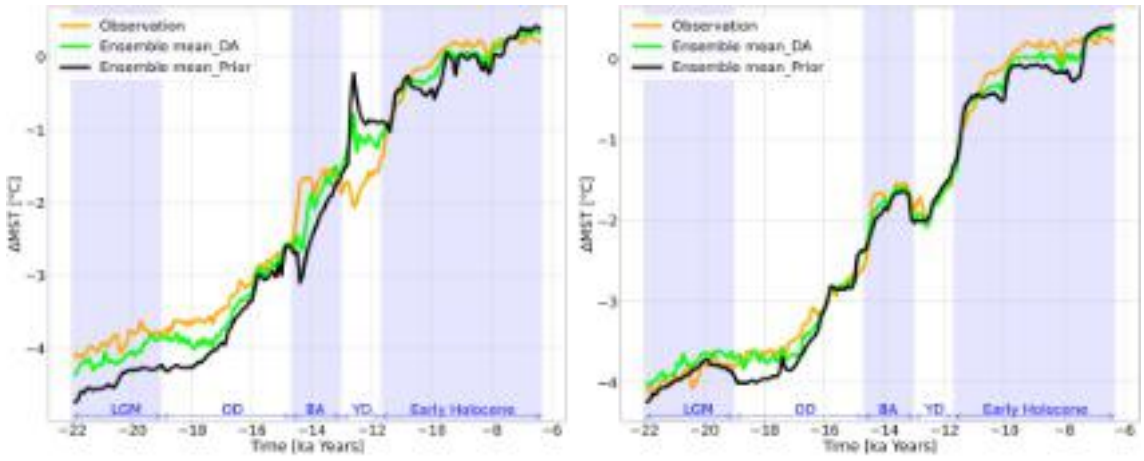


(a) (b)

Figure 5.5: Mean surface temperature change (ΔMST) calculated by averaging over the proxy locations for (a) Exp_GLAC1D and (b) Exp_PaleoMist. The orange, green, and black lines illustrate trajectories for observation, DA ensemble, and prior ensemble means, respectively.

To further analyze the deglacial dynamics, Figures 5.6 and 5.7 display the net North Atlantic FW, global SSS, AMOC at 26°N, and ΔGMSTs for Exp_GLAC1D and Exp_PaleoMist, respectively. Furthermore, the ensemble mean of DA and prior states is compared with the free run and a DA-based reconstruction conducted by Osman et al. (2021) (Figures 5.6d and 5.7d). Comparing the prior ensemble mean and the free run in Exp_GLAC1D (Figure 5.6d), the abrupt warming shift in the onset of YD reaches its maximum with a 300 year delay. However, the prior ensemble mean and free run trajectories are similar in Exp_PaleoMist, except for

a slightly warmer prior mean state during BA (Figure 5.7d).

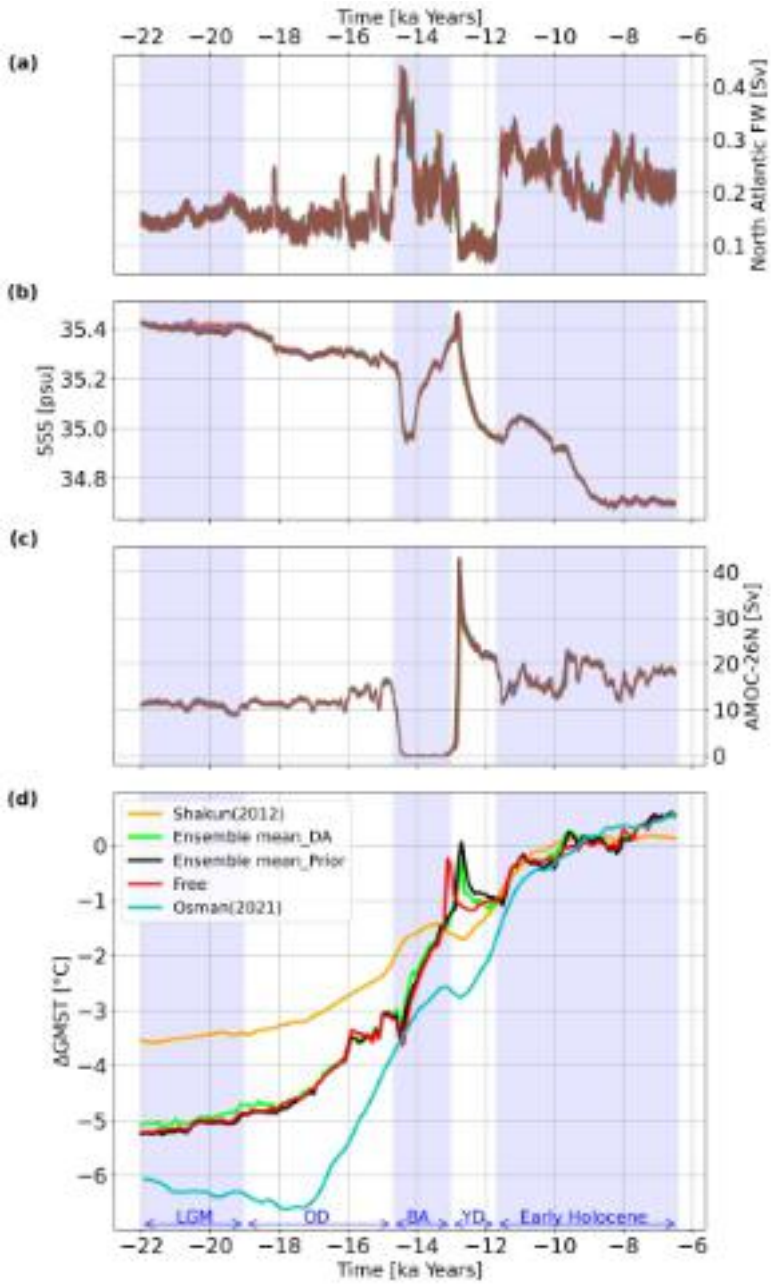


Figure 5.6: North Atlantic FW (a), SSS (b), AMOC at 26° north (c), and ΔGMSTs based on the model field (d) for Exp_GLAC1D. Different colors in (a), (b), and (c) correspond to ensemble members. The red line in (d) represents ΔGMST for the free run. The orange line in (d) is the proxy reconstruction of ΔGMST by Shakun et al. (2012) projected to 5° × 5° resolution.The blue line in (d) is the DA-based reconstruction of ΔGMST by Osman et al. (2021) .

In both experiments, the average SSS during the LGM is about one psu higher than during the early Holocene (Figures 5.6b and 5.7b), which is due to FW added to the ocean by melting ice sheets (Broecker, 2002; Clark et al., 2012). An increase in

FW leads to a decrease in AMOC strength. For example, the sudden increase in FW at the beginning of BA in Exp_GLAC1D leads to an off-state in AMOC with a rapid increase at the end of the BA (Figure 5.6a and c) which is more difficult to reconcile with proxy data (Lohmann and Schulz, 2000).

When global mean temperatures are considered, the DA solution in Exp_GLAC1D closely resembles the prior states (Figure 5.6d), but the warming trend reaches its maximum at the beginning of YD, with a reduction of approximately 0.2 degrees compared to the pre-DA state. A robust cooling trend is also observed in YD. These abrupt changes are consistent with AMOC variations. For Exp_PaleoMist (Figure 5.7d), the DA trajectory closely follows the global temperature of the prior state, implying that the paleo-observations have a minor effect on $\Delta$GMSTs during the last deglaciation when using the PaleoMist reconstruction. The DA, prior, and free trajectories exhibit two sudden upward shifts during the early Holocene in Exp_PaleoMist. This unrealistic feature can be attributed to the low temporal resolution of the PaleoMist reconstruction, which is 2500 years.

When comparing the DA solutions with Osman et al. (2021) reconstruction (Osman-DA; Figures 5.6d and 5.7d), the DA $\Delta$GMST trajectories are generally warmer then Osman-DA during the deglaciation. Specifically, when focusing on BA and YD, the timing and magnitude of these events in Exp_GLAC1D differ notably from the Osman-DA, but the DA pattern in Exp_PaleoMist is similar to that in the Osman-DA. However, the maximum warming in BA for Exp_PaleoMist occurs approximately 100 years earlier than in the Osman-DA. It is clear that discrepancies between the results and Osman-DA are due to utilizing different observation datasets, background states, and methods.

### 5.4.3 Surface temperature fields after DA

The DA has a significant effect on the pattern of the evolution of deglacial temperature. Figure 5.8 shows that the effect of DA is more pronounced at mid- and high-latitudes (from 3 °C to more than 5 °C) but small at low latitudes (less than 2 °C). When Exp_GLAC1D is compared with Exp_PaleoMist, it is observed that the DA system has a different effect in some regions due to the use

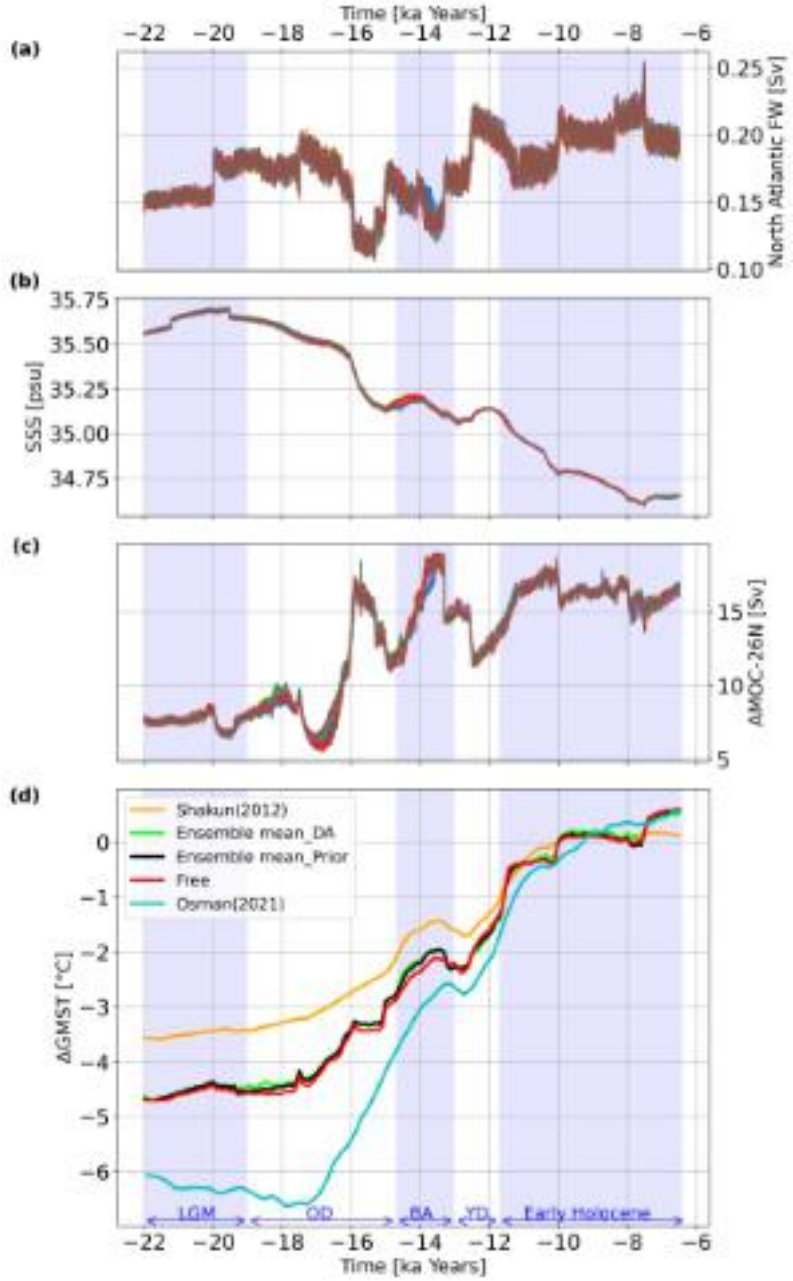


Figure 5.7: North Atlantic FW (a), SSS (b), AMOC at 26° north (c), and ΔGMSTs based on the model field (d) for Exp_PaleoMist. Different colors in (a), (b), and (c) correspond to ensemble members. The red line in (d) represents ΔGMST for the free run. The orange line in (d) is the proxy reconstruction of ΔGMST by Shakun et al. (2012) projected to 5° × 5° resolution.The blue line in (d) is the DA-based reconstruction of ΔGMST by Osman et al. (2021).

of different ice sheet reconstructions. For example, in Exp_GLAC1D during YD (Figure 5.8c), Antarctica transitions to a colder state after DA, while it becomes warmer in Exp_PaleoMist (Figure 5.8f). During BA, the discrepancies between the DA experiments are remarkable. In contrast to Exp_GLAC1D (Figure 5.8b),

Exp_PaleoMist (Figure 5.8e) shows strong cooling over the North Atlantic and warming over Antarctica and the Southern Ocean. Moreover, after DA, both experiments improve the Atlantic-Pacific seesaw phenomenon (e.g., Hoskins and Karoly, 1981; Kiefer et al., 2002; Romanova et al., 2006), characterized by the opposing temperature anomalies observed in the North Atlantic and North Pacific Ocean regions, except for the BA in Exp_GLAC1D.

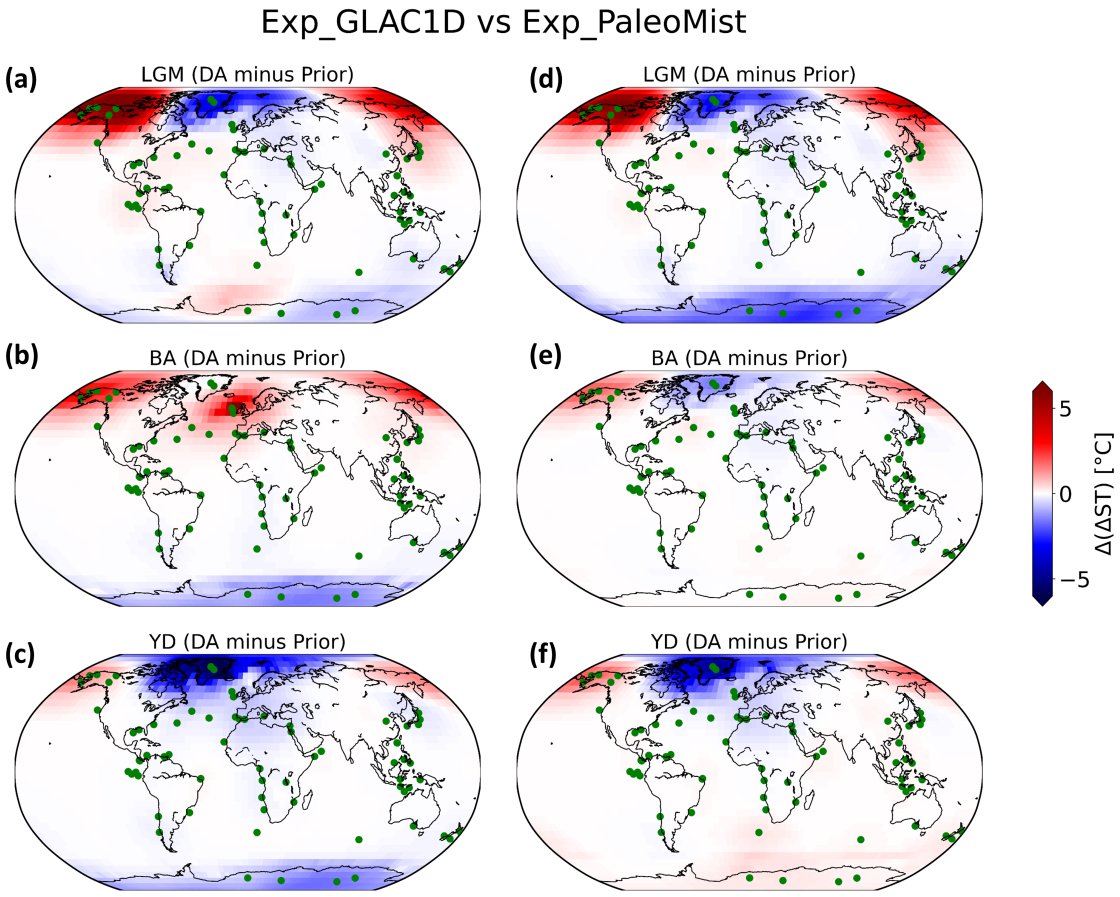


Figure 5.8: ΔST anomaly (DA minus Prior) in LGM, BA, and YD. (a), (b), and (c) show anomaly for Exp_GLAC1D and (d), (e), and (f) for Exp_PaleoMist. The green dots indicate the observation locations.

The BA is marked by a pronounced warming in the NH, particularly over Greenland (Buizert et al., 2014). Comparing the ΔGMST anomaly of BA against that of LGM (Figures 5.9a, d and 5.10a, d), the warming over Greenland and the North Atlantic increases by almost 5 °C with DA in both experiments. However, there are some cooling shifts over the North Pacific (Figures 5.9d and 5.10d), which is more evident in Exp_GLAC1D.

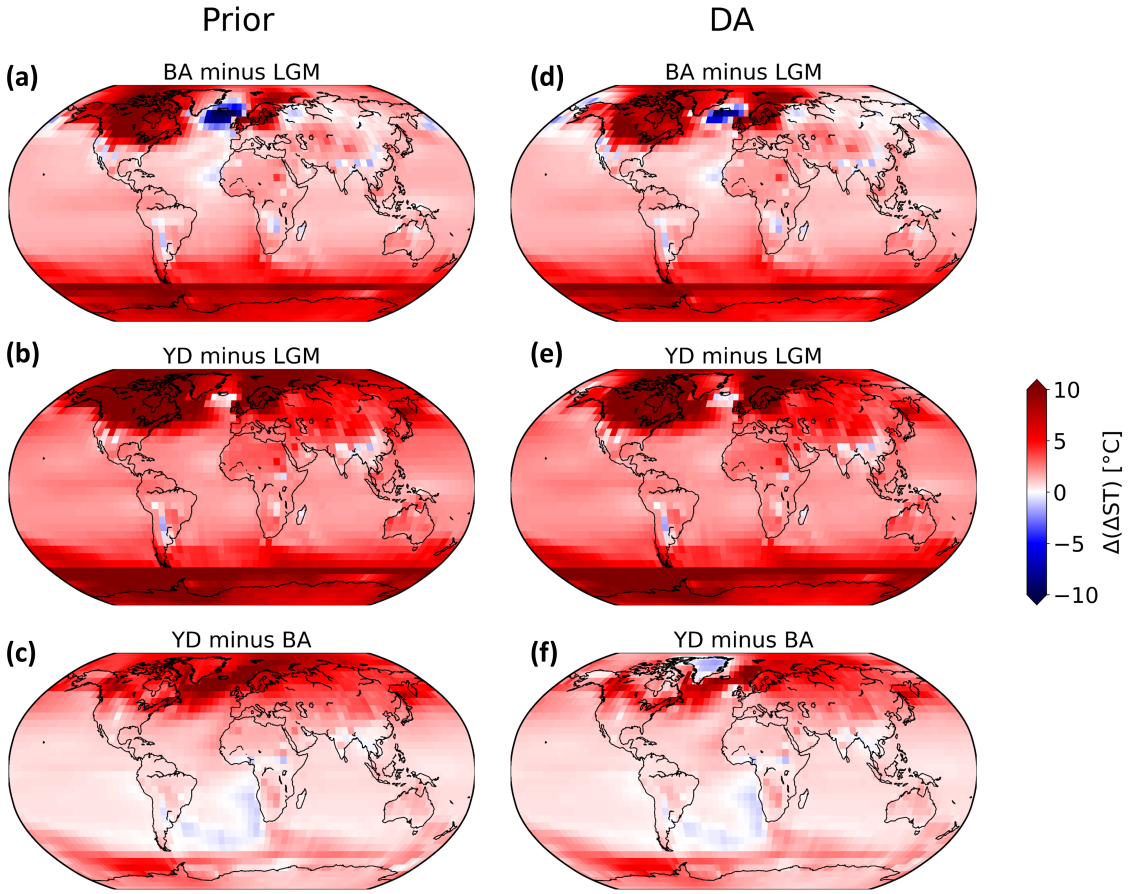


Figure 5.9: ΔST anomalies field for different time intervals in Exp_GLAC1D for before DA's implementation (a), (b), and (c) and after DA (d), (e), and (f).

In contrast to the BA, the average temperature in the NH decreased by several degrees during the YD, resulting in a return to near-glacial conditions. In the SH, the YD temperature did not vary significantly and was comparable to or even slightly warmer than BA (Shakun and Carlson, 2010; Stenni et al., 2011). These YD properties are enhanced by the implementation of DA. Figures 5.9f and 5.10f show that the NH climate in YD changes to a colder state after DA than in BA. Nevertheless, this change is more pronounced in Exp_PaleoMist. Without DA, the North Atlantic temperature drop between BA and YD could not be simulated.

## 5.5 Discussion

To overcome the computational challenges associated with long-term DA experiments in paleoclimate studies, this study has coupled CLIMBER-X with PDAF.

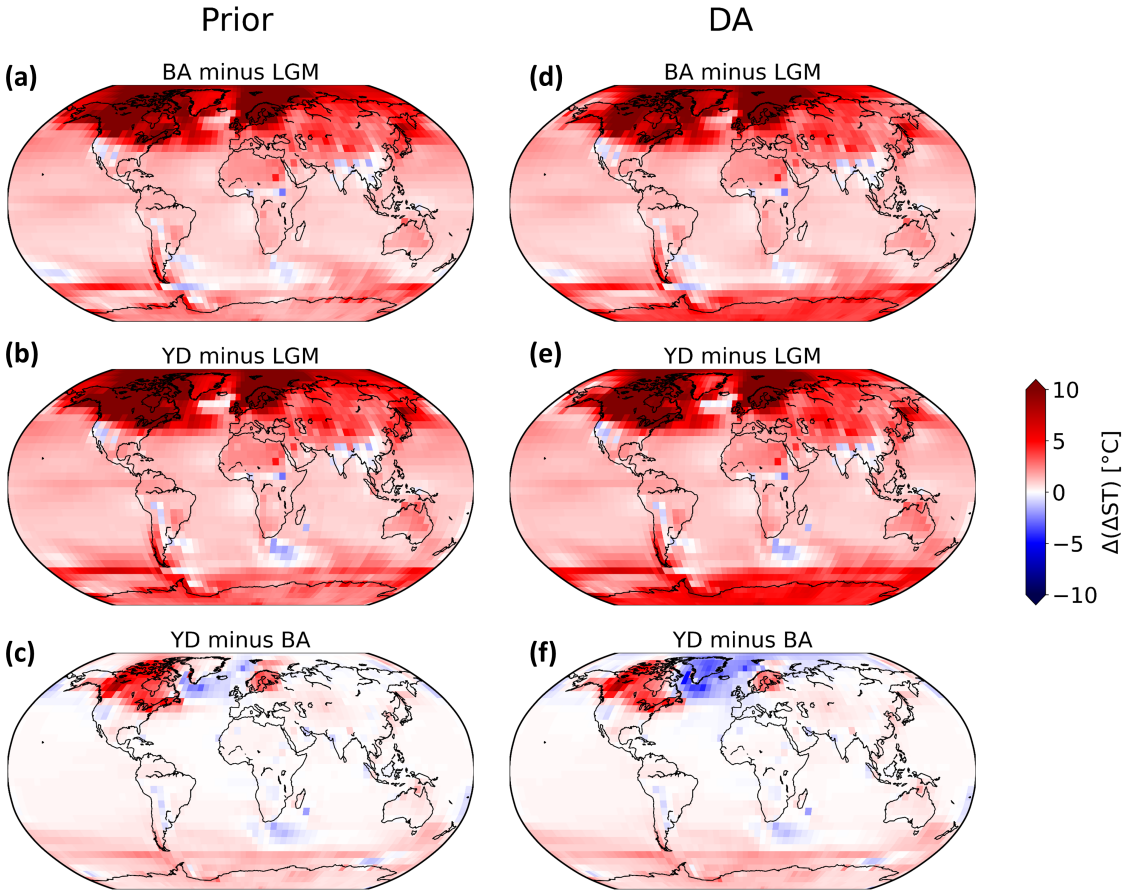


Figure 5.10: ΔST anomalies field for different time intervals in Exp_Paleomist for before DA's implementation (a), (b), and (c) and after DA (d), (e), and (f).

The DA experiments covering a span of 16500 years can be completed in approximately 40 hours. PDAF efficiently computes the DA update at each DA cycle in less than one second.

The choice of localization radius is an important factor in the DA system, and the optimal value was determined through trial and error. The optimal localization radius depends on various factors, including ensemble size, the spatial distribution of observations, and characteristics of observation errors (Kirchgessner et al., 2014). Ying et al. (2018) has shown that the optimal localization radius remains unaffected by properties of a quasigeostrophic model (Smith et al., 2002), such as resolution, as long as the model accurately represents the underlying dynamical processes. As discussed in the Experimental Design section, the 5000 km radius was selected to ensure the optimal impact of observations while avoiding unrealistic influences from distant observations on individual grid points. This radius mainly preserves the

effect of Greenland's observations, which are crucial for reconstructing the North Atlantic. The choice of localization radii for DA experiments involving CLIMBER-X and PDAF may vary depending on the specifics of the observation network.

A climate system consists of slowly varying components (e.g., ocean, cryosphere, land vegetation) and fast-varying components, primarily the atmosphere. The deterministic models, including CLIMBER-X, typically operate in a deterministic framework, where the averaged climate states are simulated based on deterministic mathematical equations, fixed initial conditions, external forcings, and parameterizations of fast-varying components (Flato et al., 2014). In contrast, stochastic climate models acknowledge the importance of considering the rapid fluctuations and introduce randomness to capture uncertainties and natural variability in the climate system (Palmer, 2012). Hasselmann (1976) emphasizes the significance of incorporating high-frequency elements in numerical models, as slow climate changes are defined as the response to ongoing random excitation by fast-varying component perturbations. By perturbing the near atmospheric surface temperature as a rapid-varying variable in the CLIMBER-X model, it has been transformed into a stochastic model, allowing for the representation of natural variability and uncertainties. This approach not only leverages the computational efficiency of CLIMBER-X but also provides more realistic background states for the DA system and avoids the ensemble collapses to a single state.

Climate models, including CLIMBER-X, are sensitive to FW fluxes (Kageyama et al., 2010; Otto-Bliesner and Brady, 2010; Stouffer et al., 2007), and the AMOC depends on FW forcing at locations where deep water forms (Stouffer et al., 2006). Accordingly, changes in AMOC are often considered to have caused abrupt climate changes during the last deglaciation (e.g., Lohmann and Schulz, 2000; Clark et al., 2002; McManus et al., 2004; Knorr and Lohmann, 2007). GLAC1D contains a significant ice volume loss during BA (Tarasov et al., 2012), associated with a pronounced MWP-1A, whereas PaleoMist (Gowan et al., 2021) does not contain a pronounced loss of deglacial meltwater during the BA. This is the main reason for the discrepancies between Exp_GLAC1D and Exp_PaleoMist. Moreover, ice sheet heights influence atmospheric and oceanic circulation (e.g., Löfverström et al.,

2014; Sherriff-Tadano et al., 2018), which may contribute to the disparities between simulations using GLAC1D and PaleoMist. Due to variations in methodologies, PaleoMist estimates the ice volume and ice sheet heights differently from GLAC1D. Mentioning briefly, PaleoMist calculates ice sheets using the program ICESHEET, which assumes that the ice sheet is in equilibrium (Gowan et al., 2016). In contrast, GLAC1D calculates Antarctica and North American ice sheets based on an ensemble average of several thousand ice sheet model simulations that fit constraints such as Holocene sea level changes and present-day uplift rates (Tarasov et al., 2012; Briggs et al., 2014).

The minor effect of DA on GMST trajectories could be attributed to the limited number of observations and the long period between DA cycles. The time gap between successive observations, 100 years, may exceed the model's predictability. Consequently, the prior ensemble loses the updated initial condition information entirely. This point is also mentioned by Matsikaris et al. (2015) and Acevedo et al. (2017) while comparing online and offline approaches. Therefore, in the experiments, GMST trajectories are mainly driven by external forcing, including ice sheets, GHGs, and orbital forcings. Increasing the frequency of model updates by employing high-temporal-resolution, well-distributed datasets covering more grid points can potentially improve the efficiency and impact of DA on GMST trajectories. However, the $\Delta$GMST trends for prior and DA in Exp_PaleoMist are similar to the Shakun et al. reconstruction and Osman-DA during BA and YD. This indicates that the choice of ice-sheet reconstruction resulting in different prior states is consequential in the DA system.

Osman et al. (2021) employ an offline EnSRF approach (Tierney et al., 2020b) and assimilate the different types of geochemical proxies for SST (Tierney et al., 2020b) directly using Bayesian proxy forward models (e.g., Tierney and Tingley, 2014). They also draw the prior states from the separate time slice simulations conducted by the isotope-enabled Community Earth System Model (iCESM; Brady et al., 2019). These methodological disparities between their DA setup and ours explain the differences between the results. Nevertheless, Exp_PaleoMist is roughly consistent with Osman-DA regarding the magnitude and speed of the warming-cooling-

warming tendency over BA and YD. This suggests that despite the differences in methodology and background states, there is some agreement regarding the general pattern of GMST changes during those time intervals.

In contrast to the effect of DA on GMST trajectories, DA has changed the spatial pattern of the surface temperature fields significantly. This implies that the impact of DA is more prominent at regional scales rather than at the global mean scale. The point that the climate sensitivity of CLIMBER-X is 3.3 K, which drops in the middle range for the Earth system models (Willeit et al., 2022), suggests that the model is responsive to $CO_2$ forcing and insolation. As a result, the main drivers in the low latitudes, such as GHG concentrations and insolation, dominate in shaping the temperature patterns in those regions. Consequently, the effect of DA is less pronounced in low latitudes where the model has already captured these primary drivers well.

However, in high latitudes, particularly over the North Atlantic and Greenland, where the ice sheet heights, FW pattern, and AMOC play significant roles in atmospheric and oceanic circulations and temperature patterns, DA enhances the characteristics of BA and YD. This denotes that the assimilation of observational data has helped skillfully to have more realistic temperature patterns and climate variability during these specific periods.

Additionally, it is worth mentioning that DA has enhanced the Atlantic-Pacific seesaw pattern, mainly for Exp_PaleoMist, indicating an improved representation of the coupled atmosphere-ocean dynamics in these regions. Several studies have reported this heterogeneous phenomenon in both model and data sets during glacial and deglacial periods (e.g., Kiefer et al., 2002; Meyer et al., 2017; Wang et al., 2021). Different factors, including oceanic and atmospheric circulation patterns, heat transport, and interactions between the oceans and atmosphere, contribute to the evolution and endurance of this seesaw pattern (e.g., Romanova et al., 2006; Deser et al., 2010; Delworth et al., 2017; Gong et al., 2019). Therefore, the assimilation of observational data has contributed to a more realistic simulation of the interhemispheric temperature gradient and associated oceanic circulation patterns.

# Chapter 6

# Assimilation of sub-layers temperatures

In the context of online DA for paleoclimate reconstruction, slow components like the ocean are critically important. Online DA estimates both time-mean states and initial conditions for subsequent DA cycles, which leverages the inherent predictability of the system. The ocean, with its relatively slow dynamics, significantly extends the predictability of the climate system compared to the atmosphere alone. This extended predictability is crucial because it allows the DA system to maintain more accurate initial conditions over longer periods, thereby improving the overall performance of the online DA compared to offline DA, which only estimates time-mean states without updating initial conditions. It is also unclear how well the variability in a subsurface ocean, where prominent predictability resides (e.g., Chikamoto et al., 2013), can be reconstructed using online-DA assimilating only surface variables, which most proxies represent.

In addition, McManus et al. (2004) find that during the coldest periods of the deglaciation, specifically around 17.5 kyr BP with HS1, the AMOC nearly or completely collapsed. This period was marked by a massive discharge of icebergs, which introduced significant amounts of FW into the North Atlantic, destabilizing the water column and weakening the AMOC. Similarly, around 12.7 kyr BP, during the YD cold event, there was a sharp but brief decline in the AMOC. These events highlight the sensitivity of the AMOC to FW inputs from melting ice sheets. Following

these cold periods, McManus et al. (2004) indicate rapid resumption and acceleration of the AMOC, which coincided with the two most significant regional warming events of the deglaciation. The rapid reinvigoration of the AMOC during these times suggests a strong link between AMOC activity and abrupt climate warming. The BA warming period, beginning around 14.7 kyr BP, marked a significant resurgence of the AMOC, likely contributing to the accelerated melting of ice sheets and rising sea levels. Moreover, Max et al. (2022) identifies a clear link between subsurface warming and weakened AMOC. During periods of reduced AMOC, there is a build-up of subsurface heat, which eventually triggers the ice-sheet instabilities that characterize HEs. The authors provide detailed evidence from geochemical proxies and age models to support this relationship, emphasizing the role of ocean circulation changes in initiating these abrupt climate events.

Considering the importance of understanding subsurface ocean dynamics in the online DA, AMOC, and climate variability, this chapter aims to develop the DA technique presented in Chapter 5 to assimilate the subsurface temperatures into the simulation of the last deglaciation.

## 6.1 Observations

No real data sets for temperature ocean layers covering the last deglaciation exist. Given that the PaleoMist outperforms GLAC1D in the simulation of the last deglaciation (Chapter 4), the subsurface temperature of Paleomist_full (Section 4.2) is used as a basis for constructing the observation network in this chapter. In addition, the signal of AMOC strength is added to the temperature layers ($Temp_{Layer}$) of Paleomist_full as

$$Temp_{Layer} = Temp_{Layer} + Temp_{Layer} \times Coefficient, \tag{6.1}$$

where $Coefficient$ is estimated based on $^{231}\mathrm{Pa}/^{230}\mathrm{Th}$ ratio provided by McManus et al. (2004). $^{231}\mathrm{Pa}/^{230}\mathrm{Th}$ is anticorrelated by AMOC strength, meaning that by increasing the ratio, AMOC weakens (McManus et al., 2004; Figure 6.1). Figure B.1 compares the observation created in this chapter with PaleoMist_full. The error of

0.5 °C is considered for all layer temperatures. This uncertainty is comparable with the ensemble standard deviation (≈0.3-0.5) in DA experiments in this chapter.

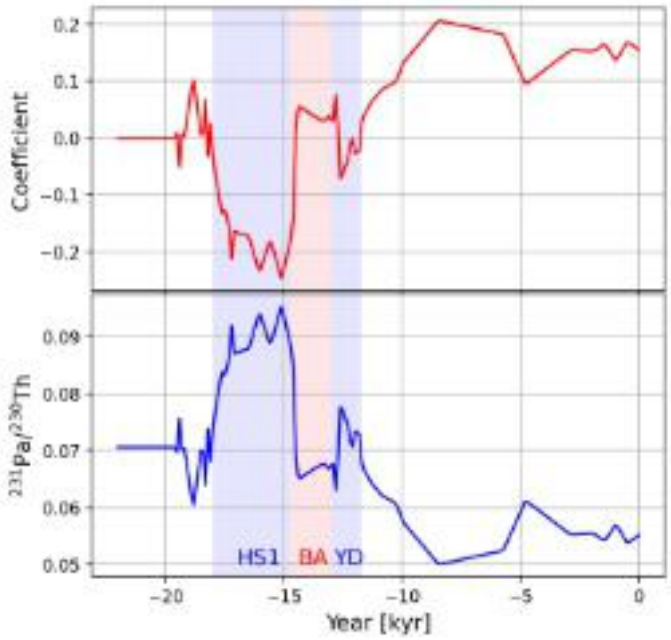


Figure 6.1: $^{231}$Pa/$^{230}$Th ratio provided by McManus et al. (2004) and the coefficient estimated based on this ratio.

## 6.2 Experimental Design

Two sets of transient deglaciation simulations, Exp_GLAC1D and Exp_PaleoMist, are conducted, each consisting of two simulations: with DA (GLAC1D_DA and PaleoMist_DA), without DA (GLAC1D_Free and PaleoMist_Free). Version 2 of CLIMBER-X (https://doi.org/10.5281/zenodo.6877358), which is slightly different from Version 1 employed in Chapter 5, is made stochastic following the method in Section 5.3. Therefore, the model outputs may differ from the simulations in Chapter 5 while the same forcings are applied to the simulations in both chapters. As in Chapter 5, the DA experiments employ GLAC1D and PaloeMist for the ice sheet reconstruction, bathymetry, and land-sea mask. Moreover, the simulations are forced by GHGs and orbital parameters. Here, the transient simulations start from the 18 kyr BP initial condition. In simulations with DA, the model is run until 14.7 kyr BP (before the BA period) with assimilating surface and subsurface ocean

temperatures (temperature of 23 layers) conducted every 100 years and continues until year 9 kyr BP without implementing DA. However, in simulations without DA, the model is run from 18 ky BP to 9 ky BP without any DA implementation. The method presented in Section 5.2 is followed for the DA. However, localization is not used here because the temperatures of all ocean areas are assimilated into the model, meaning that an observation exists at each ocean grid point. Therefore, the DA algorithm is ESTKF (Section 3.3) and the state vector contains not only surface temperature but also subsurface temperatures (22 layers).

## 6.3 Results and Discussion

### 6.3.1 Exp_GLAC1D vs Exp_PaleoMist

Figures 6.2 and 6.3 compare temperature trajectories before and after DA for Exp_GLAC1D and Exp_PaleoMist, respectively. The DA results are mainly between the observations and the simulated temperatures for the upper and middle layers. However, in deep layers, DA trajectories have more fluctuations and are closer to the prior states. This pattern is more pronounced in Exp_PaleoMist.
In Exp_GLAC1D, it is evident that the green line, representing DA, shows generally higher values, particularly during YD and the early Holocene, in North Atlantic FW flux compared to the black line (GLAC1D_Free; Figure 6.4a). This suggests that DA results in higher FW flux estimates. In the PaleoMist experiment (Figure 6.4b), both lines are relatively similar, but the DA line exhibits a different trend during YD and the onset of the early Holocene. Figure 6.5 indicates that DA considerably increases the precipitation over the North Atlantic, resulting in more FW flux during GLAC1D_DA. The changes in FW fluxes in GLAC1D_DA and PaleoMist_DA are consistent with the precipitation and evaporation trend (Figure 6.5).
SSS is generally anti-correlated with FW. With an increase in FW, SSS decreases. North Atlantic SSS shows considerable variability introduced by DA in the Exp_GLAC1D (Figure 6.4c). The GLAC1D_DA and GLAC1D_Free display a noticeable decline during the HS1 period. While GLAC1D_Free SSS rises to the level of HS1 during YD, GLAC1D_DA can not exceed 32 psu due to more FW fluxes. In the

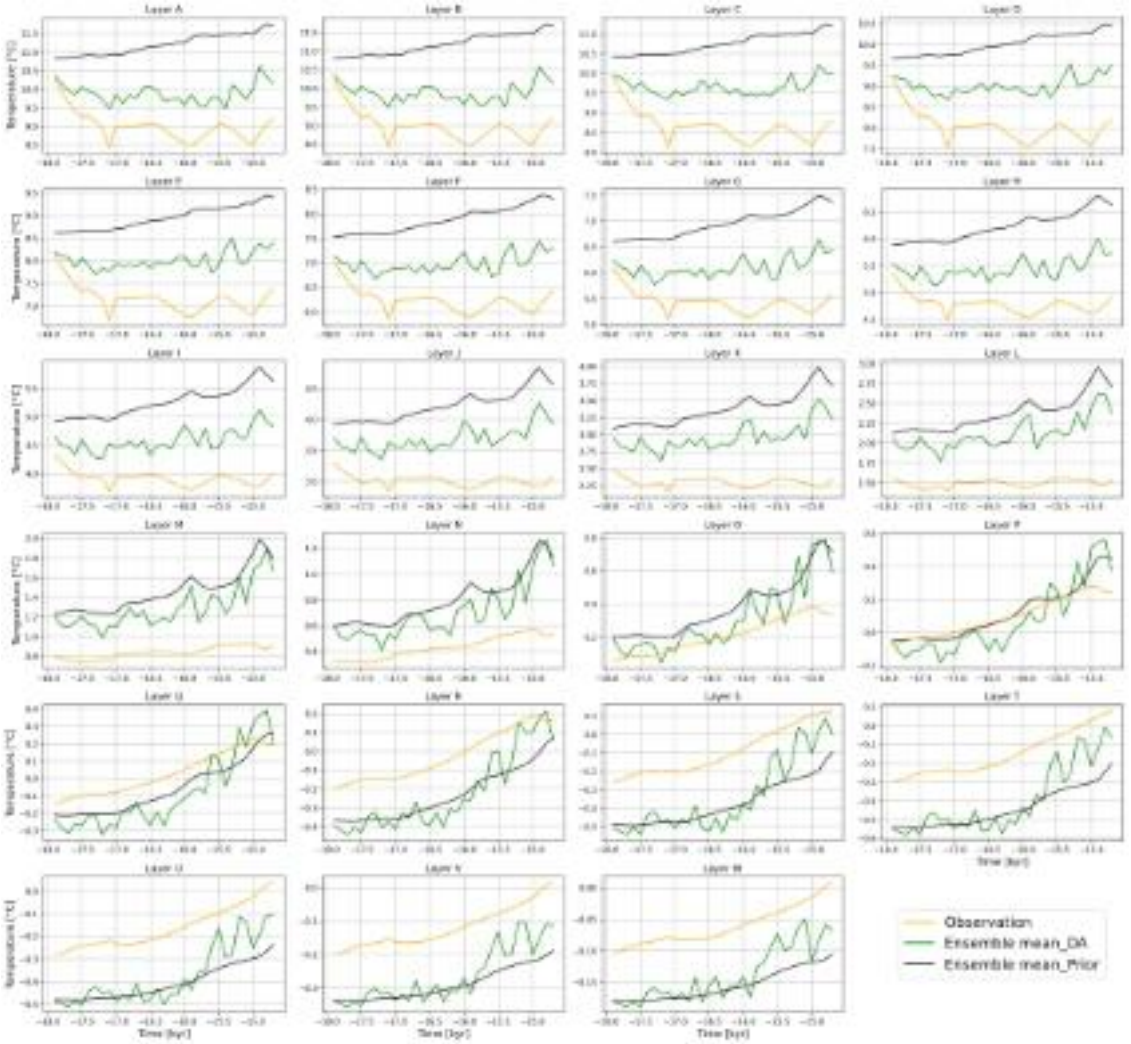


Figure 6.2: Mean temperature for 23 layers of the ocean for Exp_GLAC1D. Layer A is the surface layer (≈5 m), and Layer W is the deepest layer (≈5000 m). The layers have different depths. The orange, green, and black lines illustrate trajectories for observation, DA ensemble, and prior ensemble means, respectively.

Exp_PaleoMist (Figure 6.4d), both the DA and Free lines show a significant drop in salinity during the HS1 and YD periods, which are consistent with FW forcing.

Many studies show that an influx of freshwater can lead to a weakening of the AMOC (e.g., Lohmann and Schneider, 1999; Knorr and Lohmann, 2007; Zhang et al., 2017; Haskins et al., 2020; Swingedouw et al., 2022; He and Clark, 2022). The reduction in AMOC strength occurs because the added freshwater decreases SSS, making the surface waters less dense and inhibiting the sinking process, which is crucial for AMOC function. Consistent with FW and SSS, AMOC shifts to the offline mode in Exp_GLAC1D (Figure 6.4e) at the onset of BA. AMOC in

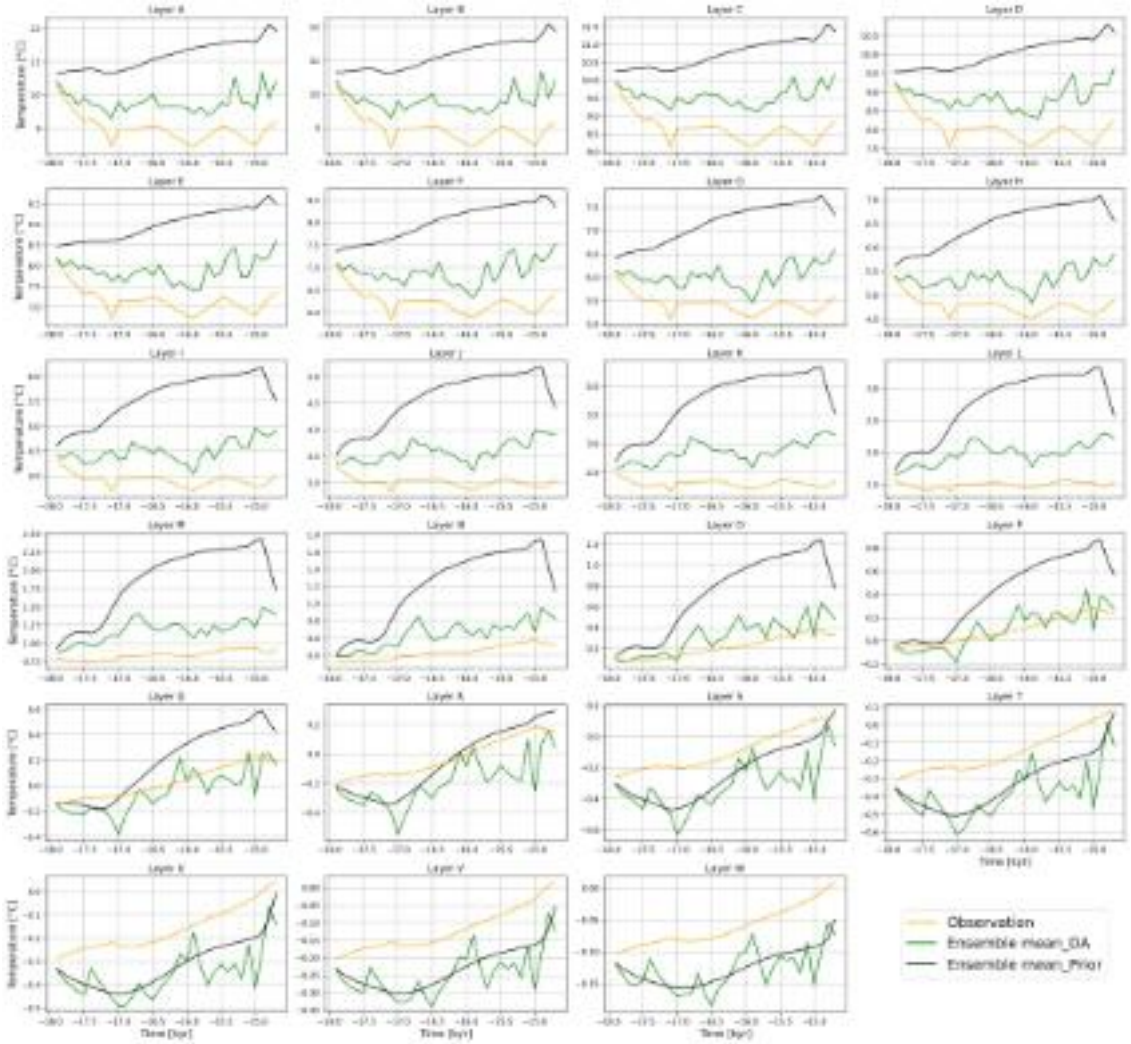


Figure 6.3: Mean temperature for 23 layers of the ocean for Exp_PaleoMist. Layer A is the surface layer (≈5 m), and Layer W is the deepest layer (≈5000 m). The layers have different depths. The orange, green, and black lines illustrate trajectories for observation, DA ensemble, and prior ensemble means, respectively.

GLAC1D_DA can not recover during the rest of the simulation due to higher FW flux. In Exp_PaleoMist (Figure 6.4f), both lines drop significantly during HS1 and YD and increase abruptly at the end of HS1. However, the timing and magnitude of PaleoMist_DA are different from PaleoMist_Free. The weak AMOC during HS1 and YD in Exp_PaleoMist is in agreement with proxies analyzed by McManus et al. (2004) (Figure 6.1).

Due to the shutdown of AMOC, Exp_GLAC1D can not simulate the warming in the North Atlantic during BA (Figure 6.4g). DA can not help to capture the warming/cooling/warming sequence in Exp_GLAC1D in the North Atlantic. Re-

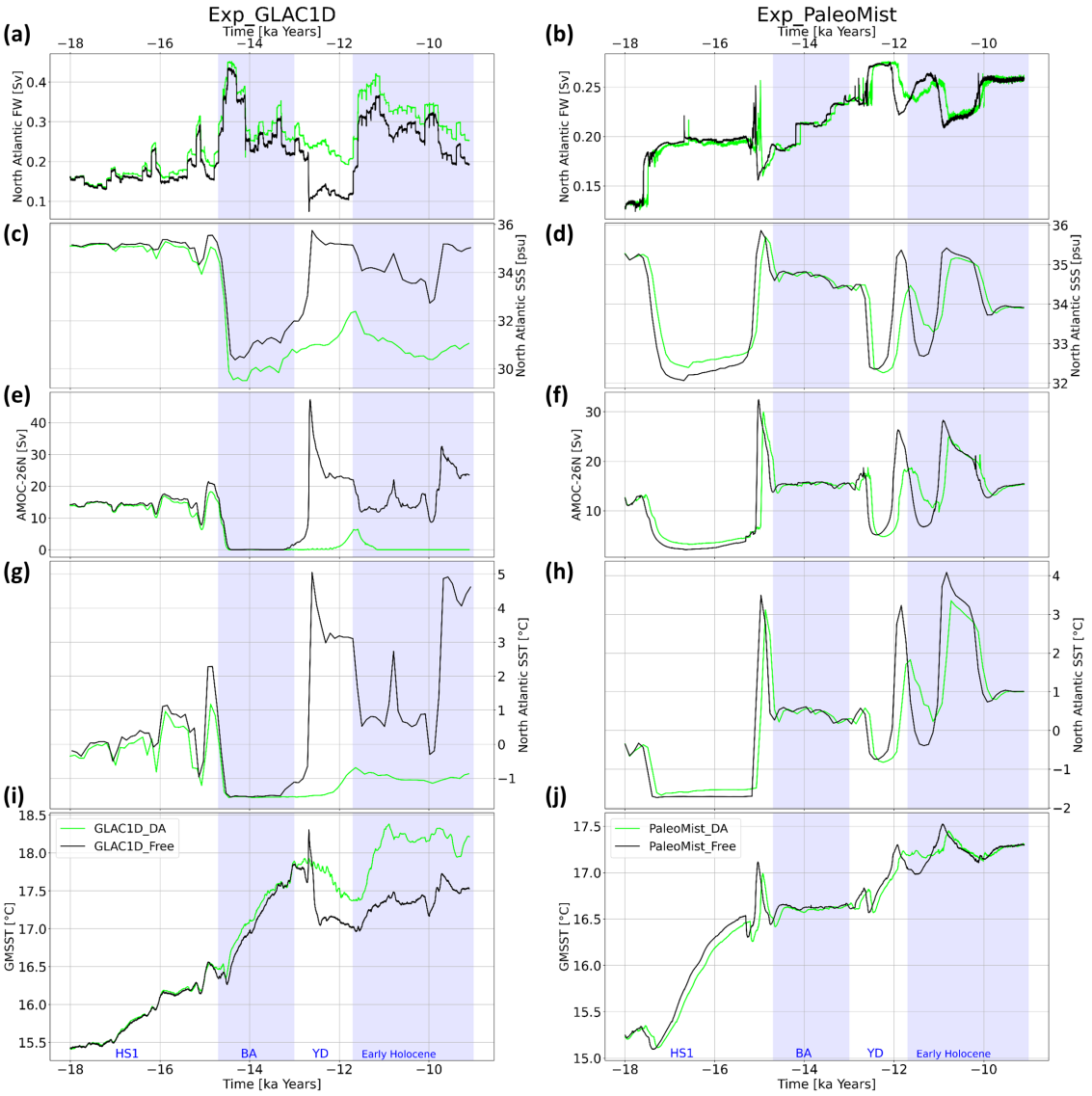


Figure 6.4: North Atlantic FW, North Atlantic SSS, AMOC at 26°N, North Atlantic SST and GMSST for Exp_GLAC1D (a),(c),(e),(g),(i) and for Exp_PaleoMist (b),(d),(f), (h) and (j). HS1 as 18-14.7 kyr BP, BA as 14.7-13 kyr BP, and YD as 13-11.6 kyr BP. North Atlantic index for SSS and SST is defined as an average over 50°N-70°N and 45°W-0°W. Note that the vertical axes differ for Exp_GLAC1D and Exp_Paleomist. North Atlantic FW flux encompasses precipitation-evaporation, sea ice fluxes, land runoff, and liquid water flux melted from ice sheets.

garding Exp_PaleoMist (Figure 6.4h), DA slightly changes the timing of the abrupt warming/cooling at the end of the HS1, but the temperature remains almost constant during BA. Further, DA enhances the cooling and its duration during YD in PaleoMist_DA.

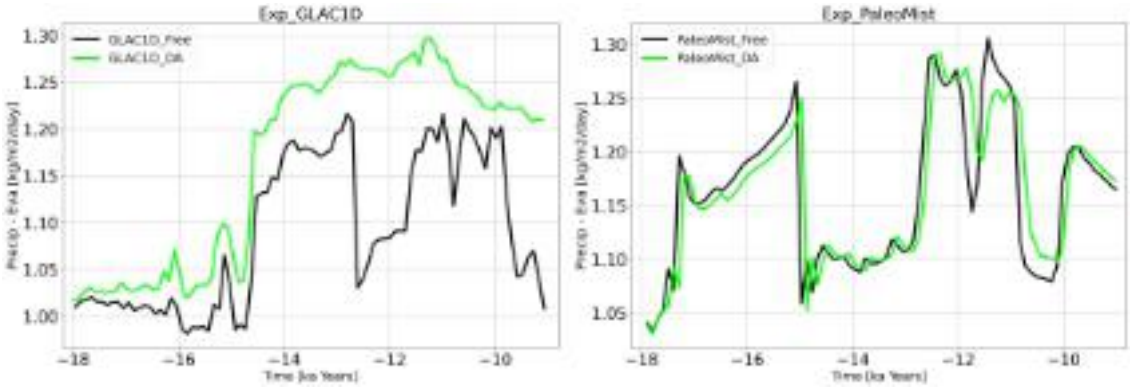


Figure 6.5: North Atlantic precipitation minus evaporation for Exp_GLAC1D (left) and Exp_PaleoMist (right) during the last deglaciation. North Atlantic index is defined as an average over 50°N-70°N and 45°W-0°W.

The global mean surface temperature (GMSST) panels (Figures 6.4i and 6.4j) reveals that both the DA and Free lines show a gradual increase over time in both experiments. GLAC1D_DA simulates GMSST with less variability than GLAC1D_Free during BA and YD, but it can not replicate the warming/cooling/warming in the time comparable with data sets (e.g., Shakun et al., 2012). GLAC1D_DA peaks at the onset of YD, followed by cooling until the start of the early Holocene. In the Exp_PaleoMist, in line with FW and AMOC, GMSST trends are similar in Paleomist_Free and PaleoMist_DA. Both simulate abrupt warming/cooling/warming sequences before the BA and in YD. However, the timing of these events in PaleoMist_DA (6.4j) is different. The events happen by a delay of approximately 100 years in PaleoMist_DA.

### 6.3.2 DA using modified PaleoMist

As shown in the chapters 4 and 5, the ice sheet reconstruction is the main source of uncertainty in the simulation of the last deglaciation, which can strongly influence the DA results. Figures 4.2h and 6.4j indicate that simulations employing PaleoMist capture a warming/cooling/warming signal earlier than the BA/YD sequence. This section conducts some extra simulations to examine the possibility of capturing BA/YD at the right time by manipulating PaleoMist ice sheet reconstruction. PaleoMist presents ice sheets from 80 kyr BP to the present with a time resolution of 2500 years. To generate the different FW forcing prescribed by ice

sheets, the linear interpolation is first used to change the time resolution to 100 years, then the variables of PaleoMist are shifted 400, 500, and 1000 years towards the present day and are saved in files named PaleoMist_400, PaleoMist_500, and PaleoMist_1000, respectively. Figure 6.6 shows the simulations using these new files as ice sheet reconstructions and compares them with PaleoMist_Free. The stochastic version of CLIMBER-X is employed here to do simulations.

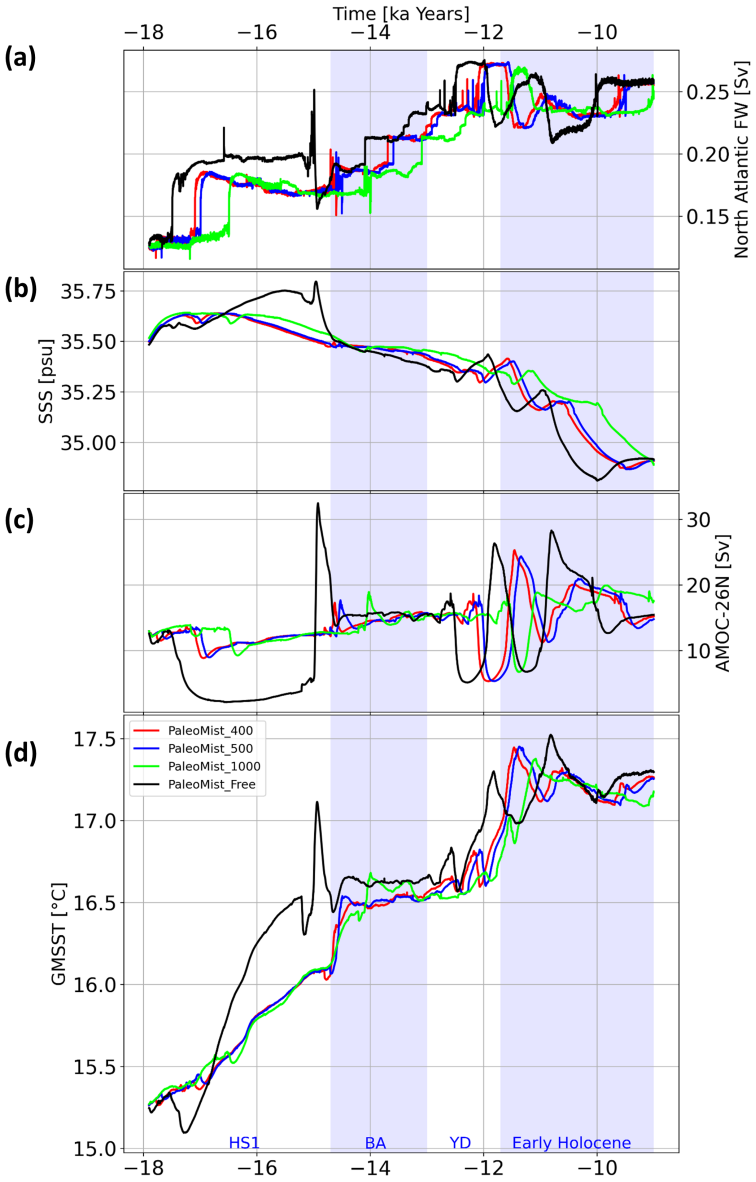


Figure 6.6: North Atlantic FW (a), global SSS (b), AMOC at 26°N (c), and GMSST (d) for PaleoMist_400, PaleoMist_500, PaleoMist_1000, and PaleoMist_Free.

The magnitude and variability of FW flux induced by the modified PaleoMists are less than PaleoMist_1000, and the timing of FW is also different (Figure 6.6).

Therefore, SSS, AMOC, and GMSST follow different patterns. The abrupt warming/cooling/warming sequence is not observed in PaleoMist_400, PaleoMist_500, and PaleoMist_1000. These simulations present almost a continuous warming during HS1. After a 0.5 °C increase, GMSST remains constant during BA and rises from the onset of YD in PaleoMist_400 and PaleoMist_500. PaleoMist_1000 continues warming until 14 kyr BP but does not show notable cooling for in YD.

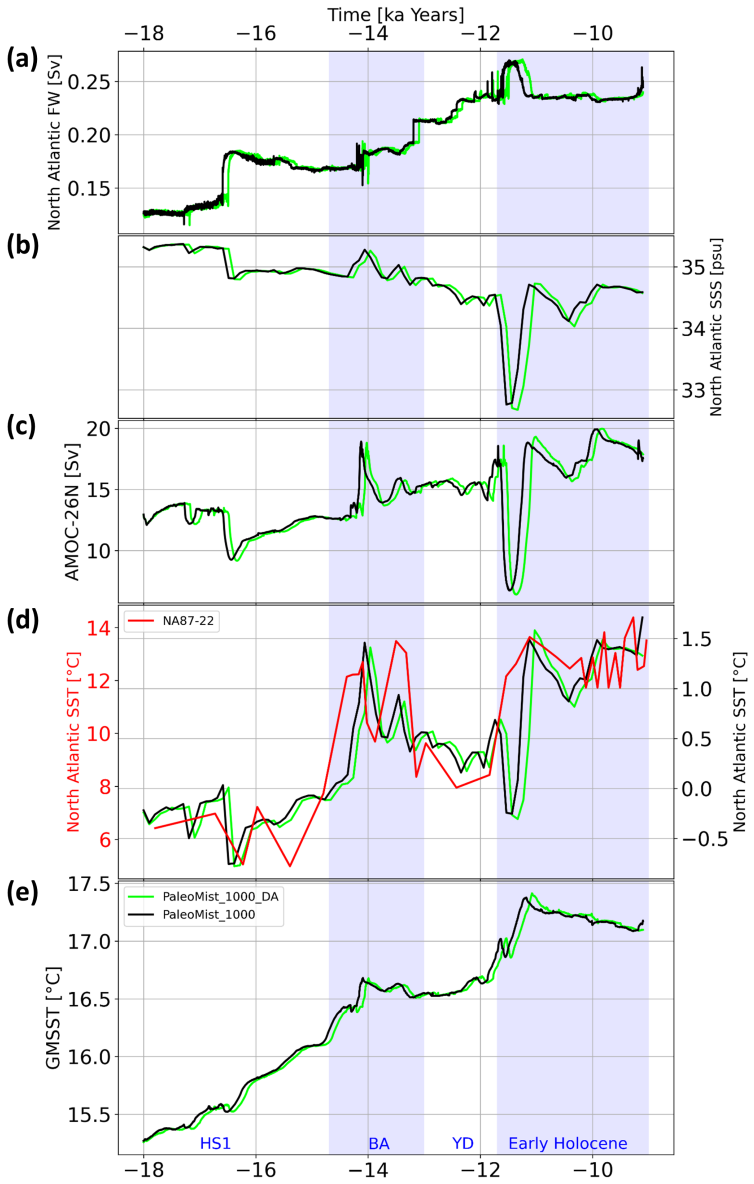


Figure 6.7: North Atlantic FW (a), North Atlantic SSS (b), AMOC at 26°N (c), North Atlantic SST (d) and GMSST (e) for PaleoMist_1000. North Atlantic index for SST is defined as an average over 50°N-70°N and 45°W-0°W. The red line in (d) presents North Atlantic SST derived from proxy NA87-22 (Shakun et al., 2012).

Since PaleoMist_1000 captures BA warming better, another DA experiment is here

conducted employing PaleoMist_1000 (Figure 6.7). DA does not change considerably the FW forcing in this experience (Figure 6.7a). Therefore, North Atlantic SSS, AMOC, SST, and GMSST trends are similar in PaleoMis_1000 and PaleoMist_1000_DA. However, DA shifts the events, particularly for North Atlantic SST. Figure 6.7d indicates that North Atlantic trends in PaleoMist_1000 and PaleoMist_1000_DA, particularly over BA and YD, agree with a North Atlantic SST proxy (Wang et al., 2021). There are two warm peaks in BA and cooling during YD (Figure 6.7d). However, the abrupt reduction at the onset of the early Holocene is not comparable with the proxy (Figure 6.7d).

# Chapter 7

# Final Considerations

## 7.1 Conclusions

This thesis uses the climate model CLIMBER-X to conduct the transient simulation of the last deglaciation forced by ice sheet reconstruction, GHGs concentration, and orbital parameters. Further, the PaleoMist ice sheet reconstruction is used as a new boundary condition for the last deglaciation simulation. Moreover, this study presents and develops an online DA technique for reconstructing the last deglaciation. The research objectives formulated at the beginning of this thesis guided the research documented in Chapters 4, 5 and 6 and a concise conclusion of these chapters is given in the following:

1. **To investigate the impact of a novel ice-sheet reconstruction on the simulation of the last deglaciation and to examine the roles of GHGs and orbital forcings in this context.** (Chapter 4)

   This study pioneers the use of the PaleoMist ice sheet reconstruction Gowan et al. (2021) to simulate the last deglaciation, contrasted with the more traditional GLAC1D reconstruction (Tarasov et al., 2012; Briggs et al., 2014). In both PaleoMist and GLAC1D simulations, LGM temperatures and southern ocean Atlantic SSTs are consistent with data assimilation-based estimates of Tierney et al. (2020b) and MARGO (2009), respectively.

   Variations in sea level pressure, wind patterns, and surface temperatures,

especially during the BA warm period, illustrate the different behaviour of GLAC1D and PaleoMist. These differences are attributed to the varying configurations, extents, and topographies of the ice sheets, affecting the atmosphere-ocean circulation. It is shown that the pronounced warming in the northern North Atlantic, which is a main characteristic of BA (Buizert et al., 2014), is better captured by the PaleoMist simulation compared to GLAC1D in agreement with previous studies (e.g., Bethke et al., 2012; Kapsch et al., 2022; Bouttes et al., 2023), it is found that the timing and magnitude of climate events during the termination are affected by the ice sheet reconstruction. PaleoMist shows greater glacial ice sheet heights, particularly in the NH, while GLAC1D has a substantial ice sheet volume loss, causing an off-mode in the AMOC during the BA. The strong fluctuations in deglacial meltwater in GLAC1D lead to abrupt changes in global mean temperature and fail to capture the BA/YD transition sequence. The FW derived from PaleoMist does not induce an off-mode AMOC during the BA but a pronounced warming in the North Atlantic realm. The YD cooling in the PaleoMist simulation seems to be underestimated for this area, especially over Greenland where most likely a pronounced overshoot dynamics is relevant (Knorr and Lohmann, 2003; Zhang et al., 2017; Lohmann et al., 2020). The exact timing of the BA/YD sequence with respect to Shakun et al. (2012) and data assimilation-based (Osman et al., 2021) reconstructions is a subject of further investigation. Besides model uncertainties, dating uncertainties of marine sediment cores due to changes in reservoir ages cannot be excluded (e.g., Butzin et al., 2017; Lohmann et al., 2020).

Assessing the contributions of ice sheets, GHGs, and orbital forcing to warming during the last deglaciation, the significant role played by both GHGs and orbital forcing in regulating the FW flux into the North Atlantic is demonstrated, consequently affecting SSS and ocean circulation, consistent with He (2011) and Bethke et al. (2012). It is likely that the timing of deglacial transitions is particularly influenced by the magnitude of FW fluxes associated with the retreat of NH ice sheets (Knorr and Lohmann, 2003, 2007; Ganopol-

ski and Roche, 2009). As an extreme case, Liu et al. (2009) proposed that BA warming is controlled by the cessation of FW input, highlighting the significant role of deglacial FW in the abrupt recovery of AMOC. However, this FW history would be inconsistent with paleo-sea level proxies and both ice sheet reconstructions used here. It is indicated that GHGs and orbital forcing influence the precipitation patterns, affecting the proximity of the AMOC to its bifurcation point between the on- and off-mode states. A significant reduction in FW input can lead to a shift in AMOC to a more stable mode. The experiments could be further developed as a way to better assess the history of ice sheet evolution. Climate-ice sheet models combined with data assimilation could be suitable for estimating the ice sheets and deglacial meltwater.

The dynamics of the last termination include a reduction in the height of the ice sheets and an increase in GHG concentrations to achieve appropriate warming. The direct effect of orbital forcing on global mean surface temperature is relatively small. This will be different in a fully interactive Earth system model including ice sheets (e.g., Ganopolski and Brovkin, 2017; Willeit et al., 2019), then the glacial termination is triggered by orbital forcing.

2. **To design and implement a DA technique for the transient simulation of the last deglaciation.** (Chapter 5)

   This study introduces a fast and efficient method for conducting DA using an EMIC, CLIMBER-X (Willeit et al., 2022). Since CLIMBER-X has no internal noise in the system, a stochastic version of this model was applied. In addition, two different ice sheet reconstructions, GLAC1D (Tarasov et al., 2012) and PaleoMist (Gowan et al., 2021), were used to investigate the effects of different model backgrounds on the climate evolution during the last deglaciation. The conclusions of this part are summarized in the following main points:

   - The choice of ice sheet reconstruction significantly impacts model simulations, affecting ocean FW forcings and AMOC, leading to different circulation and temperature patterns during the deglaciation. The free simulation with the PaleoMist ice sheet reconstruction provides a more

consistent trend than that with GLAC1D, especially during the BA/YD sequence. Accordingly, the ice sheet reconstructions lead to different effects of the DA.

- While DA has a minor effect on global mean surface temperature trajectories, it has significantly influenced the surface temperature fields, suggesting that the impact of DA is more prominent at regional scales rather than at the global mean scale. The DA system improves the surface temperature spatial heterogeneity (Atlantic-Pacific seesaw), representing the climate patterns for YD and BA, especially for the PaleoMist experiment.
- The effect of DA is more pronounced at high latitudes than at mid and low latitudes, potentially indicating disparities or inadequate representation of physical processes within the model. Considering its climate sensitivity, CLIMBER-X performs relatively more accurately in low latitudes, where the main driver is $CO_2$ forcing, compared to high latitudes.
- The online DA approach allows us to study the performance of CLIMBER-X, including AMOC, salinity, FW, and many other climate parameters. Nevertheless, the effect of the online approach is not notable on the climate variables primarily due to the long time gaps between DA cycles and due to the fact that temperature is damped out faster than other variables like salinity (Lohmann and Schneider, 1999).

3. **To investigate the effect of the assimilation of oceanic subsurface temperature on the simulation of the last deglaciation.** (Chapter 6)

   This study develops the combination of CLIMBER-X and PDAF to implement DA of the subsurface temperatures. An ideal observation network was generated and assimilated to the simulation of the last deglaciation using the stochastic version of CLIMBER-X. The conclusions of this part are summarized in the following main points:

   - The simulations done by the stochastic CLIMBER-X show some differences from those conducted by the deterministic version of CLIMBER-X

(Chapter 4). This point illustrates the importance of choosing the source of randomness added to the model.

- The update of initial conditions for subsurface temperatures by the online DA, even every 100 years, has explicit effects on the performance of the model. This is due to having a wide observation network of subsurface temperatures and due to the fact that temperatures in deeper layers have a longer memory (their effects attenuate slowly during the time) than the surface temperature.
- Assimilation of subsurface temperatures changes the precipitation and consequently FW flux, AMOC, and SST. DA influences the timing of climate events. Therefore, the online DA, introduced in this study, can be useful in adjusting the model to replicate the climate events during the last deglaciation if a suitable observation network assimilates into the model.
- In agreement with Chapter 4 and Chapter 5, this part showed that the ice sheet reconstruction is the main uncertainty in the last deglaciation simulations. Modifying the ice sheet reconstruction can be used as a tuning factor to capture the BA/YD sequence at the right time with meaningful magnitudes.

## 7.2 Outlook

Simulations with prescribed ice sheets cannot resemble the full dynamics of the termination as in such simulations, the deglacial FW flux acts as a forcing rather than a response to AMOC changes (Lohmann and Schulz, 2000). As a logical next step, transient simulation of the last deglaciation with fully interactive ice sheets will explore the climate and biogeochemical feedback in the system. In addition, single forcing experiments are deemed to be important in evaluating the phase-space and instabilities in the system.

The DA approach introduced in this work is not restricted to the specific application of the deglacial climate presented in this dissertation. CLIMBER-X and PDAF or

their variations can also be applied to other data sets and scientific questions for long-term variations in the past. There are several future steps that can improve the DA technique implemented in this study. For example, since the FW forcing plays a significant role in the transient simulation of the past, it is worth making the model stochastic by adding precipitation randomness to the model instead of temperature or adding both temperature and precipitation randomness. Given that the stochastic version of the CLIMBER-X and the deterministic CLIMBER-X differ in the simulation of the last deglaciation, another logical technical step is to make perturbations based on the output of simulations conducted by CLIMBER-X or other models instead of TraCE-21000 project (He, 2011) to understand better the effect of the origin of the perturbations on the performance of the stochastic model. Furthermore, this study showed that the assimilation of only real surface temperature every 100 years does not cause any meaningful impact on the model performance for simulating other climate variables; however, assimilating ideal subsurface temperatures influences the model performance even with the long gap between DA incidents. Therefore, another logical step is to conduct DA experiments with shorter DA cycles to update the initial condition more frequently. Finally, the DA technique in this study can be used to simulate future scenarios. For example, one can design a future simulation forced by GHGs concentrations and orbital forcing and assimilate the subsurface temperatures into the model to have a weak ocean circulation to investigate the stability of glaciers and the FW budget of the North Atlantic. Max et al. (2022) suggest that weak ocean circulation in the future could expedite warming within the subpolar Atlantic's interior ocean. This accelerated warming might significantly impact the stability of contemporary marine-terminating Arctic glaciers and alter the freshwater balance in the North Atlantic.

# Appendix A

# Simulations of the Last Deglaciation

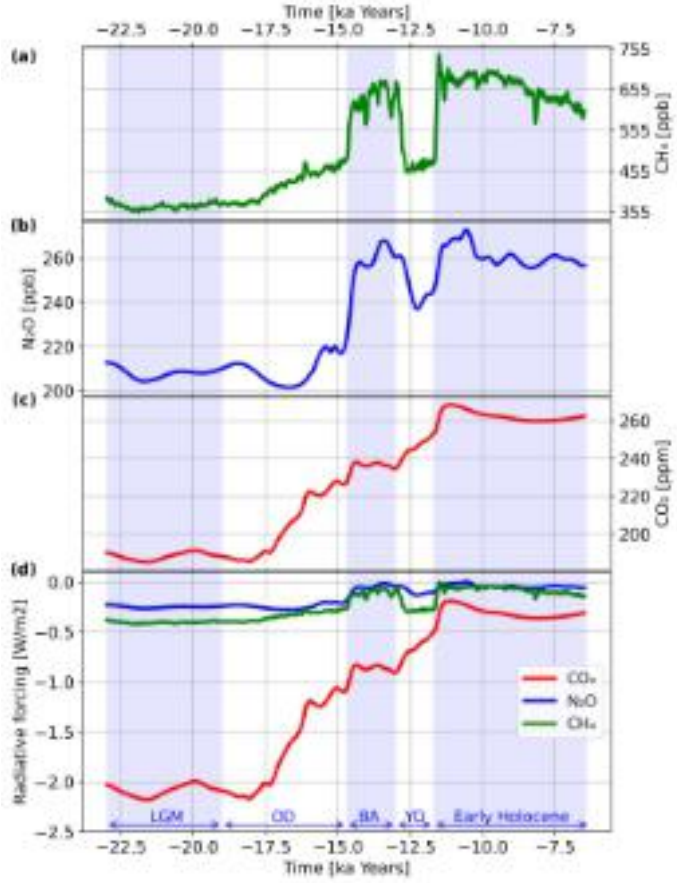


Figure A.1: Concentration evolution of $CH_4$ (a), $N_2O$ (b), and $CO_2$ (c). Radiative forcing derived from the concentration of $CH_4$ (a), $N_2O$ (b), and $CO_2$ (d). Data is provided by Köhler et al. (2017).

Table A.1: Simulations which are conducted in Chapter 4. Ice-sheet reconstructions, GLAC1D and PaleoMist, include topography, bathymetry, and land-sea distribution.

| **Exp. GLAC1D** | **Exp. PaleoMist** | **Transient Forcing** | **Constant Forcing** | **FW Forcing** |
|---|---|---|---|---|
| GLAC1D_full | PaleoMist_full | Ice-sheet reconstruction, GHG, Orbital | - | Melted ice-sheet, Precipitation-evaporation, Sea ice fluxes, Land runoff |
| GLAC1D_fixIce | PaleoMist_fixIce | GHG, Orbital | LGM ice-sheet reconstruction | Precipitation-evaporation, Sea ice fluxes, Land runoff |
| GLAC1D_fixGHG | PaleoMist_fixGHG | Ice-sheet reconstruction, Orbital | LGM GHGs | Melted ice-sheet, Precipitation-evaporation, Sea ice fluxes, Land runoff |
| GLAC1D_fixOrbit | PaleoMist_fixOrbit | Ice-sheet reconstruction, GHG | LGM Orbit | Melted ice-sheet, Precipitation-evaporation, Sea ice fluxes, Land runoff |
| GLAC1D_PI | PaleoMist_PI | - | PI Ice-sheet reconstruction, GHG, and orbital | Melted ice-sheet, Precipitation-evaporation, Sea ice fluxes, Land runoff |

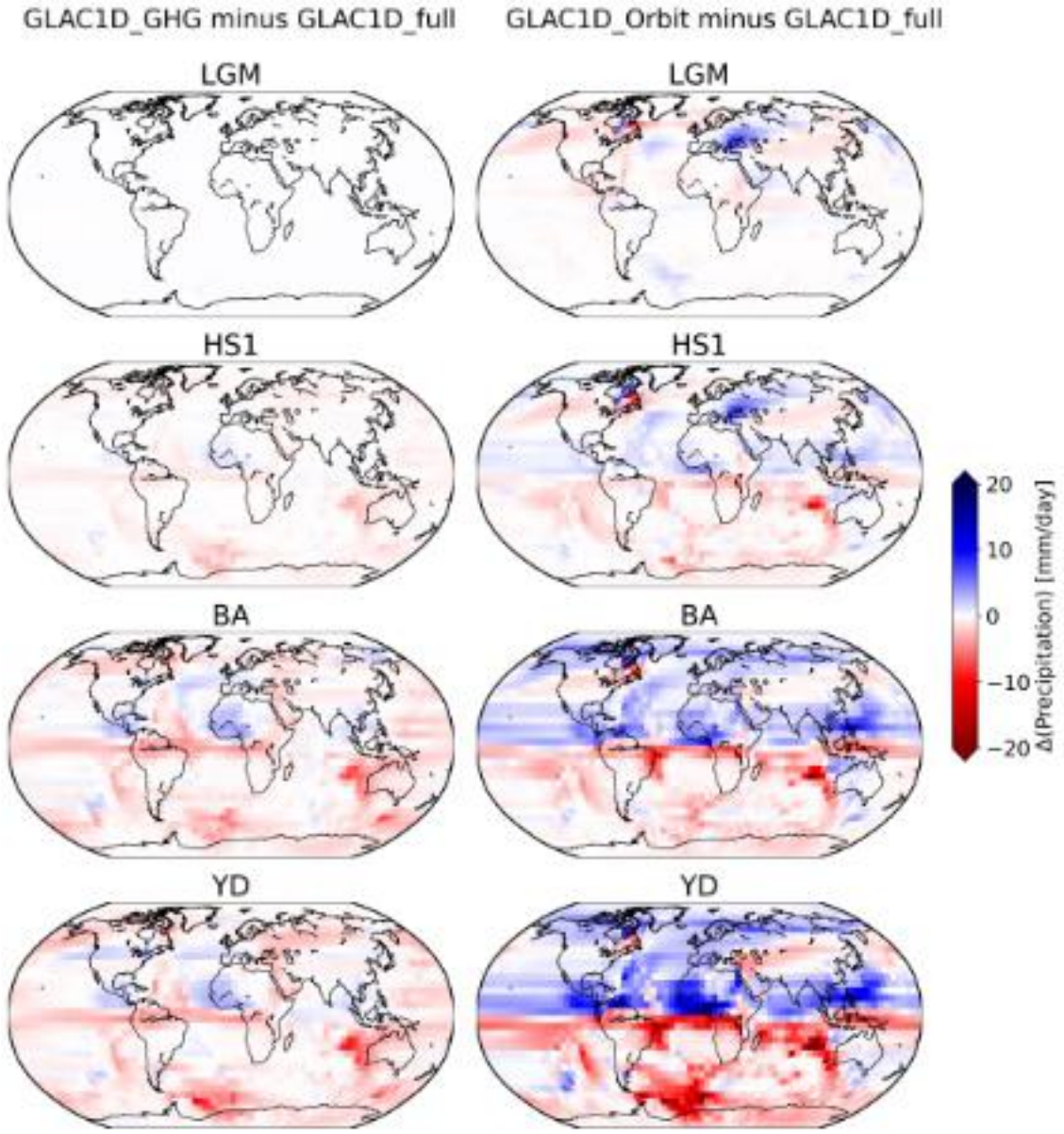


Figure A.2: Precipitation differences between GLAC1D_full and GLAC1D_fixGHG(left), GLAC1D_full and GLAC1D_fixOrbit (right) for LGM, HS1, BA, and YD.

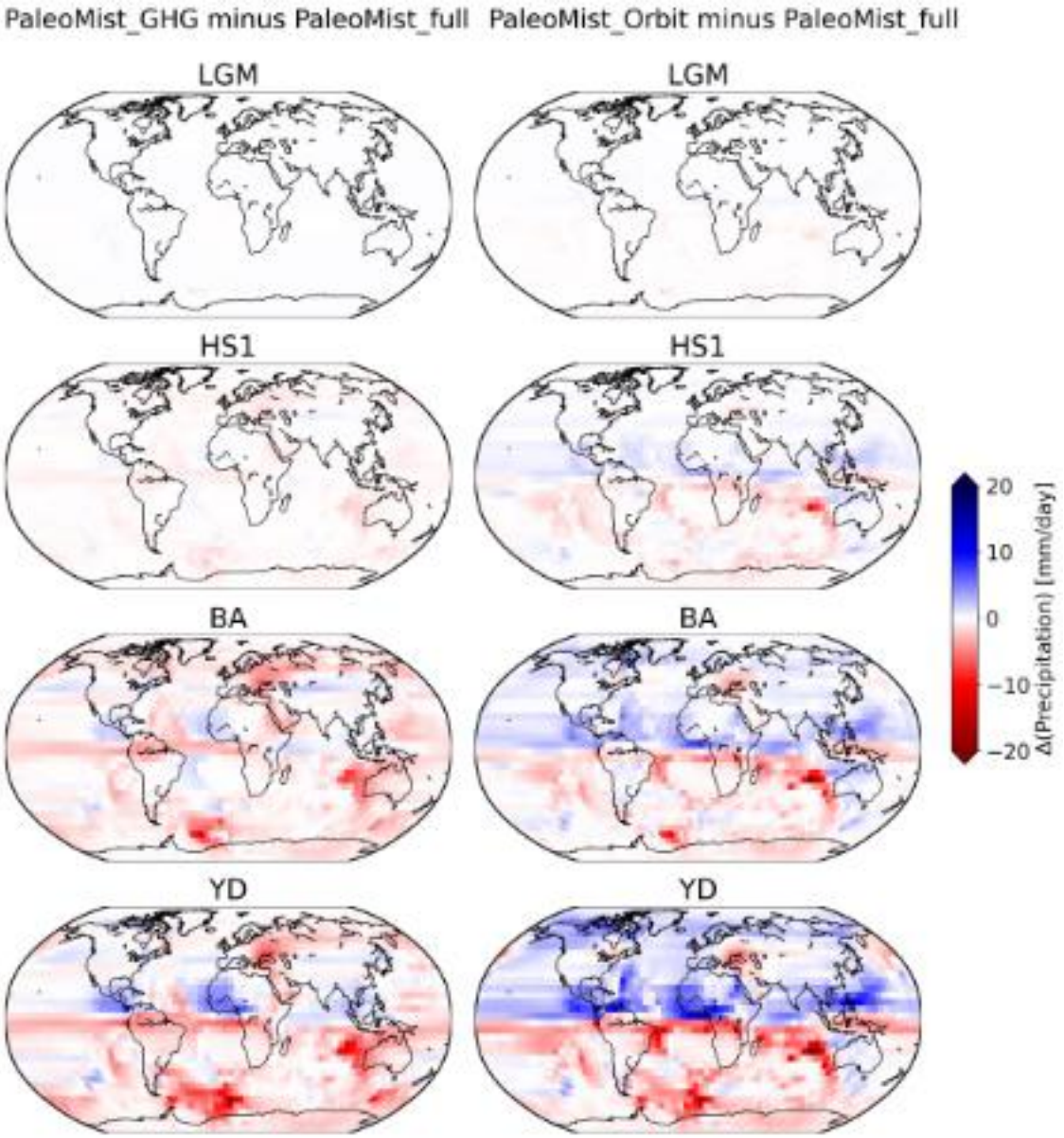


Figure A.3: Precipitation differences between PaleoMist_full and PaleoMist_fixGHG(left), PaleoMist_full and PaleoMist_fixOrbit (right) for LGM, HS1, BA, and YD.

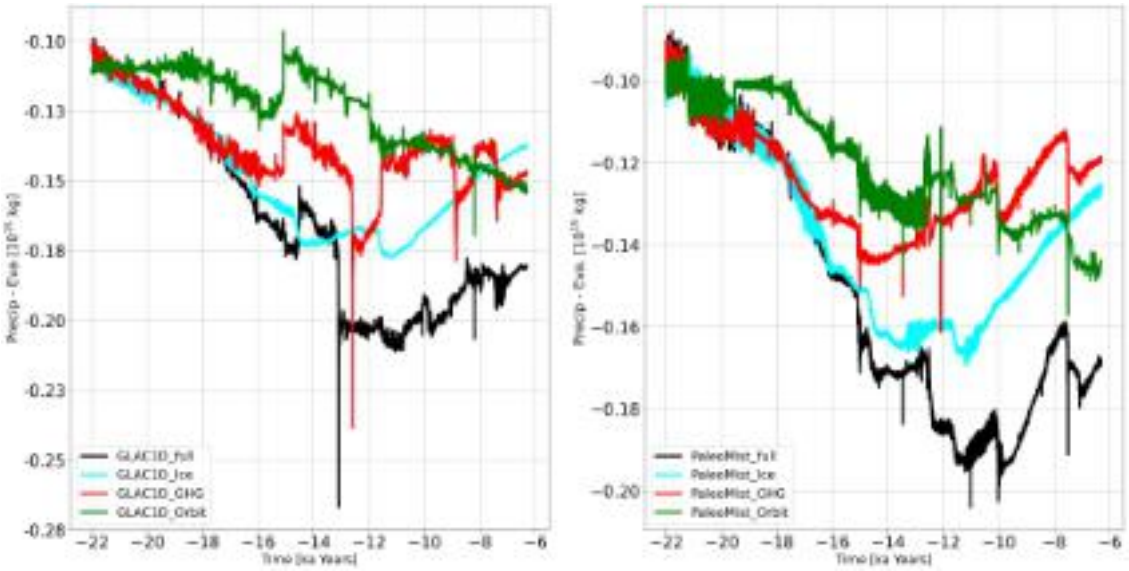


Figure A.4: Global precipitation minus evaporation for Exp_GLAC1D (left) and Exp_PaleoMist (right) during the last deglaciation.

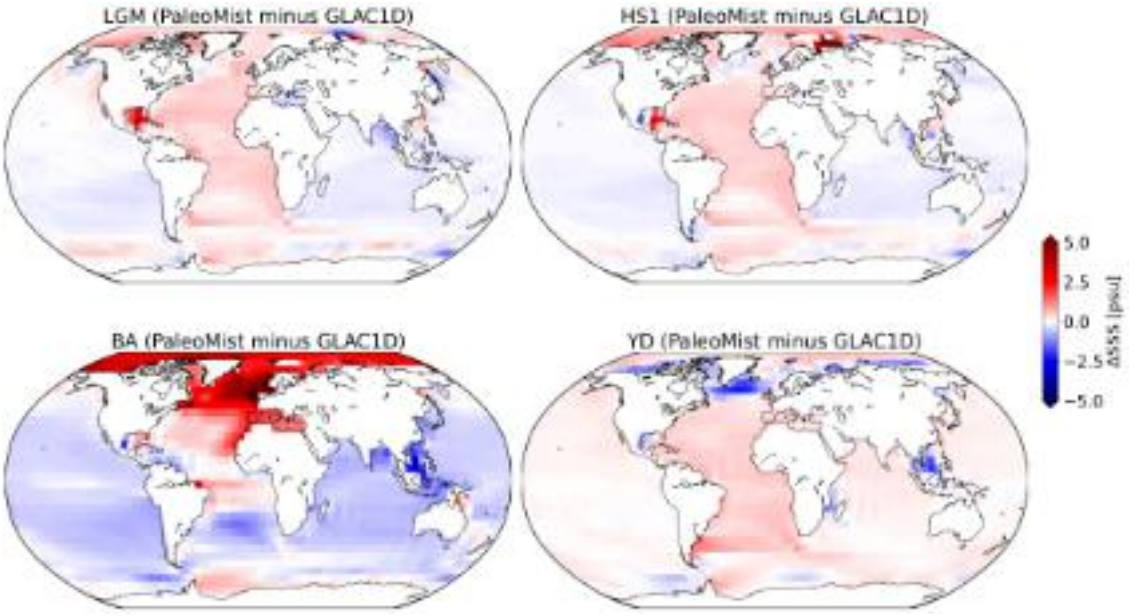


Figure A.5: Sea surface salinity differences between GLAC1D_full and PaleoMist_full for different periods of the last deglaciation.

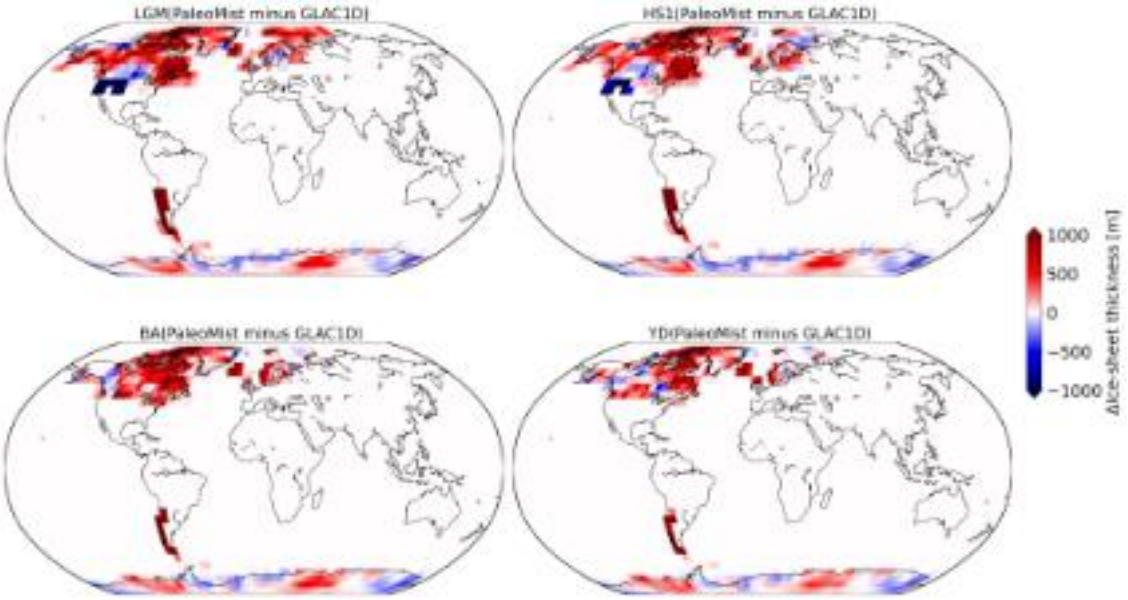


Figure A.6: Ice-thickness differences between GLAC1D and PaleoMist for different periods of the last deglaciation.

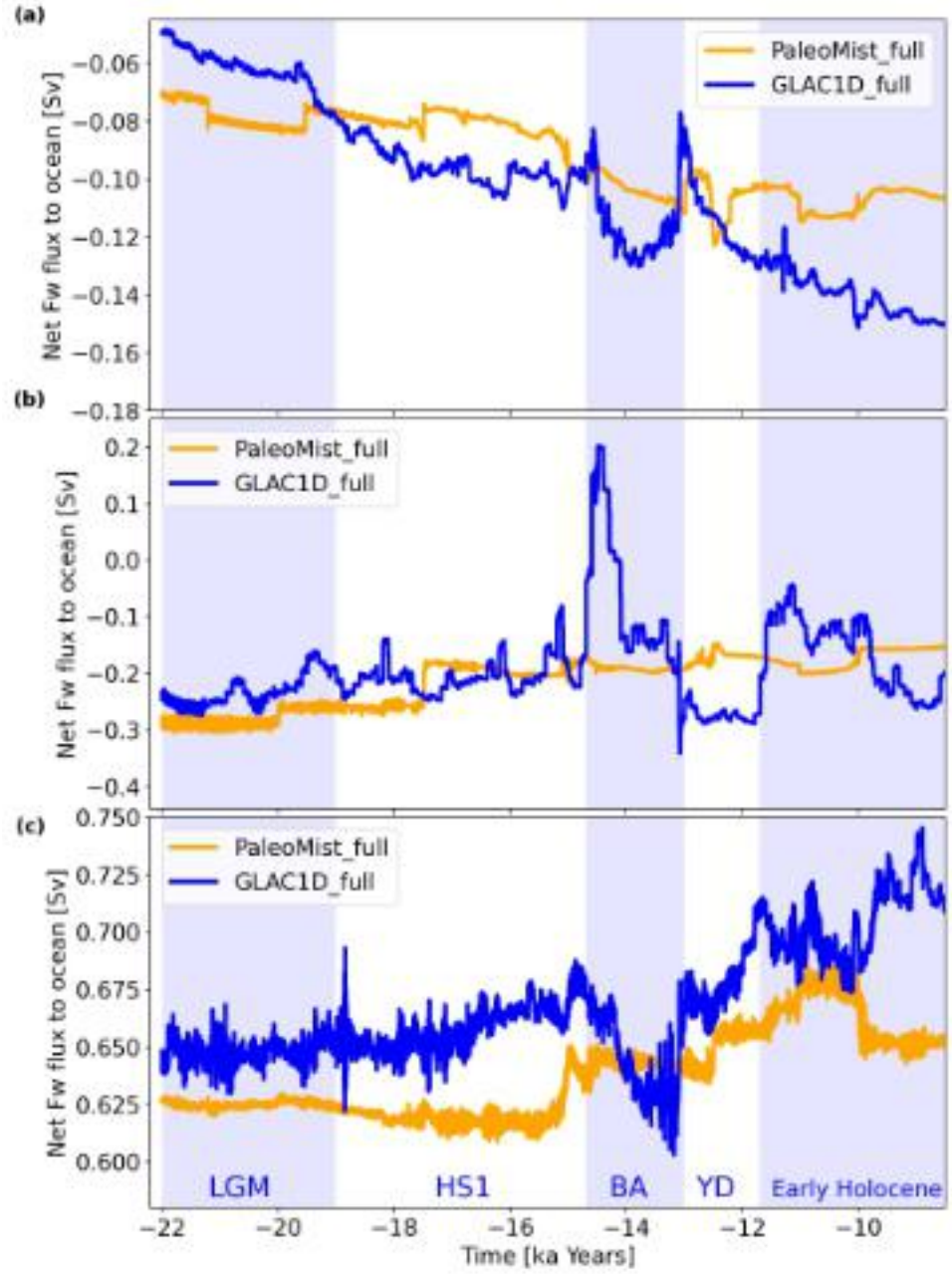


Figure A.7: FW flux into (a) the Pacific Ocean (north of 30°S), (b) Atlantic Ocean (north of 30°S), and (c) Southern Ocean for GLAC1D_full and PaleoMist_full. Units are Sv=106 $m^3/s$. The FW flux is the sum of precipitation minus evaporation, sea ice fluxes, land runoff, and deglacial melting of the ice sheets.

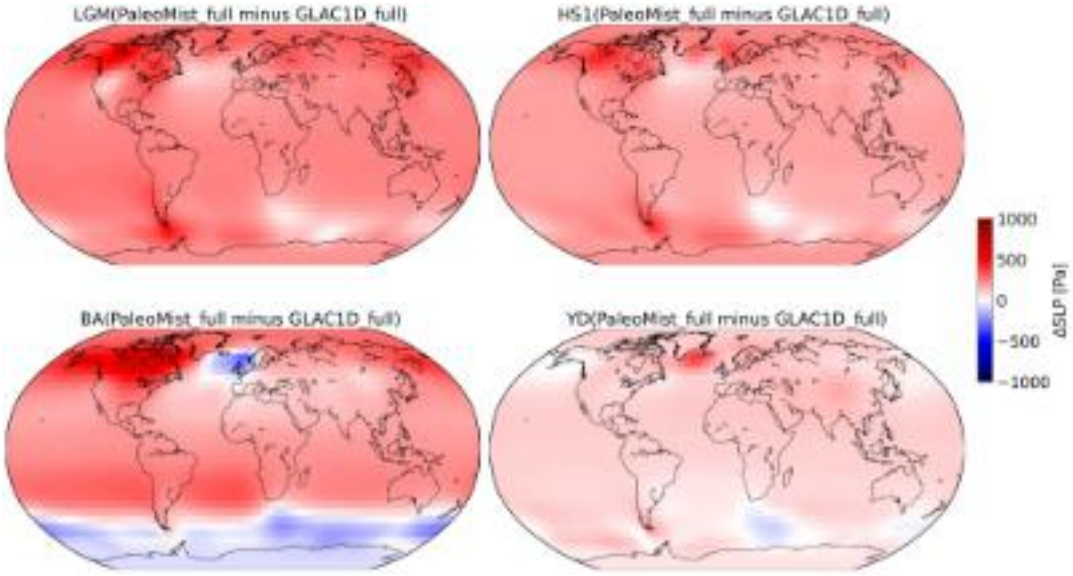


Figure A.8: Sea level pressure differences between GLAC1D_full and PaleoMist_full for LGM, HS1, BA, and YD.

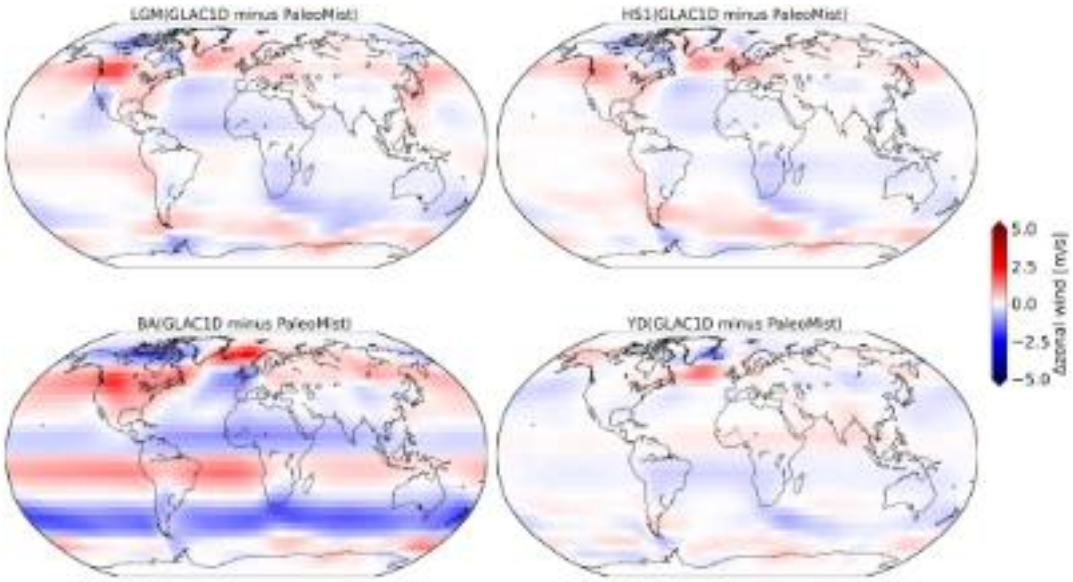


Figure A.9: Zonal wind differences between GLAC1D_full and PaleoMist_full for LGM, HS1, BA, and YD

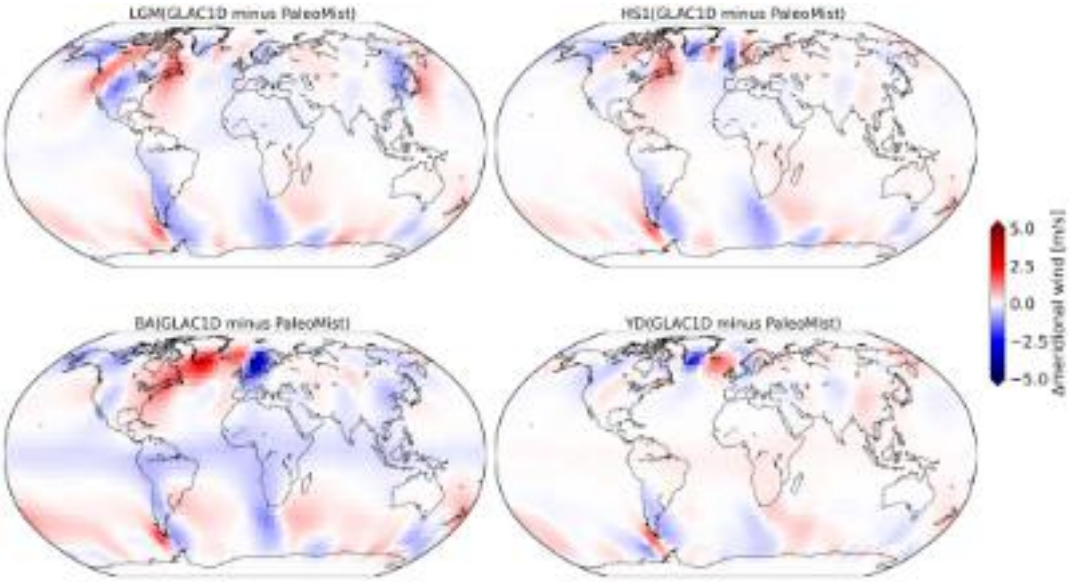


Figure A.10: Meridional wind differences between GLAC1D_full and PaleoMist_full for LGM, HS1, BA, and YD.

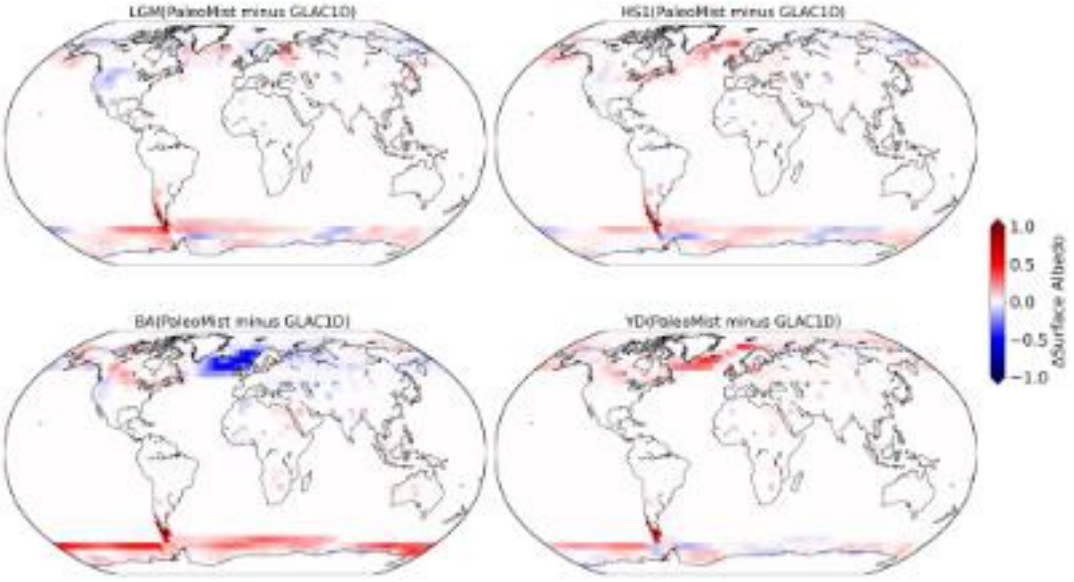


Figure A.11: Surface albedo differences between GLAC1D_full and PaleoMist_full for different periods of the last deglaciation.

# Appendix B

# Assimilation of subsurface Temperatures

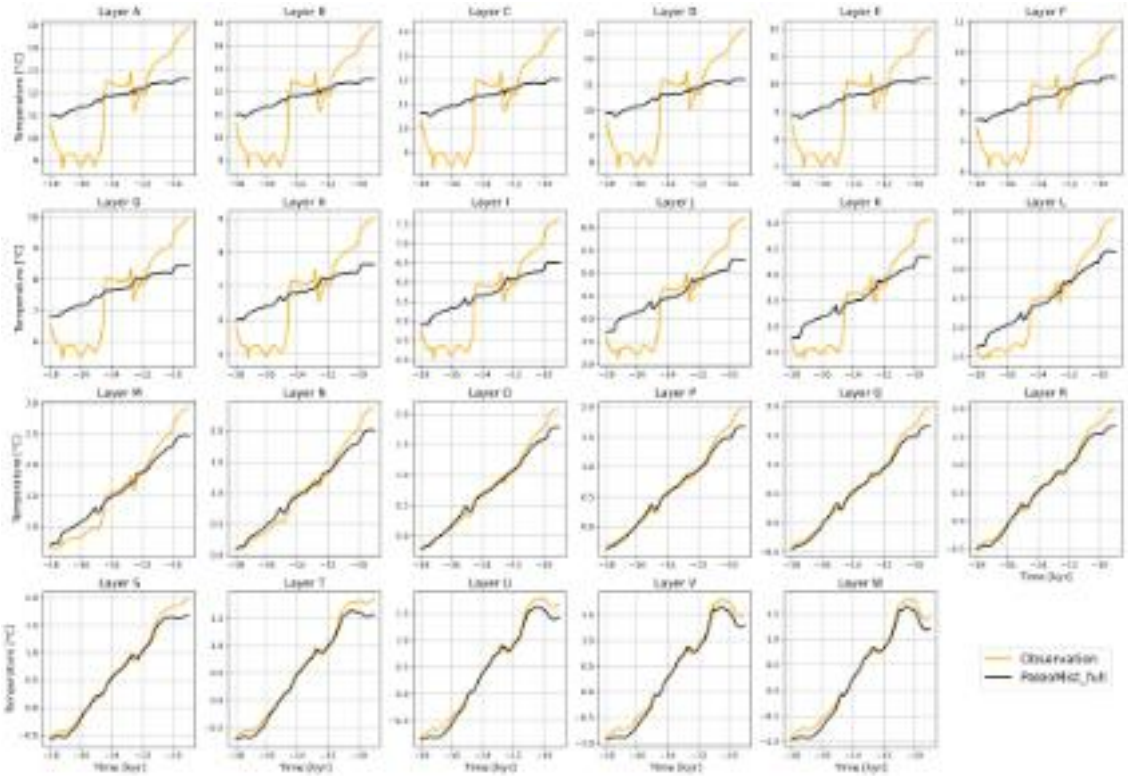

Figure B.1: Mean temperature for 23 layers of the ocean. Layer A is the surface layer (≈5 m), and Layer W is the deepest layer (≈5000 m). The layers have different depths. The orange is used as observation for DA, and black is the temperature for PaleoMist_full (Chapter 4)

.

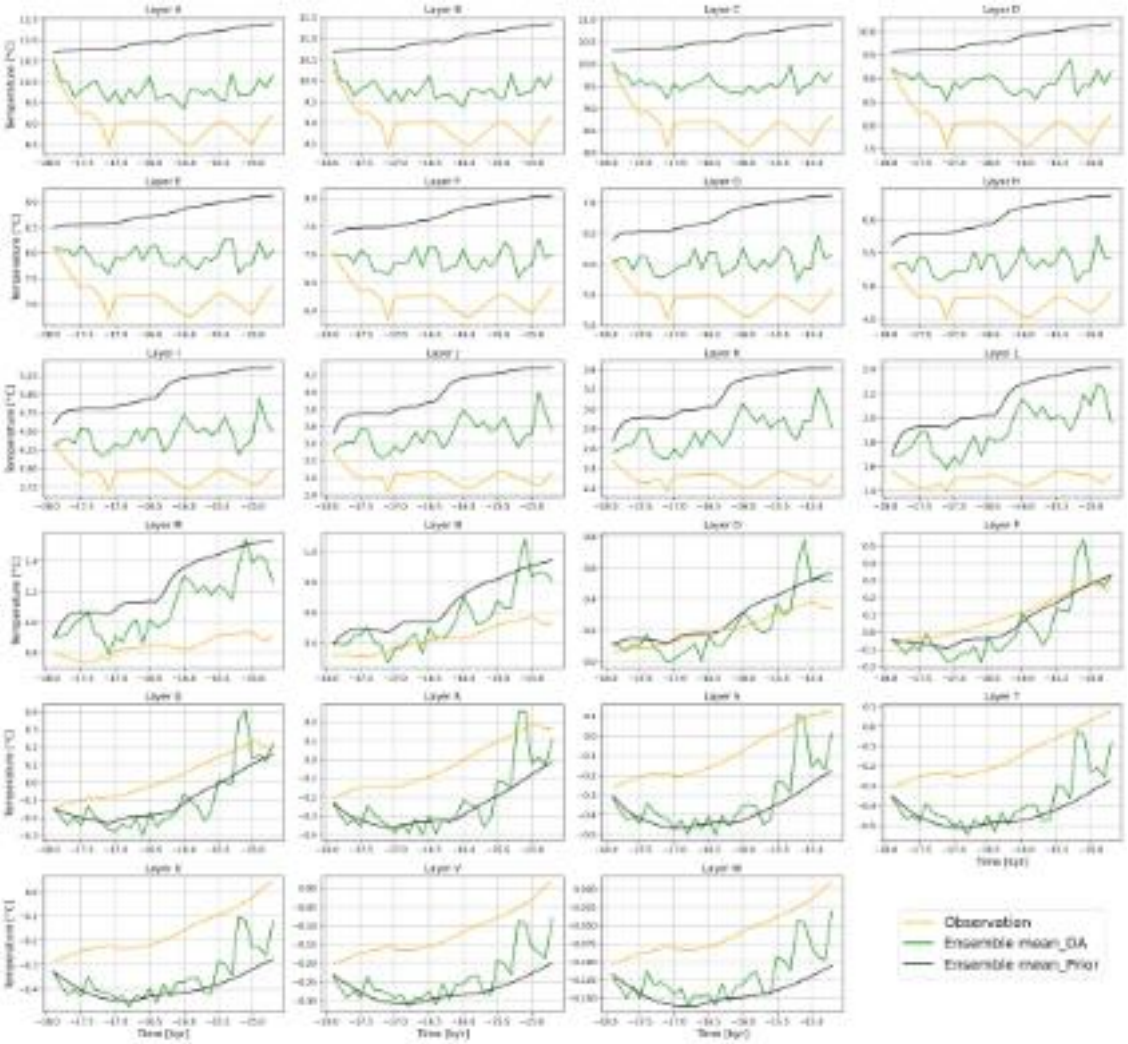


Figure B.2: Mean temperature for 23 layers of the ocean for DA experiment using PaleoMist_1000. Layer A is the surface layer (≈5 m), and Layer W is the deepest layer (≈5000 m). The layers have different depths. The orange, green, and black lines illustrate trajectories for observation, DA ensemble, and prior ensemble means, respectively.

# Bibliography


Abe-Ouchi, A., Saito, F., Kawamura, K., Raymo, M. E., Okuno, J., Takahashi, K., and Blatter, H. (2013). Insolation-driven 100,000-year glacial cycles and hysteresis of ice-sheet volume. *Nature*, 500(7461):190–193.

Abe-Ouchi, A., Segawa, T., and Saito, F. (2007). Climatic conditions for modelling the northern hemisphere ice sheets throughout the ice age cycle. *Climate of the Past*, 3(3):423–438.

Acevedo, W., Fallah, B., Reich, S., and Cubasch, U. (2017). Assimilation of pseudo-tree-ring-width observations into an atmospheric general circulation model. *Climate of the Past*, 13(5):545–557.

Alley, R. B. (2003). Palaeoclimatic insights into future climate challenges. *Philosophical Transactions of the Royal Society of London. Series A: Mathematical, Physical and Engineering Sciences*, 361(1810):1831–1849.

Anderson, J. and Lei, L. (2013). Empirical localization of observation impact in ensemble kalman filters. *Monthly Weather Review*, 141:4140–4153.

Annan, J. and Hargreaves, J. (2012). Identification of climatic state with limited proxy data. *Climate of the Past*, 8(4):1141–1151.

Annan, J. D., Hargreaves, J. C., and Mauritsen, T. (2022). A new global surface temperature reconstruction for the last glacial maximum. *Climate of the Past*, 18(8):1883–1896.

Argus, D. F., Peltier, W., Drummond, R., and Moore, A. W. (2014). The antarctica component of postglacial rebound model ice-6g_c (vm5a) based on gps positioning, exposure age dating of ice thicknesses, and relative sea level histories. *Geophysical Journal International*, 198(1):537–563.

Arias, P., Bellouin, N., Coppola, E., Jones, R., Krinner, G., Marotzke, J., Naik, V., Palmer, M., Plattner, G.-K., Rogelj, J., et al. (2023). Intergovernmental panel on climate change (ipcc). technical summary. In *Climate Change 2021: The Physical Science Basis. Contribution of Working Group I to the Sixth Assessment Report of the Intergovernmental Panel on Climate Change*, pages 35–144. Cambridge University Press.

Ault, T., Deser, C., Newman, M., and Emile-Geay, J. (2013). Characterizing decadal to centennial variability in the equatorial pacific during the last millennium. *Geophysical Research Letters*, 40(13):3450–3456.

Ault, T. R., Cole, J. E., Overpeck, J. T., Pederson, G. T., and Meko, D. M. (2014). Assessing the risk of persistent drought using climate model simulations and paleoclimate data. *Journal of Climate*, 27(20):7529–7549.

Bakker, P., Rogozhina, I., Merkel, U., and Prange, M. (2020). Hypersensitivity of glacial summer temperatures in siberia. *Climate of the Past*, 16(1):371–386.

Barkmeijer, J., Iversen, T., and Palmer, T. (2003). Forcing singular vectors and other sensitive model structures. *Quarterly Journal of the Royal Meteorological Society*, 129:2401–2423.

Bell, A. R., Osgood, D. E., Cook, B. I., Anchukaitis, K. J., McCarney, G. R., Greene, A. M., Buckley, B. M., and Cook, E. R. (2013). Paleoclimate histories improve access and sustainability in index insurance programs. *Global environmental change*, 23(4):774–781.

Bethke, I., Li, C., and Nisancioglu, K. H. (2012). Can we use ice sheet reconstructions to constrain meltwater for deglacial simulations? *Paleoceanography*, 27(2).

Bhend, J., Franke, J., Folini, D., Wild, M., and Brönnimann, S. (2012). An ensemble-based approach to climate reconstructions. *Climate of the Past*, 8(3):963–976.

Blunier, T. and Brook, E. J. (2001). Timing of millennial-scale climate change in antarctica and greenland during the last glacial period. *science*, 291(5501):109–112.

Bonelli, S., Charbit, S., Kageyama, M., Woillez, M.-N., Ramstein, G., Dumas, C., and Quiquet, A. (2009). Investigating the evolution of major northern hemisphere ice sheets during the last glacial-interglacial cycle. *Climate of the Past*, 5(3):329–345.

Boucher, O. and Boucher, O. (2015). *Atmospheric aerosols*. Springer.

Bouttes, N., Lhardy, F., Quiquet, A., Paillard, D., Goosse, H., and Roche, D. M. (2023). Deglacial climate changes as forced by different ice sheet reconstructions. *Climate of the Past*, 19(5):1027–1042.

Bouttier, F. and Courtier, P. (1999). *Data Assimilation Concepts and Methods*. European Centre for Medium-Range Weather Forecasts (ECMWF), Shinfield Park.

Bouttier, F. and Courtier, P. (2002). Data assimilation concepts and methods march 1999. *Meteorological training course lecture series. ECMWF*, 718:59.

Box, G. E., Jenkins, G. M., Reinsel, G. C., and Ljung, G. M. (2015). *Time series analysis: forecasting and control*. John Wiley & Sons.

Brady, E., Stevenson, S., Bailey, D., Liu, Z., Noone, D., Nusbaumer, J., Otto-Bliesner, B., Tabor, C., Tomas, R., Wong, T., et al. (2019). The connected isotopic water cycle in the community earth system model version 1. *Journal of Advances in Modeling Earth Systems*, 11(8):2547–2566.

Breitenmoser, P., Brönnimann, S., and Frank, D. (2014). Forward modelling of tree-ring width and comparison with a global network of tree-ring chronologies. *Climate of the Past*, 10:437–449.

Briggs, R. D., Pollard, D., and Tarasov, L. (2014). A data-constrained large ensemble analysis of antarctic evolution since the eemian. *Quaternary Science Reviews*, 103:91–115.

Broecker, W. S. (2002). *The glacial world according to Wally.* International series of monographs on physics. Lamont-Doherty earth observatory of Columbia University.

Buizert, C., Gkinis, V., Severinghaus, J. P., He, F., Lecavalier, B. S., Kindler, P., Leuenberger, M., Carlson, A. E., Vinther, B., Masson-Delmotte, V., et al. (2014). Greenland temperature response to climate forcing during the last deglaciation. *Science*, 345(6201):1177–1180.

Burke, K. D., Williams, J. W., Chandler, M. A., Haywood, A. M., Lunt, D. J., and Otto-Bliesner, B. L. (2018). Pliocene and eocene provide best analogs for near-future climates. *Proceedings of the National Academy of Sciences*, 115(52):13288–13293.

Butzin, M., Köhler, P., and Lohmann, G. (2017). Marine radiocarbon reservoir age simulations for the past 50,000 years. *Geophysical Research Letters*, 44(16):8473–8480.

Caillon, N., Severinghaus, J. P., Jouzel, J., Barnola, J.-M., Kang, J., and Lipenkov, V. Y. (2003). Timing of atmospheric co2 and antarctic temperature changes across termination iii. *Science*, 299(5613):1728–1731.

Cane, M. A., Braconnot, P., Clement, A., Gildor, H., Joussaume, S., Kageyama, M., Khodri, M., Paillard, D., Tett, S., and Zorita, E. (2006). Progress in paleoclimate modeling. *Journal of Climate*, 19(20):5031–5057.

Carlson, A. E., Clark, P. U., Haley, B. A., Klinkhammer, G. P., Simmons, K., Brook, E. J., and Meissner, K. J. (2007). Geochemical proxies of north american freshwater routing during the younger dryas cold event. *Proceedings of the National Academy of Sciences*, 104(16):6556–6561.

Carlson, A. E., Ullman, D. J., Anslow, F. S., He, F., Clark, P. U., Liu, Z., and Otto-Bliesner, B. L. (2012). Modeling the surface mass-balance response of the laurentide ice sheet to bølling warming and its contribution to meltwater pulse 1a. *Earth and Planetary Science Letters*, 315:24–29.

Change, I. P. O. C. (2007). Climate change 2007: The physical science basis. *Agenda*, 6(07):333.

Charbit, S., Kageyama, M., Roche, D., Ritz, C., and Ramstein, G. (2005). Investigating the mechanisms leading to the deglaciation of past continental northern hemisphere ice sheets with the climber–gremlins coupled model. *Global and Planetary Change*, 48(4):253–273.

Cheng, H., Edwards, R. L., Broecker, W. S., Denton, G. H., Kong, X., Wang, Y., Zhang, R., and Wang, X. (2009). Ice age terminations. *science*, 326(5950):248–252.

Chikamoto, Y., Kimoto, M., Ishii, M., Mochizuki, T., Sakamoto, T. T., Tatebe, H., Komuro, Y., Watanabe, M., Nozawa, T., Shiogama, H., et al. (2013). An overview of decadal climate predictability in a multi-model ensemble by climate model miroc. *Climate Dynamics*, 40:1201–1222.

Chou, J. (1983). Some properties of operators and the effect of initial condition. *Acta Meteorologica Sinica*, 41:385–392. in Chinese with English abstract.

Clark, P. U., Pisias, N. G., Stocker, T. F., and Weaver, A. J. (2002). The role of the thermohaline circulation in abrupt climate change. *Nature*, 415(6874):863–869.

Clark, P. U., Shakun, J. D., Baker, P. A., Bartlein, P. J., Brewer, S., Brook, E., Carlson, A. E., Cheng, H., Kaufman, D. S., Liu, Z., et al. (2012). Global climate evolution during the last deglaciation. *Proceedings of the National Academy of Sciences*, 109(19):E1134–E1142.

Clark, P. U. and Tarasov, L. (2014). Closing the sea level budget at the last glacial maximum. *Proceedings of the National Academy of Sciences*, 111(45):15861–15862.

Claussen, M., Mysak, L., Weaver, A., Crucifix, M., Fichefet, T., Loutre, M.-F., Weber, S., Alcamo, J., Alexeev, V., Berger, A., et al. (2002). Earth system models of intermediate complexity: closing the gap in the spectrum of climate system models. *Climate dynamics*, 18:579–586.

Coats, S., Smerdon, J., Stevenson, S., Fasullo, J., Otto-Bliesner, B., and Ault, T. (2020). Paleoclimate constraints on the spatiotemporal character of past and future droughts. *Journal of Climate*, 33(22):9883–9903.

Collins, M. (2002). Climate predictability on interannual to decadal time scales: The initial value problem. *Climate dynamics*, 19:671–692.

community, E. (2004). Eight glacial cycles from an antarctic ice core. *Nature*, 429(6992):623–628.

Compo, G., Whitaker, J., Sardeshmukh, P., Matsui, N., Allan, R., and Yin, X. (2011). The twentieth century reanalysis project. *Quarterly Journal of the Royal Meteorological Society*, 137:1–28.

Consortium, P. et al. (2017). A global multiproxy database for temperature reconstructions of the common era. *Scientific data*, 4.

Cook, B. I., Cook, E. R., Anchukaitis, K. J., Seager, R., and Miller, R. L. (2011). Forced and unforced variability of twentieth century north american droughts and pluvials. *Climate dynamics*, 37:1097–1110.

Crespin, E., Goosse, H., Fichefet, T., and Mann, M. (2009). The 15th century arctic warming in coupled model simulations with data assimilation. *Climate of the Past*, 5:389–401.

Crowley, T. J. (1991). Utilization of paleoclimate results to validate projections of a future greenhouse warming. In *Developments in atmospheric science*, volume 19, pages 35–45. Elsevier.

Crowley, T. J. (2000). Causes of climate change over the past 1000 years. *Science*, 289(5477):270–277.

Dang, C., Brandt, R. E., and Warren, S. G. (2015). Parameterizations for narrowband and broadband albedo of pure snow and snow containing mineral dust and black carbon. *Journal of Geophysical Research: Atmospheres*, 120(11):5446–5468.

Dee, D. P. (2005). Bias and data assimilation. *Quarterly Journal of the Royal Meteorological Society: A journal of the atmospheric sciences, applied meteorology and physical oceanography*, 131(613):3323–3343.

Dee, D. P. and Da Silva, A. M. (1998). Data assimilation in the presence of forecast bias. *Quarterly Journal of the Royal Meteorological Society*, 124(545):269–295.

Dee, S. G., Steiger, N. J., Emile-Geay, J., and Hakim, G. J. (2016). On the utility of proxy system models for estimating climate states over the common era. *Journal of Advances in Modeling Earth Systems*, 8(3):1164–1179.

Delworth, T. L., Zeng, F., Zhang, L., Zhang, R., Vecchi, G. A., and Yang, X. (2017). The central role of ocean dynamics in connecting the north atlantic oscillation to the extratropical component of the atlantic multidecadal oscillation. *Journal of Climate*, 30(10):3789–3805.

Deser, C., Alexander, M. A., Xie, S.-P., and Phillips, A. S. (2010). Sea surface temperature variability: Patterns and mechanisms. *Annual review of marine science*, 2:115–143.

Deser, C., Phillips, A., Bourdette, V., and Teng, H. (2012). Uncertainty in climate change projections: the role of internal variability. *Climate dynamics*, 38:527–546.

Ding, Z. L., Derbyshire, E., Yang, S., Yu, Z., Xiong, S., and Liu, T. (2002). Stacked 2.6-ma grain size record from the chinese loess based on five sections and correlation with the deep-sea $\delta$18o record. *Paleoceanography*, 17(3):5–1.

Dirren, S. and Hakim, G. J. (2005). Toward the assimilation of time-averaged observations. *Geophysical research letters*, 32(4).

Doblas-Reyes, F., Andreu-Burillo, I., Chikamoto, Y., García-Serrano, J., Guemas, V., Kimoto, M., Mochizuki, T., Rodrigues, L., and Van Oldenborgh, G. (2013). Initialized near-term regional climate change prediction. *Nature communications*, 4(1):1715.

Dubinkina, S., Goosse, H., Sallaz-Damaz, Y., Crespin, E., and Crucifix, M. (2011). Testing a particle filter to reconstruct climate changes over the past centuries. *International Journal of Bifurcation and Chaos*, 21:3611–3618.

Edwards, N. R., Willmott, A. J., and Killworth, P. D. (1998). On the role of topography and wind stress on the stability of the thermohaline circulation. *Journal of physical oceanography*, 28(5):756–778.

Edwards, T., Annan, J., Crucifix, M., Gebbie, G., and Paul, A. (2013). Best-of-both-worlds estimates for time slices in the past. *Pages News Letter*, 21:76–77.

Elderfield, H., Greaves, M., Barker, S., Hall, I. R., Tripati, A., Ferretti, P., Crowhurst, S., Booth, L., and Daunt, C. (2010). A record of bottom water temperature and seawater $\delta$18o for the southern ocean over the past 440 kyr based on mg/ca of benthic foraminiferal uvigerina spp. *Quaternary Science Reviews*, 29(1-2):160–169.

Erb, M. P., McKay, N. P., Steiger, N., Dee, S., Hancock, C., Ivanovic, R. F., Gregoire, L. J., and Valdes, P. (2022). Reconstructing holocene temperatures in time and space using paleoclimate data assimilation. *Climate of the Past*, 18(12):2599–2629.

Evensen, G. (2003). The ensemble kalman filter: Theoretical formulation and practical implementation. *Ocean dynamics*, 53(4):343–367.

Fang, M. and Li, X. (2016). Paleoclimate data assimilation: Its motivation, progress and prospects. *Science China Earth Sciences*, 59:1817–1826.

Fang, S.-w., Khodri, M., Timmreck, C., Zanchettin, D., and Jungclaus, J. (2021). Disentangling internal and external contributions to atlantic multidecadal variability over the past millennium. *Geophysical Research Letters*, 48(23):e2021GL095990.

Feigelson, M., Ginzburg, S., Krasnokutskaya, D., and Petoukhov, K. (1975). Effects of clouds on the radiative heat exchange in the atmosphere. *Geofísica Internacional*, 15(4):293–326.

Fernández-Donado, L., González-Rouco, J., Raible, C., Ammann, C., Barriopedro, D., García-Bustamante, E., Jungclaus, J. H., Lorenz, S., Luterbacher, J., Phipps, S. J., et al. (2013). Large-scale temperature response to external forcing in simulations and reconstructions of the last millennium. *Climate of the Past*, 9(1):393–421.

Fischer, H., Wahlen, M., Smith, J., Mastroianni, D., and Deck, B. (1999). Ice core records of atmospheric co2 around the last three glacial terminations. *Science*, 283(5408):1712–1714.

Fischer, M. (2006). ichasm, a flexible land-surface model that incorporates stable water isotopes. *Global and Planetary Change*, 51:121–130.

Flato, G., Marotzke, J., Abiodun, B., Braconnot, P., Chou, S. C., Collins, W., Cox, P., Driouech, F., Emori, S., Eyring, V., et al. (2014). Evaluation of climate models. In *Climate change 2013: the physical science basis. Contribution of Working Group I to the Fifth Assessment Report of the Intergovernmental Panel on Climate Change*, pages 741–866. Cambridge University Press.

Franke, J., Brönnimann, S., Bhend, J., and Brugnara, Y. (2017). A monthly global paleo-reanalysis of the atmosphere from 1600 to 2005 for studying past climatic variations. *Scientific data*, 4(1):1–19.

Franke, J., Valler, V., Brönnimann, S., Neukom, R., and Jaume-Santero, F. (2020). The importance of input data quality and quantity in climate field reconstructions–results from the assimilation of various tree-ring collections. *Climate of the Past*, 16(3):1061–1074.

Ganopolski, A. and Brovkin, V. (2017). Simulation of climate, ice sheets and co 2 evolution during the last four glacial cycles with an earth system model of intermediate complexity. *Climate of the Past*, 13(12):1695–1716.

Ganopolski, A. and Calov, R. (2011). The role of orbital forcing, carbon dioxide and regolith in 100 kyr glacial cycles. *Climate of the Past*, 7(4):1415–1425.

Ganopolski, A., Calov, R., and Claussen, M. (2010). Simulation of the last glacial cycle with a coupled climate ice-sheet model of intermediate complexity. *Climate of the Past*, 6(2):229–244.

Ganopolski, A. and Roche, D. M. (2009). On the nature of lead–lag relationships during glacial–interglacial climate transitions. *Quaternary Science Reviews*, 28(27-28):3361–3378.

Gaspari, G. and Cohn, S. E. (1999). Construction of correlation functions in two and three dimensions. *Quarterly Journal of the Royal Meteorological Society*, 125(554):723–757.

Gleick, P. H. (1993). *Water in crisis*, volume 100. New York: Oxford University Press.

Gong, X., Lembke-Jene, L., Lohmann, G., Knorr, G., Tiedemann, R., Zou, J., and Shi, X. (2019). Enhanced north pacific deep-ocean stratification by stronger intermediate water formation during heinrich stadial 1. *Nature communications*, 10(1):656.

Goosse, H. (2015). Continental-scale temperature variability in pmip3 simulations and pages 2k regional temperature reconstructions over the past millennium. *Climate of the Past*, 11(12).

Goosse, H., Crespin, E., de Montety, A., Mann, M., Renssen, H., and Timmermann, A. (2010). Reconstructing surface temperature changes over the past 600 years using climate model simulations with data assimilation. *Journal of Geophysical Research: Atmospheres*, 115(D9).

Goosse, H., Crespin, E., Dubinkina, S., Loutre, M.-F., Mann, M. E., Renssen, H., Sallaz-Damaz, Y., and Shindell, D. (2012a). The role of forcing and internal dynamics in explaining the "medieval climate anomaly". *Climate dynamics*, 39(12):2847–2866.

Goosse, H., Guiot, J., Mann, M. E., Dubinkina, S., and Sallaz-Damaz, Y. (2012b). The medieval climate anomaly in europe: Comparison of the summer and annual mean signals in two reconstructions and in simulations with data assimilation. *Global and Planetary Change*, 84:35–47.

Goosse, H., Renssen, H., Timmermann, A., Bradley, R., and Mann, M. (2006a). Using paleoclimate proxy-data to select optimal realizations in an ensemble of simulations of the climate of the past millennium. *Climate Dynamics*, 27:165–184.

Gordon, N., Salmond, D., and Smith, A. (1993). Novel approach to nonlinear/non-gaussian bayesian state estimation. *IEE Proceedings F (Radar and Signal Processing)*, 140:107–113.

Gowan, E. J., Tregoning, P., Purcell, A., Lea, J., Fransner, O. J., Noormets, R., and Dowdeswell, J. (2016). Icesheet 1.0: a program to produce paleo-ice sheet reconstructions with minimal assumptions. *Geoscientific Model Development*, 9(5):1673–1682.

Gowan, E. J., Zhang, X., Khosravi, S., Rovere, A., Stocchi, P., Hughes, A. L., Gyllencreutz, R., Mangerud, J., Svendsen, J.-I., and Lohmann, G. (2021). A new global ice sheet reconstruction for the past 80 000 years. *Nature communications*, 12(1):1–9.

Gowan, E. J., Zhang, X., Khosravi, S., Rovere, A., Stocchi, P., Hughes, A. L., Gyllencreutz, R., Mangerud, J., Svendsen, J.-I., and Lohmann, G. (2022). Reply to: Towards solving the missing ice problem and the importance of rigorous model data comparisons. *Nature Communications*, 13(1):6264.

Gregoire, L. J., Valdes, P. J., and Payne, A. J. (2015). The relative contribution of orbital forcing and greenhouse gases to the north american deglaciation. *Geophysical Research Letters*, 42(22):9970–9979.

Gulev, S. K., Thorne, P. W., Ahn, J., Dentener, F. J., Domingues, C. M., Gerland, S., Gong, D., Kaufman, D. S., Nnamchi, H. C., Quaas, J., et al. (2021). Changing state of the climate system.

Hakim, G. J., Annan, J., Bronnimann, S., Crucifix, M., Edwards, T., Goosse, H., Paul, A., van der Schrier, G., and Widmann, M. (2013). Overview of data assimilation methods. *PAGES News*, 21:72–73.

Hakim, G. J., Emile-Geay, J., Steig, E. J., Noone, D., Anderson, D. M., Tardif, R., Steiger, N., and Perkins, W. A. (2016). The last millennium climate reanalysis project: Framework and first results. *Journal of Geophysical Research: Atmospheres*, 121(12):6745–6764.

Han, X. J., Li, X., Rigon, R., Jin, R., and Endrizzi, S. (2015). Soil moisture estimation by assimilating l-band microwave brightness temperature with geostatistics and observation localization. *PLOS One*, 10:e0116435.

Hansen, J., Russell, G., Rind, D., Stone, P., Lacis, A., Lebedeff, S., Ruedy, R., and Travis, L. (1983). Efficient three-dimensional global models for climate studies: Models i and ii. *Monthly Weather Review*, 111(4):609–662.

Hargreaves, J., Abe-Ouchi, A., and Annan, J. (2007). Linking glacial and future climates through an ensemble of gcm simulations. *Climate of the Past*, 3(1):77–87.

Hargreaves, J. and Annan, J. (2002). Assimilation of paleo-data in a simple earth system model. *Climate Dynamics*, 19:371–381.

Hargreaves, J. and Annan, J. (2009). On the importance of paleoclimate modelling for improving predictions of future climate change. *Climate of the Past*, 5(4):803–814.

Haskins, R. K., Oliver, K. I., Jackson, L. C., Wood, R. A., and Drijfhout, S. S. (2020). Temperature domination of amoc weakening due to freshwater hosing in two gcms. *Climate dynamics*, 54:273–286.

Hasselmann, K. (1976). Stochastic climate models part i. theory. *tellus*, 28(6):473–485.

Hays, J. D., Imbrie, J., and Shackleton, N. J. (1976). Variations in the earth's orbit: Pacemaker of the ice ages: For 500,000 years, major climatic changes have followed variations in obliquity and precession. *science*, 194(4270):1121–1132.

He, F. (2011). *Simulating transient climate evolution of the last deglaciation with CCSM 3*, volume 72.

He, F. and Clark, P. U. (2022). Freshwater forcing of the atlantic meridional overturning circulation revisited. *Nature Climate Change*, 12(5):449–454.

Heinemann, M., Timmermann, A., Elison Timm, O., Saito, F., and Abe-Ouchi, A. (2014). Deglacial ice sheet meltdown: Orbital pacemaking and co 2 effects. *Climate of the Past*, 10(4):1567–1579.

Held, H. and Kleinen, T. (2004). Detection of climate system bifurcations by degenerate fingerprinting. *Geophysical Research Letters*, 31(23).

Herbert, T. D., Peterson, L. C., Lawrence, K. T., and Liu, Z. (2010). Tropical ocean temperatures over the past 3.5 million years. *science*, 328(5985):1530–1534.

Herrington, A. R. and Poulsen, C. J. (2011). Terminating the last interglacial: The role of ice sheet–climate feedbacks in a gcm asynchronously coupled to an ice sheet model. *Journal of climate*, 25(6):1871–1882.

Hoke, J. E. and Anthes, R. A. (1976). The initialization of numerical models by a dynamic-initialization technique. *Monthly Weather Review*, 104:1551–1556.

Hoskins, B. J. and Karoly, D. J. (1981). The steady linear response of a spherical atmosphere to thermal and orographic forcing. *Journal of the atmospheric sciences*, 38(6):1179–1196.

Houtekamer, P. L. and Mitchell, H. L. (2001). A sequential ensemble kalman filter for atmospheric data assimilation. *Monthly Weather Review*, 129:123–137.

Hunke, E. C. and Dukowicz, J. K. (1997). An elastic–viscous–plastic model for sea ice dynamics. *Journal of physical oceanography*, 27(9):1849–1867.

Huntley, H. S. and Hakim, G. J. (2010). Assimilation of time-averaged observations in a quasi-geostrophic atmospheric jet model. *Climate Dynamics*, 35:995–1009.

Hurrell, J. W., Holland, M. M., Gent, P. R., Ghan, S., Kay, J. E., Kushner, P. J., Lamarque, J.-F., Large, W. G., Lawrence, D., Lindsay, K., et al. (2013). The community earth system model: a framework for collaborative research. *Bulletin of the American Meteorological Society*, 94(9):1339–1360.

Huybers, P. (2011). Combined obliquity and precession pacing of late pleistocene deglaciations. *Nature*, 480(7376):229–232.

Ivanovic, R. F., Gregoire, L. J., Kageyama, M., Roche, D. M., Valdes, P. J., Burke, A., Drummond, R., Peltier, W. R., and Tarasov, L. (2016). Transient climate simulations of the deglaciation 21–9 thousand years before present (version 1)–pmip4 core experiment design and boundary conditions. *Geoscientific Model Development*, 9(7):2563–2587.

Jaccard, S., Galbraith, E., Sigman, D. M., and Haug, G. (2010). A pervasive link between antarctic ice core and subarctic pacific sediment records over the past 800 kyrs. *Quaternary Science Reviews*, 29(1-2):206–212.

Jungclaus, J. H., Lorenz, S., Timmreck, C., Reick, C., Brovkin, V., Six, K., Segschneider, J., Giorgetta, M., Crowley, T., Pongratz, J., et al. (2010). Climate and carbon-cycle variability over the last millennium. *Climate of the Past*, 6(5):723–737.

Kageyama, M., Albani, S., Braconnot, P., Harrison, S. P., Hopcroft, P. O., Ivanovic, R. F., Lambert, F., Marti, O., Peltier, W. R., Peterschmitt, J.-Y., et al. (2017). The PMIP4 contribution to CMIP6–Part 4: Scientific objectives and experimental design of the PMIP4-CMIP6 last glacial maximum experiments and PMIP4 sensitivity experiments. *Geoscientific Model Development*, 10(11):4035–4055.

Kageyama, M., Paul, A., Roche, D. M., and Van Meerbeeck, C. J. (2010). Modelling glacial climatic millennial-scale variability related to changes in the atlantic meridional overturning circulation: a review. *Quaternary Science Reviews*, 29(21-22):2931–2956.

Kageyama, M. and Valdes, P. J. (2000). Impact of the north american ice-sheet orography on the last glacial maximum eddies and snowfall. *Geophysical Research Letters*, 27(10):1515–1518.

Kalnay, E. (2003). *Atmospheric modeling, data assimilation and predictability*. Cambridge university press.

Kapsch, M.-L., Mikolajewicz, U., Ziemen, F., and Schannwell, C. (2022). Ocean response in transient simulations of the last deglaciation dominated by underlying ice-sheet reconstruction and method of meltwater distribution. *Geophysical Research Letters*, 49(3):e2021GL096767.

Kawamura, K., Parrenin, F., Lisiecki, L., Uemura, R., Vimeux, F., Severinghaus, J. P., Hutterli, M. A., Nakazawa, T., Aoki, S., Jouzel, J., et al. (2007). Northern hemisphere forcing of climatic cycles in antarctica over the past 360,000 years. *Nature*, 448(7156):912–916.

Kiefer, T., Lorenz, S., Schulz, M., Lohmann, G., Sarnthein, M., and Elderfield, H. (2002). Response of precipitation over greenland and the adjacent ocean to north pacific warm spells during dansgaard–oeschger stadials. *Terra Nova*, 14(4):295–300.

Kikstra, J. S., Nicholls, Z. R., Smith, C. J., Lewis, J., Lamboll, R. D., Byers, E., Sandstad, M., Meinshausen, M., Gidden, M. J., Rogelj, J., et al. (2022). The ipcc sixth assessment report wgiii climate assessment of mitigation pathways: from emissions to global temperatures. *Geoscientific Model Development*, 15(24):9075–9109.

King, J. M., Anchukaitis, K. J., Tierney, J. E., Hakim, G. J., Emile-Geay, J., Zhu, F., and Wilson, R. (2021). A data assimilation approach to last millennium temperature field reconstruction using a limited high-sensitivity proxy network. *Journal of Climate*, 34(17):7091–7111.

Kirchgessner, P., Nerger, L., and Bunse-Gerstner, A. (2014). On the choice of an optimal localization radius in ensemble kalman filter methods. *Monthly Weather Review*, 142(6):2165–2175.

Kistler, R. E. (1974). *A study of data assimilation techniques in an autobarotropic, primitive equation, channel model*. PhD thesis, Pennsylvania State University, Pennsylvania.

Klockmann, M., Mikolajewicz, U., and Marotzke, J. (2018). Two amoc states in response to decreasing greenhouse gas concentrations in the coupled climate model mpi-esm. *Journal of Climate*, 31(19):7969–7984.

Knorr, G. and Lohmann, G. (2003). Southern ocean origin for the resumption of atlantic thermohaline circulation during deglaciation. *Nature*, 424(6948):532–536.

Knorr, G. and Lohmann, G. (2007). Rapid transitions in the atlantic thermohaline circulation triggered by global warming and meltwater during the last deglaciation. *Geochemistry, Geophysics, Geosystems*, 8(12).

Köhler, P., Nehrbass-Ahles, C., Schmitt, J., Stocker, T. F., and Fischer, H. (2017). A 156 kyr smoothed history of the atmospheric greenhouse gases co 2, ch 4, and n 2 o and their radiative forcing. *Earth System Science Data*, 9(1):363–387.

Kurahashi-Nakamura, T., Paul, A., and Losch, M. (2017). Dynamical reconstruction of the global ocean state during the last glacial maximum. *Paleoceanography*, 32(4):326–350.

Lambeck, K., Rouby, H., Purcell, A., Sun, Y., and Sambridge, M. (2014). Sea level and global ice volumes from the last glacial maximum to the holocene. *Proceedings of the National Academy of Sciences*, 111(43):15296–15303.

Lang, N. and Wolff, E. W. (2011). Interglacial and glacial variability from the last 800 ka in marine, ice and terrestrial archives. *Climate of the Past*, 7(2):361–380.

Laskar, J., Robutel, P., Joutel, F., Gastineau, M., Correia, A., and Levrard, B. (2004). A long-term numerical solution for the insolation quantities of the earth. *Astronomy & Astrophysics*, 428(1):261–285.

Li, X. (2014). Characterization, controlling, and reduction of uncertainties in the modeling and observation of land-surface systems. *Science China Earth Sciences*, 57(1):80–87.

Li, X., Huang, C. L., Che, T., Jin, R., Wang, S. G., Wang, J. M., Gao, F., Zhang, S. W., Qiu, C. J., and Wang, C. H. (2007). Development of a chinese land data assimilation system: Its progress and prospects. *Progress in Natural Science*, 17:881–892.

Lisiecki, L. E. (2010). Links between eccentricity forcing and the 100,000-year glacial cycle. *Nature geoscience*, 3(5):349–352.

Lisiecki, L. E. and Raymo, M. E. (2005). A pliocene-pleistocene stack of 57 globally distributed benthic $\delta$18o records. *Paleoceanography*, 20(1).

Lisiecki, L. E., Raymo, M. E., and Curry, W. B. (2008). Atlantic overturning responses to late pleistocene climate forcings. *Nature*, 456(7218):85–88.

Liu, Z., Otto-Bliesner, B., He, F., Brady, E., Tomas, R., Clark, P., Carlson, A., Lynch-Stieglitz, J., Curry, W., Brook, E., et al. (2009). Transient simulation of last deglaciation with a new mechanism for bølling-allerød warming. *science*, 325(5938):310–314.

Liu, Z., Zhu, J., Rosenthal, Y., Zhang, X., Otto-Bliesner, B. L., Timmermann, A., Smith, R. S., Lohmann, G., Zheng, W., and Elison Timm, O. (2014). The holocene temperature conundrum. *Proceedings of the National Academy of Sciences*, 111(34):E3501–E3505.

Löfverström, M., Caballero, R., Nilsson, J., and Kleman, J. (2014). Evolution of the large-scale atmospheric circulation in response to changing ice sheets over the last glacial cycle. *Climate of the Past*, 10(4):1453–1471.

Löfverström, M. and Lora, J. M. (2017). Abrupt regime shifts in the north atlantic atmospheric circulation over the last deglaciation. *Geophysical Research Letters*, 44(15):8047–8055.

Lohmann, G., Butzin, M., Eissner, N., Shi, X., and Stepanek, C. (2020). Abrupt climate and weather changes across time scales. *Paleoceanography and Paleoclimatology*, 35(9):e2019PA003782.

Lohmann, G. and Schneider, J. (1999). Dynamics and predictability of stommel's box model. a phase-space perspective with implications for decadal climate variability. *Tellus A*, 51(2):326–336.

Lohmann, G. and Schulz, M. (2000). Reconciling bølling warmth with peak deglacial meltwater discharge. *Paleoceanography*, 15(5):537–540.

Lorenz, E. N. (1982). Atmospheric predictability experiments with a large numerical model. *Tellus Series A-Dynamic Meteorology and Oceanography*, 34:505–513.

Mairesse, A., Goosse, H., Mathiot, P., Wanner, H., and Dubinkina, S. (2013). Investigating the consistency between proxy-based reconstructions and climate models using data assimilation: a mid-holocene case study. *Climate of the Past*, 9(6):2741–2757.

Marcott, S. A., Shakun, J. D., Clark, P. U., and Mix, A. C. (2013). A reconstruction of regional and global temperature for the past 11,300 years. *science*, 339(6124):1198–1201.

MARGO (2009). Constraints on the magnitude and patterns of ocean cooling at the last glacial maximum. *Nature Geoscience*, 2(2):127–132.

Masoum, A., Nerger, L., Willeit, M., Ganopolski, A., and Lohmann, G. (2024). Paleoclimate data assimilation with climber-x: An ensemble kalman filter for the last deglaciation. *Plos one*, 19(4):e0300138.

Masson-Delmotte, V., Schulz, M., Abe-Ouchi, A., Beer, J., Ganopolski, A., González Rouco, J. F., Jansen, E., Lambeck, K., Luterbacher, J., Naish, T., et al. (2013). Information from paleoclimate archives.

Masson-Delmotte, V., Zhai, P., Pirani, S., Connors, C., Péan, S., Berger, N., Caud, Y., Chen, L., Goldfarb, M., and Scheel Monteiro, P. M. (2021). Ipcc, 2021: Summary for policymakers. in: Climate change 2021: The physical science basis. contribution of working group i to the sixth assessment report of the intergovernmental panel on climate change.

Matsikaris, A., Widmann, M., and Jungclaus, J. (2015). On-line and off-line data assimilation in palaeoclimatology: a case study. *Climate of the Past*, 11(1):81–93.

Max, L., Nürnberg, D., Chiessi, C. M., Lenz, M. M., and Mulitza, S. (2022). Subsurface ocean warming preceded heinrich events. *Nature Communications*, 13(1):4217.

McManus, J. F., Francois, R., Gherardi, J.-M., Keigwin, L. D., and Brown-Leger, S. (2004). Collapse and rapid resumption of atlantic meridional circulation linked to deglacial climate changes. *nature*, 428(6985):834–837.

McManus, J. F., Oppo, D. W., Keigwin, L. D., Cullen, J. L., and Bond, G. C. (2002). Thermohaline circulation and prolonged interglacial warmth in the north atlantic. *Quaternary Research*, 58(1):17–21.

Meyer, V. D., Hefter, J., Lohmann, G., Max, L., Tiedemann, R., and Mollenhauer, G. (2017). Summer temperature evolution on the kamchatka peninsula, russian far east, during the past 20 000 years. *Climate of the Past*, 13(4):359–377.

Milankovitch, M. (1941). Canon of insolation and the iceage problem. *Koniglich Serbische Akademice Beograd Special Publication*, 132.

Monnin, E., Indermuhle, A., Dallenbach, A., Fluckiger, J., Stauffer, B., Stocker, T. F., Raynaud, D., and Barnola, J.-M. (2001). Atmospheric CO2 concentrations over the last glacial termination. *Science*, 291(5501):112–114.

Mudelsee, M. (2001). The phase relations among atmospheric co2 content, temperature and global ice volume over the past 420 ka. *Quaternary Science Reviews*, 20(4):583–589.

Nerger, L. and Hiller, W. (2013). Software for ensemble-based data assimilation systems—implementation strategies and scalability. *Computers & Geosciences*, 55:110–118.

Nerger, L., Janjić, T., Schröter, J., and Hiller, W. (2012). A unification of ensemble square root kalman filters. *Monthly Weather Review*, 140(7):2335–2345.

Nerger, L., Tang, Q., and Mu, L. (2020). Efficient ensemble data assimilation for coupled models with the parallel data assimilation framework: example of awi-cm (awi-cm-pdaf 1.0). *Geoscientific Model Development*, 13(9):4305–4321.

Neukom, R., Barboza, L., Erb, M., Shi, F., Emile-Geay, J., Evans, M., Franke, J., Kaufman, D., Lücke, L., Rehfeld, K., et al. (2019a). Consistent multidecadal variability in global temperature reconstructions and simulations over the common era. *Nature geoscience*, 12(8):643–649.

Neukom, R., Steiger, N., Gómez-Navarro, J. J., Wang, J., and Werner, J. P. (2019b). No evidence for globally coherent warm and cold periods over the preindustrial common era. *Nature*, 571(7766):550–554.

Ng, H. C., Robinson, L. F., McManus, J. F., Mohamed, K. J., Jacobel, A. W., Ivanovic, R. F., Gregoire, L. J., and Chen, T. (2018). Coherent deglacial changes in western atlantic ocean circulation. *Nature communications*, 9(1):2947.

Obase, T. and Abe-Ouchi, A. (2019). Abrupt bølling-allerød warming simulated under gradual forcing of the last deglaciation. *Geophysical Research Letters*, 46(20):11397–11405.

Okazaki, A., Miyoshi, T., Yoshimura, K., Greybush, S. J., and Zhang, F. (2021). Revisiting online and offline data assimilation comparison for paleoclimate reconstruction: an idealized osse study. *Journal of Geophysical Research: Atmospheres*, 126(16):e2020JD034214.

Osman, M. B., Tierney, J. E., Zhu, J., Tardif, R., Hakim, G. J., King, J., and Poulsen, C. J. (2021). Globally resolved surface temperatures since the last glacial maximum. *Nature*, 599(7884):239–244.

Otto-Bliesner, B. L. and Brady, E. C. (2010). The sensitivity of the climate response to the magnitude and location of freshwater forcing: last glacial maximum experiments. *Quaternary Science Reviews*, 29(1-2):56–73.

Otto-Bliesner, B. L., Brady, E. C., Clauzet, G., Tomas, R., Levis, S., and Kothavala, Z. (2006). Last glacial maximum and holocene climate in ccsm3. *Journal of Climate*, 19(11):2526–2544.

Overpeck, J. T., Otto-Bliesner, B. L., Miller, G. H., Muhs, D. R., Alley, R. B., and Kiehl, J. T. (2006). Paleoclimatic evidence for future ice-sheet instability and rapid sea-level rise. *Science*, 311(5768):1747–1750.

Pahnke, K., Zahn, R., Elderfield, H., and Schulz, M. (2003). 340,000-year centennial-scale marine record of southern hemisphere climatic oscillation. *Science*, 301(5635):948–952.

Paillard, D. (2015). Quaternary glaciations: from observations to theories. *Quaternary Science Reviews*, 107:11–24.

Palmer, T. (2012). Towards the probabilistic earth-system simulator: A vision for the future of climate and weather prediction. *Quarterly Journal of the Royal Meteorological Society*, 138(665):841–861.

Palmer, T., Williams, P., and Williams, P. (2010). *Stochastic physics and climate modelling*, volume 480. Cambridge University Press Cambridge.

Parrenin, F., Masson-Delmotte, V., Köhler, P., Raynaud, D., Paillard, D., Schwander, J., Barbante, C., Landais, A., Wegner, A., and Jouzel, J. (2013). Synchronous change of atmospheric co2 and antarctic temperature during the last deglacial warming. *Science*, 339(6123):1060–1063.

Parsons, L. A., Amrhein, D. E., Sanchez, S. C., Tardif, R., Brennan, M. K., and Hakim, G. J. (2021). Do multi-model ensembles improve reconstruction skill in paleoclimate data assimilation? *Earth and Space Science*, 8(4):e2020EA001467.

Pedro, J., Rasmussen, S., and Van Ommen, T. (2012). Tightened constraints on the time-lag between antarctic temperature and co 2 during the last deglaciation. *Climate of the Past*, 8(4):1213–1221.

Peixoto, J. P. and Oort, A. H. (1992). Physics of climate.

Peltier, W. (2005). On the hemispheric origins of meltwater pulse 1A. *Quaternary Science Reviews*, 24(14-15):1655–1671.

Peltier, W. R. (1994). Ice age paleotopography. *Science*, 265(5169):195–201.

Peltier, W. R. (2004). Global glacial isostasy and the surface of the ice-age earth: the ice-5g (vm2) model and grace. *Annu. Rev. Earth Planet. Sci.*, 32:111–149.

Peltier, W. R., Argus, D., and Drummond, R. (2015). Space geodesy constrains ice age terminal deglaciation: The global ice-6g_c (vm5a) model. *Journal of Geophysical Research: Solid Earth*, 120(1):450–487.

Pendergrass, A. G. (2009). *Time-averaged data assimilation for midlatitude climates: Towards paleoclimate applications*. PhD thesis, University of Washington, Seattle.

Pendergrass, A. G., Hakim, G. J., Battisti, D. S., and Roe, G. (2012). Coupled air-mixed layer temperature predictability for climate reconstruction. *Journal of Climate*, 25:459–472.

Pépin, L., Raynaud, D., Barnola, J.-M., and Loutre, M. (2001). Hemispheric roles of climate forcings during glacial-interglacial transitions as deduced from the vostok record and lln-2d model experiments. *Journal of Geophysical Research: Atmospheres*, 106(D23):31885–31892.

Perkins, W. A. and Hakim, G. J. (2017). Reconstructing paleoclimate fields using online data assimilation with a linear inverse model. *Climate of the Past*, 13(5):421–436.

Petit, J.-R., Jouzel, J., Raynaud, D., Barkov, N. I., Barnola, J.-M., Basile, I., Bender, M., Chappellaz, J., Davis, M., Delaygue, G., et al. (1999). Climate and atmospheric history of the past 420,000 years from the vostok ice core, antarctica. *Nature*, 399(6735):429–436.

Petoukhov, V., Ganopolski, A., Brovkin, V., Claussen, M., Eliseev, A., Kubatzki, C., and Rahmstorf, S. (2000). Climber-2: a climate system model of intermediate complexity. part i: model description and performance for present climate. *Climate dynamics*, 16(1):1–17.

Pham, D. T. (2001). Stochastic methods for sequential data assimilation in strongly nonlinear systems. *Monthly weather review*, 129(5):1194–1207.

Pham, D. T., Verron, J., and Roubaud, M. C. (1998). A singular evolutive extended kalman filter for data assimilation in oceanography. *Journal of Marine systems*, 16(3-4):323–340.

Phipps, S. J., McGregor, H. V., Gergis, J., Gallant, A. J., Neukom, R., Stevenson, S., Ackerley, D., Brown, J. R., Fischer, M. J., and Van Ommen, T. D. (2013). Paleoclimate data–model comparison and the role of climate forcings over the past 1500 years. *Journal of Climate*, 26(18):6915–6936.

Pöppelmeier, F., Jeltsch-Thömmes, A., Lippold, J., Joos, F., and Stocker, T. F. (2023). Multi-proxy constraints on atlantic circulation dynamics since the last ice age. *Nature geoscience*, 16(4):349–356.

Project, N. G. I. C. (2004). High-resolution record of northern hemisphere climate extending into the last interglacial period. *Nature*, 431(7005):147–151.

Prokopenko, A. A., Hinnov, L. A., Williams, D. F., and Kuzmin, M. I. (2006). Orbital forcing of continental climate during the pleistocene: a complete astronomically tuned climatic record from lake baikal, se siberia. *Quaternary Science Reviews*, 25(23-24):3431–3457.

Rahmstorf, S. (1993). A fast and complete convection scheme for ocean models. *Ocean Modelling*, 101:9–11.

Redi, M. H. (1982). Oceanic isopycnal mixing by coordinate rotation. *Journal of Physical Oceanography*, 12(10):1154–1158.

Reichler, T. J. and Roads, J. O. (2003). The role of boundary and initial conditions for dynamical seasonal predictability. *Nonlinear Processes in Geophysics*, 10:211–232.

Renssen, H., Mairesse, A., Goosse, H., Mathiot, P., Heiri, O., Roche, D. M., Nisancioglu, K. H., and Valdes, P. J. (2015). Multiple causes of the younger dryas cold period. *Nature Geoscience*, 8(12):946–949.

Rice, J. L., Woodhouse, C. A., and Lukas, J. J. (2009). Science and decision making: Water management and tree-ring data in the western united states 1. *JAWRA Journal of the American Water Resources Association*, 45(5):1248–1259.

Robinson, A. R. and Lermusiaux, P. F. (2000). Overview of data assimilation. *Harvard reports in physical/interdisciplinary ocean science*, 62(1):1–13.

Roche, D. M., Wiersma, A. P., and Renssen, H. (2010). A systematic study of the impact of freshwater pulses with respect to different geographical locations. *Climate Dynamics*, 34:997–1013.

Romanova, V., Lohmann, G., Grosfeld, K., and Butzin, M. (2006). The relative role of oceanic heat transport and orography on glacial climate. *Quaternary science reviews*, 25(7-8):832–845.

Rühlemann, C., Mulitza, S., Lohmann, G., Paul, A., Prange, M., and Wefer, G. (2004). Intermediate depth warming in the tropical atlantic related to weakened thermohaline circulation: Combining paleoclimate data and modeling results for the last deglaciation. *Paleoceanography*, 19(1).

Saltzman, B. (2002). *Dynamical Paleoclimatology: Generalized Theory of Global Climate Change*. Academic Press, San Diego.

Schmidt, G., Annan, J. D., Bartlein, P., Cook, B., Guilyardi, E., Hargreaves, J., Harrison, S., Kageyama, M., LeGrande, A., Konecky, B., et al. (2013). Using paleo-climate comparisons to constrain future projections in cmip5. *Climate of the Past Discussions*, 9(GSFC-E-DAA-TN8476).

Schmidt, G. A. (2010). Enhancing the relevance of palaeoclimate model/data comparisons for assessments of future climate change. *Journal of Quaternary Science*, 25(1):79–87.

Semtner Jr, A. J. (1976). A model for the thermodynamic growth of sea ice in numerical investigations of climate. *Journal of Physical Oceanography*, 6(3):379–389.

Shackleton, N. J. (2000). The 100,000-year ice-age cycle identified and found to lag temperature, carbon dioxide, and orbital eccentricity. *Science*, 289(5486):1897–1902.

Shakun, J. D. and Carlson, A. E. (2010). A global perspective on last glacial maximum to holocene climate change. *Quaternary Science Reviews*, 29(15-16):1801–1816.

Shakun, J. D., Clark, P. U., He, F., Marcott, S. A., Mix, A. C., Liu, Z., Otto-Bliesner, B., Schmittner, A., and Bard, E. (2012). Global warming preceded by increasing carbon dioxide concentrations during the last deglaciation. *Nature*, 484(7392):49–54.

Sherriff-Tadano, S., Abe-Ouchi, A., Yoshimori, M., Oka, A., and Chan, W.-L. (2018). Influence of glacial ice sheets on the atlantic meridional overturning circulation through surface wind change. *Climate dynamics*, 50:2881–2903.

Shikazono, N. and Shikazono, N. (2012). *Introduction to earth and planetary system science: a new view of the earth, planets, and humans*. Springer.

Shuman, B., Webb Iii, T., Bartlein, P., and Williams, J. W. (2002). The anatomy of a climatic oscillation: vegetation change in eastern north america during the younger dryas chronozone. *Quaternary Science Reviews*, 21(16-17):1777–1791.

Smerdon, J. (2011). Discussion of "a statistical analysis of multiple temperature proxies: Are reconstructions of surface temperatures over the last 1000 years reliable?". *Annals of Applied Statistics*, 5:76–79.

Smith, K., Boccaletti, G., Henning, C., Marinov, I., Tam, C., Held, I., and Vallis, G. (2002). Turbulent diffusion in the geostrophic inverse cascade. *Journal of Fluid Mechanics*, 469:13–48.

Smith, R. S. and Gregory, J. M. (2009). A study of the sensitivity of ocean overturning circulation and climate to freshwater input in different regions of the north atlantic. *Geophysical Research Letters*, 36(15).

Snyder, C. W. (2010). The value of paleoclimate research in our changing climate: An editorial comment. *Climatic change*, 100(3):407–418.

Spada, G. and Stocchi, P. (2007). Selen: A fortran 90 program for solving the "sea-level equation". *Computers & Geosciences*, 33(4):538–562.

Spahni, R., Chappellaz, J., Stocker, T. F., Loulergue, L., Hausammann, G., Kawamura, K., Fluckiger, J., Schwander, J., Raynaud, D., Masson-Delmotte, V., et al. (2005). Atmospheric methane and nitrous oxide of the late pleistocene from antarctic ice cores. *Science*, 310(5752):1317–1321.

Steiger, N. J., Hakim, G. J., Steig, E. J., Battisti, D. S., and Roe, G. H. (2014). Assimilation of time-averaged pseudoproxies for climate reconstruction. *Journal of Climate*, 27(1):426–441.

Steiger, N. J., Smerdon, J. E., Cook, E. R., and Cook, B. I. (2018). A reconstruction of global hydroclimate and dynamical variables over the common era. *Scientific data*, 5(1):1–15.

Stenni, B., Buiron, D., Frezzotti, M., Albani, S., Barbante, C., Bard, E., Barnola, J., Baroni, M., Baumgartner, M., Bonazza, M., et al. (2011). Expression of the bipolar see-saw in antarctic climate records during the last deglaciation. *Nature Geoscience*, 4(1):46–49.

Stocker, T. (2011). *Introduction to climate modelling*. Springer Science & Business Media.

Stocker, T. F. and Johnsen, S. J. (2003). A minimum thermodynamic model for the bipolar seesaw. *Paleoceanography*, 18(4).

Stott, L., Timmermann, A., and Thunell, R. (2007). Southern hemisphere and deep-sea warming led deglacial atmospheric co2 rise and tropical warming. *science*, 318(5849):435–438.

Stouffer, R. J., Seidov, D., and Haupt, B. J. (2007). Climate response to external sources of freshwater: North atlantic versus the southern ocean. *Journal of Climate*, 20(3):436–448.

Stouffer, R. J., Yin, J., Gregory, J., Dixon, K., Spelman, M., Hurlin, W., Weaver, A., Eby, M., Flato, G., Hasumi, H., et al. (2006). Investigating the causes of the response of the thermohaline circulation to past and future climate changes. *Journal of climate*, 19(8):1365–1387.

Sturm, K., Hoffmann, G., Langmann, B., and Stichler, W. (2005). Simulation of d18o in precipitation by the regional circulation model remoiso. *Hydrological Processes*, 19:3425–3444.

Su, Y., Fang, X. Q., and Yin, J. (2014). Impact of climate change on fluctuations of grain harvests in china from the western han dynasty to the five dynasties (206 bc–960 ad). *Science China Earth Sciences*, 57:1701–1712.

Sun, Y., Knorr, G., Zhang, X., Tarasov, L., Barker, S., Werner, M., and Lohmann, G. (2022). Ice sheet decline and rising atmospheric co2 control amoc sensitivity to deglacial meltwater discharge. *Global and Planetary Change*, 210:103755.

Swingedouw, D., Houssais, M.-N., Herbaut, C., Blaizot, A.-C., Devilliers, M., and Deshayes, J. (2022). Amoc recent and future trends: A crucial role for oceanic resolution and greenland melting? *Frontiers in Climate*, 4:838310.

Talagrand, O. (1997). Assimilation of observations, an introduction (gtspecial issueltdata assimilation in meteology and oceanography: Theory and practice). *Journal of the Meteorological Society of Japan. Ser. II*, 75(1B):191–209.

Tarasov, L., Dyke, A. S., Neal, R. M., and Peltier, W. R. (2012). A data-calibrated distribution of deglacial chronologies for the north american ice complex from glaciological modeling. *Earth and Planetary Science Letters*, 315:30–40.

Tarasov, L. and Richard Peltier, W. (2002). Greenland glacial history and local geodynamic consequences. *Geophysical Journal International*, 150(1):198–229.

Tardif, R., Hakim, G. J., Perkins, W. A., Horlick, K. A., Erb, M. P., Emile-Geay, J., Anderson, D. M., Steig, E. J., and Noone, D. (2019). Last millennium reanalysis with an expanded proxy database and seasonal proxy modeling. *Climate of the Past*, 15(4):1251–1273.

Tierney, J. E., Poulsen, C. J., Montañez, I. P., Bhattacharya, T., Feng, R., Ford, H. L., Hönisch, B., Inglis, G. N., Petersen, S. V., Sagoo, N., et al. (2020a). Past climates inform our future. *science*, 370(6517):eaay3701.

Tierney, J. E. and Tingley, M. P. (2014). A bayesian, spatially-varying calibration model for the tex86 proxy. *Geochimica et Cosmochimica Acta*, 127:83–106.

Tierney, J. E., Zhu, J., King, J., Malevich, S. B., Hakim, G. J., and Poulsen, C. J. (2020b). Glacial cooling and climate sensitivity revisited. *Nature*, 584(7822):569–573.

Timmermann, A., Timm, O., Stott, L., and Menviel, L. (2009). The roles of co2 and orbital forcing in driving southern hemispheric temperature variations during the last 21 000 yr. *Journal of Climate*, 22(7):1626–1640.

Ullman, D., LeGrande, A., Carlson, A. E., Anslow, F., and Licciardi, J. (2014). Assessing the impact of laurentide ice sheet topography on glacial climate. *Climate of the Past*, 10(2):487–507.

Vaganov, E. A., Anchukaitis, K. J., and Evans, M. N. (2006). How well understood are the processes that create dendroclimatic records? a mechanistic model of climatic control on conifer tree-ring growth dynamics. In Malcolm, K. H., Thomas, W. S., and Henry, F. D., editors, *Dendroclimatology: Progress and Prospects*, pages 37–75. Springer-Verlag, Beilin.

Veres, D., Bazin, L., Landais, A., Toyé Mahamadou Kele, H., Lemieux-Dudon, B., Parrenin, F., Martinerie, P., Blayo, E., Blunier, T., Capron, E., et al. (2013). The antarctic ice core chronology (aicc2012): an optimized multi-parameter and multi-site dating approach for the last 120 thousand years. *Climate of the Past*, 9(4):1733–1748.

von Storch, H., Cubasch, U., Gonzalez-Rouco, J. F., Jones, J. M., Voss, R., Widmann, M., and Zorita, E. (2000). Combining paleoclimatic evidence and gcms by means of data assimilation through upscaling and nudging (datun). In *Proceedings of the 11th Symposium on Global Change Studies*, pages 28–31.

Waelbroeck, C., Duplessy, J.-C., Michel, E., Labeyrie, L., Paillard, D., and Duprat, J. (2001). The timing of the last deglaciation in north atlantic climate records. *Nature*, 412(6848):724–727.

Wallace, J. M. and Hobbs, P. V. (2006). *Atmospheric science: an introductory survey*, volume 92. Elsevier.

Wang, R., Kuhn, G., Gong, X., Biskaborn, B. K., Gersonde, R., Lembke-Jene, L., Lohmann, G., Tiedemann, R., and Diekmann, B. (2021). Deglacial land-ocean linkages at the alaskan continental margin in the bering sea. *Frontiers in Earth Science*, page 1172.

Wang, Y. S. (1999). Data assimilation-its cause, its meaning and main procedures. *Mar Forecasts*, 16:11–20. in Chinese with English abstract.

Weaver, A. J., Saenko, O. A., Clark, P. U., and Mitrovica, J. X. (2003). Meltwater pulse 1a from antarctica as a trigger of the bølling-allerød warm interval. *Science*, 299(5613):1709–1713.

Whitaker, J. S., Compo, G. P., Wei, X., and Hamill, T. M. (2004). Reanalysis without radiosondes using ensemble data assimilation. *Monthly Weather Review*, 132:1190–1200.

Whitaker, J. S. and Hamill, T. M. (2002). Ensemble data assimilation without perturbed observations. *Monthly Weather Review*, 130:1913–1924.

Widmann, M., Goosse, H., Schrier, G., Schnur, R., and Barkmeijer, J. (2010). Using data assimilation to study extratropical northern hemisphere climate over the last millennium. *Climate of the Past*, 6:627–644.

Willeit, M. and Ganopolski, A. (2016). Paladyn v1. 0, a comprehensive land surface–vegetation–carbon cycle model of intermediate complexity. *Geoscientific Model Development*, 9(10):3817–3857.

Willeit, M., Ganopolski, A., Calov, R., and Brovkin, V. (2019). Mid-pleistocene transition in glacial cycles explained by declining co2 and regolith removal. *Science Advances*, 5(4):eaav7337.

Willeit, M., Ganopolski, A., Robinson, A., and Edwards, N. R. (2022). The earth system model climber-x v1. 0–part 1: Climate model description and validation. *Geoscientific Model Development*, 15(14):5905–5948.

Ying, Y., Zhang, F., and Anderson, J. L. (2018). On the selection of localization radius in ensemble filtering for multiscale quasigeostrophic dynamics. *Monthly Weather Review*, 146(2):543–560.

Yokoyama, Y., Lambeck, K., De Deckker, P., Esat, T. M., Webster, J. M., and Nakada, M. (2022). Towards solving the missing ice problem and the importance of rigorous model data comparisons. *Nature Communications*, 13(1):6261.

Yu, G., Liu, J., and Xue, B. (2007). *Dynamical Paleoclimate Simulations*. Higher Education Press, Beijing. in Chinese.

Zhang, D. E. and Jiang, G. M. (2004). *A Compendium of Chinese Meteorological Records of the Last 3000 Years*. Jiangsu Education Publishing House, Phoenix Publishing House, Nanjing. in Chinese.

Zhang, X., Barker, S., Knorr, G., Lohmann, G., Drysdale, R., Sun, Y., Hodell, D., and Chen, F. (2021). Direct astronomical influence on abrupt climate variability. *Nature Geoscience*, 14(11):819–826.

Zhang, X., Knorr, G., Lohmann, G., and Barker, S. (2017). Abrupt north atlantic circulation changes in response to gradual co2 forcing in a glacial climate state. *Nature Geoscience*, 10(7):518–523.

Zhang, X., Lohmann, G., Knorr, G., and Purcell, C. (2014). Control of rapid glacial climate shifts by variations in intermediate ice-sheet volume. *Nature*, 512:290–294.

Zhang, X. P., Wang, X. Y., Yang, Z. L., Niu, G. Y., and Xie, Z. C. (2009). Simulations of seasonal variations of stable water isotopes in land surface process model clm. *Chinese Science Bulletin*, 54:1765–1772.

Zhu, J., Liu, Z., Zhang, X., Eisenman, I., and Liu, W. (2014). Linear weakening of the amoc in response to receding glacial ice sheets in ccsm3. *Geophysical Research Letters*, 41(17):6252–6258.

Zhu, J., Otto-Bliesner, B. L., Brady, E. C., Poulsen, C. J., Tierney, J. E., Lofverstrom, M., and DiNezio, P. (2021). Assessment of equilibrium climate sensitivity of the community earth system model version 2 through simulation of the last glacial maximum. *Geophysical Research Letters*, 48(3):e2020GL091220.

Zhu, J., Poulsen, C. J., Otto-Bliesner, B. L., Liu, Z., Brady, E. C., and Noone, D. C. (2020). Simulation of early eocene water isotopes using an earth system model and its implication for past climate reconstruction. *Earth and Planetary Science Letters*, 537:116164.